Katalytisch-induzierte Änderungen der Morphologie von Kupferkatalysatoren

von Diplom-Chemiker

Hans-Jörg Wölk

aus Hamburg

Fakultät II Mathematik und Naturwissenschaften
der Technischen Universität Berlin
zur Erlangung des akademischen Grades
Doktor der Naturwissenschaften
Dr. rer. nat.

vorgelegte Dissertation

Promotionsausschuß:

Vorsitzender:	Prof. Dr. R. Schomäcker
Berichter:	Prof. Dr. M. Lerch
Berichter:	Prof. Dr. R. Schlögl

Tag der mündlichen Prüfung: 27.05.2002

Berlin, 2002

D 83

Abstract

Kupferkatalysatoren sind für Reaktionen, die in der chemischen Industrie angewendet werden, von großer Bedeutung. In diesem Zusammenhang wird im Rahmen dieser Arbeit die katalytische Aktivität von Kupferkatalysatoren in Modellreaktionen, wie besonders der Methanoloxidation und anderen Partialoxidationsreaktionen berichtet. Die Untersuchung erfolgte mit Hilfe thermoanalytischer Techniken (TG/DTA), temperatur-programmierter Oxidation, Reduktion und Desorption (TPO/R/D). Besonders die Rasterelektronenmikroskopie (SEM) wurde zur Charakterisierung der Morphologie des Kupferkatalysators vor und nach der katalytischen Reaktion (Test) herangezogen.

Diese Arbeit basiert auf Ergebnissen, die an Silberkatalysatoren mit Hilfe der Photoelektronenspektroskopie (XPS) erzielt wurden. Auf Grund von strukturellen Gemeinsamkeiten zwischen Kupfer und Silber, bestätigt durch vergleichbare Ergebnisse aus der Röntgenabsorption (O-XANES), könnte eine Adaption des Silbermodells auf Kupfer möglich sein. Das Hauptinteresse der Untersuchungen jedoch stellt die Beobachtung von katalytisch-induzierten Veränderungen des Kupfers dar, da generell die Oberfläche des Katalysators seine Aktivität bestimmt. Um einen allgemeinen Bezug herstellen zu können, wurden neben sphärischen Kupferpartikeln unterschiedlichen Durchmessers, Cuprate wie Perowskite, Spinelle und die neue Verbindung $Ag_2Cu_2O_3$ untersucht. Das redoxchemische Verhalten von metallischem Kupfer konnte so mit dem von Oxiden verglichen werden. Dafür wurden verschiedene physikalische, metallurgische und kinetische Modelle herangezogen. Die Wahl dieser in ihren Eigenschaften unterschiedlichen Materialien sollte einen Transfer zwischen Festkörperkinetik und Katalyse möglich machen.

Als Resultat konnte ein deutlicher Bezug zwischen dem katalytischen Verhalten von Kupfer und dem von Silberkatalysatoren auf Grund der sauerstoff-induzierten Oberflächenrestrukturierung bestätigt werden. In Abhängigkeit von der Reaktionsatmosphäre konnten so Kupferpartikel aus verschiedenen Quellen generiert und mit metallischem Kupfer verglichen werden. Die katalytisch-induzierten morphologischen Änderungen des Kupfers folgen Gesetzen der Keimbildung (Avrami-Erofeev), Sinterung (Nabarro-Herring), und Hülle/Kern Ausbildung (Levenspiel) unabhängig von dem Oxidationszustand des Ausgangsmaterials.

Abstract

Copper-based catalysts are of considerable importance for industrial reactions, *e. g.* partial oxidation reactions. In this contribution, this work report on a broad study of the catalytic activity of copper catalysts in model redox reactions, *e. g.* methanol oxidation and oxidative coupling of methane with thermoanalytic techniques (TG/DTA), temperature programmed oxidation and reduction (TPO/TPR) and thermal desorption spectroscopy (TDS). Scanning electron microscopy (SEM) and X-ray-diffraction (XRD) was additionally used to characterise the copper catalyst morphology before after catalytic action (TEST).

This work is based on recent investigations of silver catalysts by photoelectron spectroscopy (XPS). Due to the structural similarity of copper and silver catalysts and comparable *in situ* O-XANES results, an adaptation of the model developed for silver to the behaviour of copper catalysts is can be imagined. The main interest is focussed on geometric and morphologic changes of copper during the catalytic reaction. In general, the surface of catalysts influences its activity. To optimise the detection of changes induced by catalysis, the reported experiments were made with spherical copper particles of diameters between <20µm up to 250µm. To manifest a general relation between copper metal particles and nano-scaled copper particles, the behaviour of three more different types of copper catalysts were investigated. The redox behaviour of copper aluminates, perovskite-type oxides and silver cuprates was correlated to the catalytic activity of the pure copper catalyst by application of several model dependent and independent kinetics. The reason for the choice of these different materials was to find a relation between solid state kinetics and catalytic reactions.

In conclusion, a strong relation was found between the catalytic behaviour of silver catalysts and copper catalysts for methanol oxidation and the oxidative coupling of methane, and morphological changes during the reactions. Due to the reaction atmosphere copper particles of different materials were generated and compared to unsupported copper metal. The alterations of the catalyst during the reactions are explained by several models. Sintering is described by Nabarro-Herring, the reduction by Avrami-Erofeev, the core-shell phenomenon by Levenspiel and the relation between surface structure and catalytic behaviour by the silver-oxygen model. The combination of these effects results in a complex description of the catalytic behaviour of copper in selective partial oxidation reactions.

Meinen Eltern

[...]
Per me si va ne la citta dolente,
per me si va ne l’etterno dolore,
per ne si va tra la perduta gente.

Guistizia mosse il mio alto faltere,
facemi la divina podestate,
la somma sa pienze e ’l primo amore.

Dinanzi a me non fuor cose create
se non etterne, e io etterno duro.
Losciate ogne speranza, voi ch’intrate.

Queste parole do colore oscuro
vid’io scitte al sommo d’una porta;
per ch’io:”Maestro, il senso lor m’ e duro.”

Ed elli a me, come persona accorta:
"Qui si convien lasciare ogne sospetto;
ogne viltà convien che qui sia morta”.
[...]

Dante Aligheri,

La divina comedia, Inferno, Canto III, 1-15.

Table of Contents

1 Introduction

Catalysis can be understood as an integrated process, which interrelates the atomic level, i.e. adsorption on, reaction at, and desorption from the active surface center, the microscopic level, i.e. surface faceting, particle sintering and growth, and the macroscopic level, i.e. the overall performance of the system reactor-catalyst-gas phase. In this respect next to the chemical properties of a catalyst, its morphology, i.e. shape of extrudates, or particle sizes, pore volume, etc., is of main importance for catalytic reactor activity and selectivity.

In case of catalytic oxidations, the redox chemistry of the chosen catalyst may also play an important role and, hence, the catalytic test reactions should be chosen well. The problem of the transfer of catalytic results to ultra high vacuum (UHV), surface science models still remains. The proper choice of the catalyst, e.g. defined particle geometries might help to solve the problem of the pressure and material gap.

Structure-reactivity correlation's are increasingly discussed to explain the activity of a catalyst in heterogeneous catalysis. The development of selective oxidation catalysts is based on a set of concepts amongst which site isolation or phase co-operation are fundamental[1, 2]. For that again the choice of the material for the catalytic test is most important for any further investigations. This choice can be separated into two routes. One is based on the "molecular modelling" of a catalysts microscopic geometry. The local electronic surroundings of the supposed active centre in the material should possibly be defined by preparation. This preparation could be managed in a laboratory using the "usual" way to produce a stable isolated compound or opposite to that by the in situ preparation during the catalytic reaction. This separation of both routes seem to be unbridgeable at the moment. Catalysis is also based on engineer sciences so the influence of the macroscopic geometry on the catalytic process also should be taken into account. Therefore the material can be used in different industry related morphologies. If both aspects could be combined a direct relation to results of surface science methods should be possible.

The interaction of small gas-phase molecules with a solid surface are in the centre of fundamental investigations often done under surface science

conditions. The catalytic reaction at the surface leads to the formation of product molecules, the whole process combining adsorption, reaction, desorption, and diffusion to and from the catalyst surface. Parallel to the changing gas phase, often morphological alterations of the catalyst can be observed during the catalytic reaction[3]. In case of selective partial oxidation reactions, the activation of molecular oxygen as forced by the properties of the catalyst is still an unsolved scientific problem. Active oxygen species may be formed at special surface sites either by adsorption and dissociation or by diffusion of bulk or subsurface oxygen to the surface.

The structure of a solid catalyst may support both pathways to active oxygen by the formation of an active surface, at which oxygen can adsorb and dissociate, or by its chemical bulk properties, e.g. easy oxygen diffusion.

Catalytic processes are used for the production of some of the most important chemical substances. A more fundamental knowledge about these reactions can help to improve these processes to save natural resources and the environment.

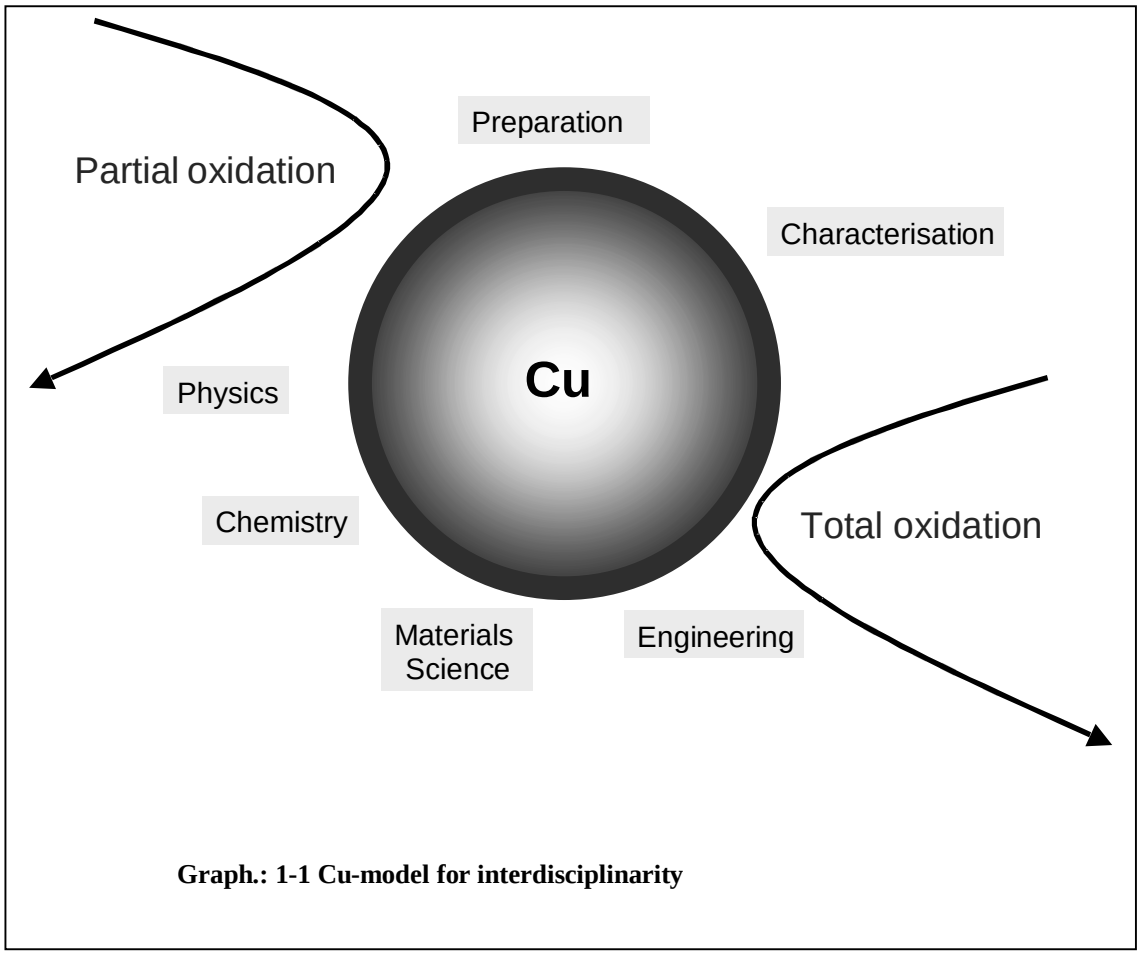

Graph.: 1-1 Cu-model for interdisciplinarity

Copper metal is used by human beings for several thousands of years because of its flexible material properties. It is easily to explore and to purify. The interest in the chemical properties of copper exists for several hundred years. The catalytic facilities were developed in the 19th century. The wide field of copper catalysts that were used since that time give rise to the assumption that a detailed explanation of its catalytic behaviour may be the general focus in catalysis. Opposite to the wide field of applications, the basically assumptions that makes copper to be a catalytic active material are rudimentary published. Because of the main importance of this metal many results ha been published by scientist of different fields of interests. This work tries to combine materials, engineer and chemistry sciences for a detailed interdisciplinary view on the behaviour of copper in partial oxidation reactions.

2 Industrial Motivation

2.1 Copper catalysts

Copper or copper containing compounds are used as catalysts for many different reactions in the chemical industry. The application of Cu-Al-Zn-O catalysts[4, 5] for the methanol synthesis is in the centre of investigations for a long time. Steam reforming and the dehydrogenation of methanol using a variety of different copper catalysts[6] are as important as the glycol oxidation on copper metal[7]. Additionally, copper catalysts are also used for the methanol oxidation to formaldehyde like silver catalysts.

2.1.1 Formaldehyde

2.1.1.1 General

Formaldehyde is naturally formed by photochemical oxidation in the atmosphere and is also one metabolism product of many organisms[8]. The industrial production of formaldehyde started 1889 by Merklin und Lösekann GmbH The first description of a preparation routine using a methanol-air mixture and platinum wires was published by A.W. Hoffmann in 1867. The industrial process was optimised by BASF parallel to the high pressure synthesis of methanol during the 20th century. 1988 the formaldehyde production was about 6,9+105 t/a in the former Federal German Republic[9].

2.1.1.2 Chemical properties

At room temperature, formaldehyde (F) is a smelling, colourless gas with a boiling point of –19.2°C and a melting point of –118°C. F - air mixtures between 7 Vol.-% and 71Vol.-% are highly flammable. Due to easy polymerisation, aqueous solutions contain the equilibrium of methylene glycol (HO-(CH_2O)-H) and poly-methylene glycol (HO-(CH_2O)$_n$-H, with n=1-8). The commercial products are the

polymerised para-formaldehyde, its solution (formaline), and the trimeric form, Trioxane[10].

Because of its highly reactivity, F is one of the most important C1-molecules in chemical industry. F is an intermediate for the production of fine chemicals as well for polymers like polyacatales.

2.1.1.3 Synthesis

Several industrial processes were developed for its synthesis, which can be distinguished: the air sub-stoichiometric and the air over-stoichiometric processes, both being based on methanol.

The BASF silver contact process is the most important sub-stoichiometric process. Elementary silver (crystalline or net-catalysts) is used under atmospheric pressure in the temperature range between 600°C and 720°C. Several thermodynamic equations describe the reaction mechanism (Equ.: 2-1).

(1) $CH_3OH + 3/2O_2$	→	$CO_2 + 2H_2O$	ΔH= -674kJ/mol	(total oxidation)
(2) $CH_3OH + ½O_2$	→	$CH_2O + H_2O$	ΔH=-159kJ/mol	(oxidehydrogenation)
(3) CH_3OH	→	$CH_2O + H_2$	ΔH=+84kJ/mol	(dehydrogenation)
(4) $CH_3OH + H_2O$	→	$CO_2 + 3H_2$	ΔH= +62kJ/mol	(steam reforming)
(5) $CH_3OH + 3/2O_2$	→	$CO + 2H_2$	ΔH= +119kJ/mol	
(6)$CH_2O + O_2$	→	$CO_2 + H_2O$	ΔH= -519kJ/mol	(total oxidation)
(7) CH_2O	→	$CO + H_2$	ΔH= +12.5kJ/mol	
(8) $CO_2 + H_2$	→	$CO + H_2O$	ΔH= +41kJ/mol	
(9) $H_2 + ½O_2$	→	H_2O	ΔH= -243kJ/mol	
(10) $CO + ½O_2$	→	CO_2	ΔH= -68kJ/mol	

Equ.: 2-1 Formaldehyde reaction pathways

All these reactions can be observed during the methanol oxidation reaction. The relative ratios of the different pathways depend on the reactor conditions, the catalyst, and the temperature.

Depending on the reaction conditions, 50-60% of F are produced by the partial oxidation reaction (1) and the rest via dehydrogenation (2). Due to the first, the whole process is exothermic.

To minimise exothermicity, water is added or the methanol conversion is kept incomplete. The maximum methanol conversion is near 97%, the selectivity to F is 90%.

The air-excess process (FORMOX-process) uses an iron-molybdenum oxide catalyst promoted by additional metal oxides. The product stream does not contain hydrogen, the reactor temperature profile is poly-tropic. The reaction possibly follows the Mars-Van Krevelen redox-mechanism. The main reaction step is the direct methanol partial oxidation.

3 Chemical Motivation

3.1 Copper

Copper (^{29}Cu, M= 63,5g/mol) belongs, together with silver and gold, to the 1. transition metal group of the periodic table of elements[11]. It is a noble element due to its standard electropotential ε_0 = 0,337 V (Cu/Cu^{2+}) and ε_0 = 0,521 (Cu/Cu^{+}). The configuration of its electrons is $1s^2$, $2s^2$, $2p^6$, $3s^2$, $3p^6$, $3d^{10}$, $4s^1$. Copper can exist in the oxidation states of +2, +1, 0, -2, -4, the most common being +2, +1, and 0. Copper crystallises in the cubic lattice (Cu-type). Its density is 8,92g/cm^3. The melting point is 1083°C, the boiling point 2595°C. Copper is easily oxidised to Cu_2O in air and at room temperature.

3.2 Copper Oxides

Two thermodynamically stable oxides are known, and their lattice parameters are listed in Tab.: 3-1. CuO[12] is described by the monoclinic tenorite lattice in which Cu is co-ordinated square planar by oxygen, and O is tetrahedrally co-ordinated by Cu with copper-oxygen distances of 1.94Å[13]. Cu_2O[14], the cuprite lattice-type oxide also showing tetrahedrally co-ordinated oxygen, is the example for linearly co-ordinated copper, i.e. the anti-cristobalite structure type, with copper-oxygen distances of 1.84Å (tab. 3-1). The crystal structure is highly symmetric with 6 atoms per unit cell. The low co-ordination number of 2 for Cu is unusual for oxides and causes an non-vanishing electric field gradient at Cu. The short distances of Cu and O, which are incompatible to any sum of Cu^+ and O^{2-} ionic radii, support the covalent character of the compound. The red Cu_2O has a full Cu 3d shell. It is a semiconductor with a gap of 2.17 eV[15]. The black CuO has an open 3d shell ($3d^9$) and it is an (anti-ferromagnetic) semiconductor with a gap of 1.4eV[16]. The densities of the oxides are ρ = 6,3g/cm^3 (CuO) and ρ = 6,0 g/cm^3 (Cu_2O) at 25°C.

	Cu_2O[12]	CuO[12]
Crystal parameters	cubic	monoclinic
	a=4.27Å	a=4.6837 Å
		b=3.4226 Å
		c=5.1288 Å
		β=99.54°
distances		
d_{Cu-O}/d_{Ag-O}	1.84 Å	1.95 Å
d_{O-O}	3.68 Å	2.62 Å
d_{Cu-Cu}/d_{Ag-Ag}	3.02 Å	2.90 Å

Tab.: 3-1 Crystal parameters of Cu_2O and CuO

3.2.1 Copper sub-oxides (non-stoichiometric oxides)

The discussion about the existence of copper sub-oxides is as old as the detection of the thermodynamically stable oxides. The earliest observations on this field were published by Tammann[17] about the colour change of Cu surfaces during oxidation at different temperatures. It was suggested that the oxygen content varies

with the changing colour[18]. The problem of an exact determination of the oxygen content led to the investigation of the crystallographic orientation of these layers[19]. The interaction of oxygen was found to influence the surface structures. The formation of facetted areas was detected parallel to the growth of oxidic layers also [20, 21, 22]. The inter-diffusion of Cu and the formed oxides[23] at elevated temperatures led to the formation of Cu(111) surfaces[24, 25]. The growth of the oxides on the copper surface was affected by the surface orientation. On spherical copper single crystals, the formation of concentric rings of Cu_2O was detected near the Cu(113) pole, the pyramidal growth of Cu_2O was found near Cu(111). The final thickness of this discontinuous oxide layer was about 100µm at 600°C and $5*10^{-3}$ Torr air.

At temperatures near 500°C, the copper oxidation follows a parabolic growth law ($L \sim t^{1/2}$) [26] up to an oxide thickness of L>400 nm with a constant ratio of CuO and Cu_2O. Cu_2O is formed first, subsequently islands of CuO were detected[27]. At temperatures below 400°C, a logarithmic growth law was assumed[28]. The differences in the exact description of the oxide formation started the discussion on the structure of thermodynamically stable suboxides. So far, the isolation and characterisation of a sub-oxide like $Cu_{1,5}O$[29] failed[30]. The formation of Cu_4O was described from CuO reduction at high temperatures. This compound is not stable at room temperature[31]. Detailed investigations always proved the co-existence of copper and copper oxide phases. In this discussion, the mineral para-melanconite[32], Cu_4O_3, can be seen as an intermediate. Its structure is explainable by the addition of oxygen to the Cu_2O lattice[36].

In situ X-ray absorption spectroscopy proved the existence of an additional oxygen species in the Cu lattice during the treatment of a polycrystalline Cu foil under catalytic conditions using a methanol/oxygen mixed atmosphere. It was not possible to determine the stoichiometry of this oxide. The binding energies of the oxygen and copper signals showed O 2*p*-Cu 4*s*- and O 2*p*-Cu 4*p*- interactions. The well known O 2*p*-Cu 3*d* hybridisation, as in the case of CuO and Cu_2O, could be neglected[33, 34].

3.3 Oxygen interaction with Copper surfaces and bulk

3.3.1 Phase diagram of the Cu-O system

The behaviour of Cu in selective partial oxidation reactions is related on the chemistry of the system copper-oxygen. The phase diagram of this system was developed before 1929 by Vogel and Pocher[35, 36] (Graph.: 3-1). This phase diagram, reflecting the technical possibilities of this time period, is still actual and not corrected in the literature yet. The high temperature behaviour of Cu, e.g. the Cu melting point at 1098°C, is well described by this phase diagram. But the catalytically important temperature range between 25°C and 1000°C shows several insufficiencies. Below 380°C Cu and CuO, copper(II)-oxide, are co-existing. At exactly 380°C, the phase transition to the other thermodynamically stable oxide, Cu_2O, occurs. Both oxides do not form mixed crystals and are described to be co-existing with copper metal up to 1075°C depending on the oxygen pressure. Informations on the structural and chemical mechanisms that are necessary for these transformations are not given, and sub-oxides are not described yet. The morphology of operating Cu-catalysts, e.g. activation or deactivation behaviour, may be affected by the phase diagram, e.g. oxygen partial pressure and reaction temperature, due to dissolution of oxygen, oxygen bulk diffusion, and the formation of oxides. The results, however, that are described in this work have shown that high temperature effects like melting and sintering are induced during catalytic reactions. Hence, the temperature range

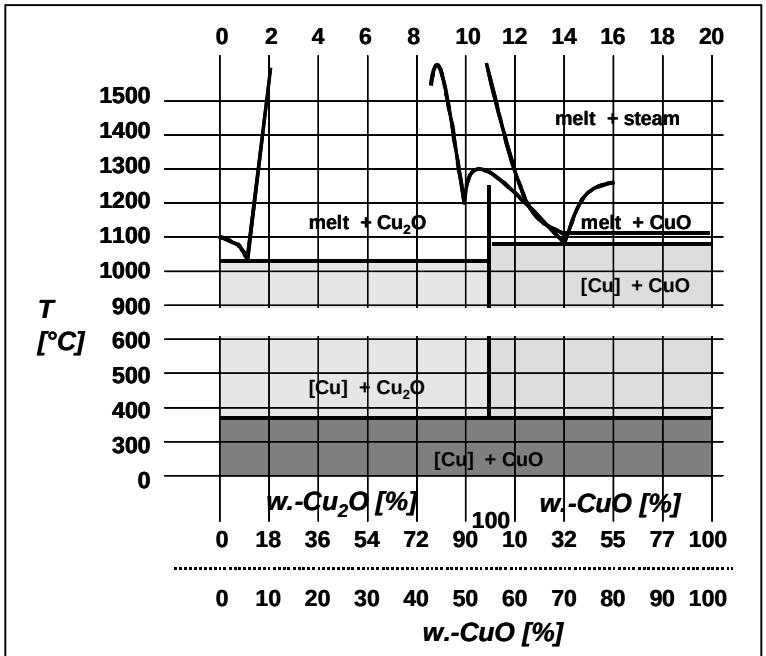

Graph.: 3-1 Phase diagram of Cu-O[35]

around 1000°C indeed could be very important for the explanation of the catalytic behavior of copper.

The equilibrium diagram for the systems Cu-Cu_2O and CuO-Cu_2O as a function of oxygen partial pressure and temperature allows a more detailed view on the copper-oxygen interaction (Graph 3-2). Under equilibrium conditions, the three phases Cu, CuO and Cu_2O are co-existing. The lines, denoted by I and II, are labelling the equilibrium pO_2 and T. The area between this two lines marks the area in which Cu_2O is stable.

A homogeneous copper oxide phase could not be obtained in case of Cu oxidation to Cu_2O. Solution of oxygen in the copper oxide lattice was observed, possibly as O^{2-} anions at vacancies in the oxygen sub-lattice These O^{2-}-ions are known to be responsible for the electrochemical behaviour of Cu_2O (semiconductor)[37].

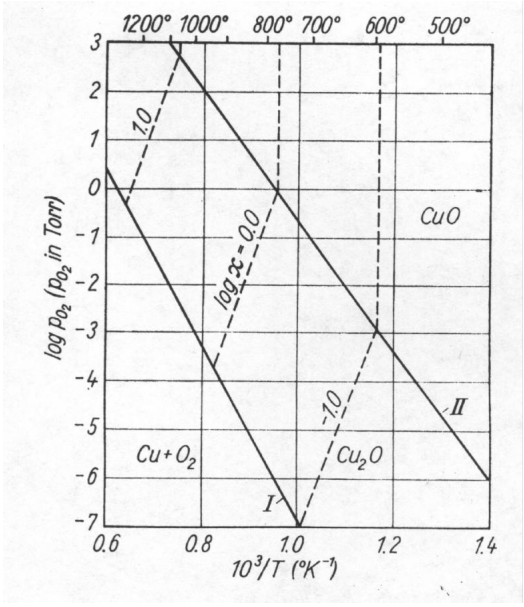

Graph.: 3-2 Phase diagram of Cu-O; oxygen dependence[80]

The dashed lines in graph. 3-2 describe the O-conductivity depending on temperature and oxygen partial pressure. Higher temperatures lead to the solution of more oxygen in the lattice and hence to an increase of the conductivity. In fact, the solubility of oxygen in the copper or copper oxide lattices is very low. It was found to be 0,0002 – 0,007 mass% for Cu and 0,02 – 0,06 mass% for Cu_2O[38, 39].

3.3.2 Oxygen adsorption on copper surfaces

Besides active lattice oxygen, the adsorption of O_2, its dissociation, and an interstitialcy dissolution into the catalysts surface[40], Cu or its oxides, may also lead to active O species for the catalytic oxidation reactions. The activation of the strong oxygen-oxygen bond in O_2 is still an unsolved problem of oxidation catalysis.

The way the oxygen is incorporated into the surface depends on reaction conditions, e.g. oxygen partial pressure, temperature, and surface orientation. Oxygen is physisorbed at low temperatures as atoms or molecules. Its chemisorption

on Cu leads to surface reconstruction[41]. The initial Cu surface orientation leads to different reactivities toward oxygen. The Cu(110) surface is more active for oxygen interaction than Cu(100) and Cu(111) surfaces[41].

The literature documents different results for the interaction of molecular oxygen with the Cu(111), Cu(110), and the Cu(100) surfaces[42]. Based on the technique used a variety of oxygen adlayers were found[43]. The low experimented temperatures of most of the surface science studies exclude simple data transfer to reactor tests performed at high temperatures. In case of copper, its oxygen affinity also leads to the formation of oxidic adlayers or the oxidation of the surface. It seems possible this surface oxidation may describe the observed catalyst deactivation. Surface oxidation is known to follow nucleation kinetics as a function of the oxygen partial pressure. The adsorption of oxygen on Cu(110) was found to start with the (2x1)-O(a) surface structure[44] at 50°C. Heating such surfaces did not lead to changes up to temperatures of around 210°C. At higher temperatures, the (2x1)-O(a) structure disappeared and the surface was partially oxidized. This implies that the diffusion of oxygen to the subsurface region began. This subsurface oxygen diffusion may provide a link to high pressure test reaction conditions. There was observed that oxygen diffuses to the copper subsurface region at 280°C[45]. Furthermore, the Cu(110) facet was found to be the most active of the low index faces for copper zinc catalysts and thus can be expected to be sensitive to temperature variations. In case of polycrystalline copper particles the methanol oxidation reaction was found to start at temperatures above 280°C[46]. Those combined observation render possible a diffusion mechanism that may be responsible for the catalytic activity. XPS or TDS measurements can only initially provide information about the depth of the oxygen diffusion. Longtime experiments under high pressure reaction conditions may solve this problem together with by using subsequent electron microscopy to determine morphological changes of the material.

3.3.3 Surface science model reactions for methanol oxidation on copper catalysts

The methanol oxidation to F (Equ.: 3-1) over Cu is an efficient process and has attracted significant interest as a model reaction for selective partial

oxidation. Most of the published studies are focussed on the interaction of the reactants with the Cu surface under ultra-high-vacuum conditions. Several mechanisms have been suggested[47, 48, 49]. The occurrence of methoxy and formate species during reaction has been controversially discussed[50 ,51 ,52]. As a result, the mechanisms depend strongly on the reaction conditions[53, 54]. A partially oxidised Cu surface was found to be active exhibiting nucleophilic oxygen. When using a copper (110) single crystal surface as substrate. Oxygen was responsible for the activation of the metal surface for the methanol adsorption and it reacts with the formed hydrogen to water (see chapter:2.2.3).

(11) $2CH_3OH + ½\ O_2 \rightarrow CH_2O + H_2 + H_2O$

Equ.: 3-1Basic Methanol oxidation reaction

The rate limiting step is the C-H bond breakage. A second reaction pathway to surface formate, $HCOO^-$, was additionally present[49] to the formation methoxy species, the latter decomposing to F and desorbing. The formate species could not be detected at 260K on a polycrystalline Cu surface, but occurs at a significant rate at 295K and temperatures above. On the O-Cu(111) surface, a minor methanol decomposition path for has been found to carbon dioxide probably via a formate surface intermediate[55]. The F production rate is surface independent, whereas the formate production rate is higher for the polycrystalline surfaces.

A detailed mechanism was developed for Cu(110) surfaces[56] being described by equations 12-20 (Equ. 3-2).

(12) $CH_3OH_{(g)} \rightarrow CH_3OH_{(ad)}$

(13) $CH_3OH_{(g)} + O_{(ad)} \rightarrow CH_3OH_{(ad)} + OH_{(ad)}$

(14) $CH_3OH_{(g)} + OH_{(ad)} \rightarrow CH_3OH_{(ad)} + H_2O_{(ad)}$

(15) $H_2O_{(ad)} \rightarrow H_2O_{(g)}$

(16) $CH_3OH_{(ad)} \rightarrow CH_2O_{(ad)} + H_{(ad)}$

(17) $CH_2O_{(ad)} \rightarrow CH_2O_{(g)}$

(17) $CH_3O_{(ad)} + H_{(ad)} \rightarrow CH_3OH_{(g)}$

(18) $2H_{(ad)} \rightarrow H_{2(g)}$

(19) $CH_2O_{(ad)} + O_{(ad)} \rightarrow CHO_{2(ad)} + H_{(ad)}$

(20) $CHO_{2(ad)} + O_{(ad)} \rightarrow CO_{2(g)} + H_{(ad)}$

Equ.: 3-2 Methanol oxidation on Cu(110)

It is suggested that the reaction follows a Langmuir-Hinshelwood mechanism. The first step is the hydrogen abstraction from methanol to form methoxy-radicals and water via a hydroxide. With increasing temperatures, F desorption is enhanced due to the abstraction of a second hydrogen from the methoxy species[56].

The role of pre-adsorbed oxygen is important for the F formation. An “oxygen free”, clean copper surface only shows a minor reaction with adsorbed methanol. In this case, methanol is molecularly adsorbed[57]. The ability of Cu, and silver, to adsorb methanol dissociatively is enhanced by the presence of co-adsorbed oxygen species, “oxygen induced adsorption”[58].

Oxygen atoms on Ag surfaces are identified as strong Broenstedt bases (proton acceptors). This nucleophilic oxygen species thus heterolytically activates both O-H and C-H bonds, both being necessary for the formation of methoxy and C=O containing species.

F was found to be weakly adsorbed via the oxygen on Cu(110) surfaces[59]. A much more strongly bound surface moiety is formed when formaldehyde is dosed on a oxygen pre-covered surface. The adsorbed oxygen species is added to the surface intermediate thus acting as an electrophilic Lewis acid.

The interaction of methanol with copper oxide surfaces depends on the crystal structure of the Cu_2O. F production was detected on Cu_2O (111) and Cu_2O(100) surfaces in the temperature range of 50°C to 380°C[60].

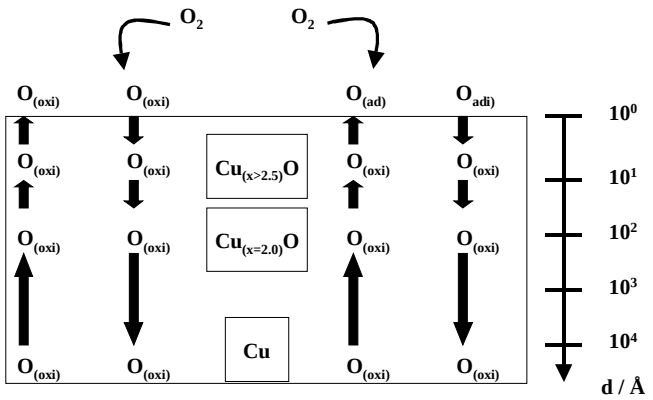

Graph.: 3-3 Diffusion model for oxygen-surface interaction on copper catalysts[34]

It was found that oxygen surface adatoms can diffuse to subsurface and near surface positions (Graph.: 3-4)[34] . After exposure of oxidised copper foils to methanol at high temperatures, the formation of $Cu_{(x\geq2.5)}O$ was observed in the near surface region underneath this non-stoichiometric oxide[34] . A Cu_2O film was detected at a depth of 400Å.

3.3.4 Oxidative coupling of methane, OCM

Oxidative coupling of methane (OCM) would be one of the most attractive methods for natural gas conversion into valuable products[61, 62, 63]. One possible reaction mechanism was described by the equations 21 to 26 (Equ.: 3-3).

The choice of OCM as test reaction for the catalytic activity of Cu based on the assumption that a slow thermally neutral reaction may lead to more detailed information on the O-Cu interaction opposite to the fast exothermic oxidative dehydrogenation of methanol. For both, methanol partial oxidation and OCM, the C-H bond breakage is suggested to be the rate limiting step, which should be catalysed by basic surface oxygens. Hence, kinetic measurements, being easier for the slow OCM than for the fast methanol oxidation reaction, should reveal details on the rate limiting step. This approach was successfully applied for the homologue Ag catalysts[64, 65].

The OCM reaction is known to be one of the most attractive methods of natural gas conversion into valuable products[61, 66, 67]. One possible reaction mechanism was described by the equations 21 to 26 (Equ.: 3-3).

(21) $2CH_4$	→	$C_2H_6+2H_2$	$\Delta H = +66kJ/mol$
(22) $2CH_4$	→	$C_2H_4+H_2$	$\Delta H = +186kJ/mol$
(23) $C_2H_4+3O_2$	→	$2CO_2+2H_2O$	$\Delta H = -1309kJ/mol$
(24) $C_2H_4+O_2$	→	$2CO+2H_2$	$\Delta H = -257kJ/mol$
(25) $C_2H_6+O_2$	→	$2CO+3H_2$	$\Delta H = -136kJ/mol$
(26) C_2H_6	→	$C_2H_4+H_2$	$\Delta H = +120kJ/mol$

Equ.: 3-3 General reaction scheme for oxidative methane coupling[68]

Cu catalysts are known to prefer total oxidation of methane, the selectivity to and the yield of C_2 species are low[69]. Low temperature oxidative coupling[70] was observed for several other transition metal oxides[71, 72], total oxidation especially for perovskite-type oxides[73, 74].

3.4 Partial oxidation on silver catalysts, Ag model

Work on silver catalysts in selective partial oxidation reactions have proven the correlation between activation energy of OCM and the activation energy of the oxygen diffusion in silver metal. In addition, an increase of catalyst activity was forced by its re-crystallisation and morphological changes induced by the reaction. Highly active silver catalysts have shown facets of mainly Ag(110) and Ag(100) surfaces[64, 75]. SEM (scanning electron microscopy) results showed that high-temperature treatment in oxygen leads to faceting of the silver surface. Combined XPS/UPS and TDS experiments[76, 40] and in situ XRD revealed that two distinctly different oxygen species are formed in the silver subsurface region[77] as a result of the gas-metal interaction (Graph. 3). These species differentiate themselves in both their location and bonding states. The detailed mechanism, however, leading to the formation of these species is not fully understood.

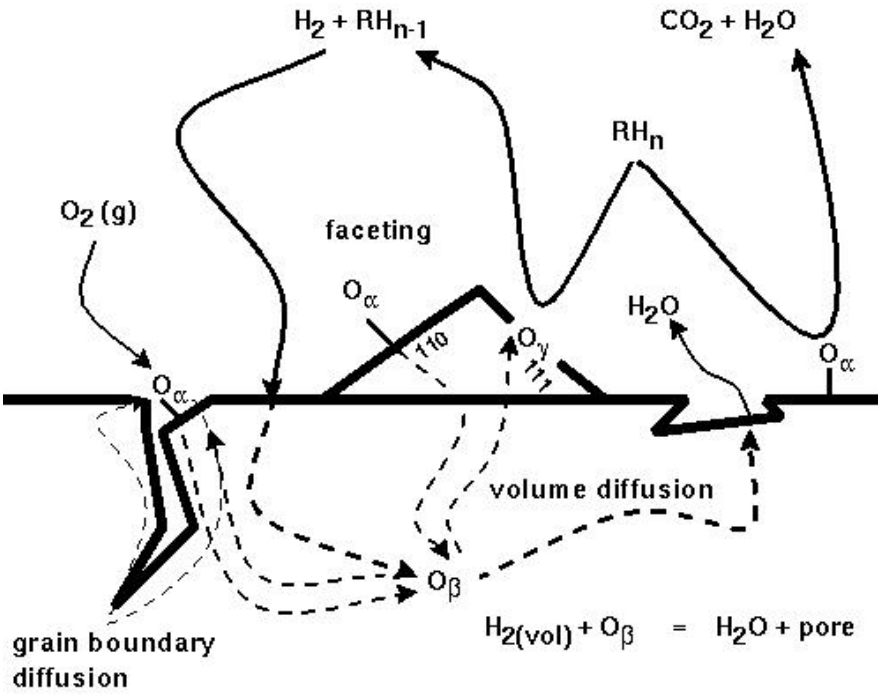

Graph.: 3-4 Ag-model for selective oxidation reaction (OCM; oxidative coupling of methane)[65].

The first step is the diffusion of chemisorbed oxygen, O_α, from the surface to form the bulk-dissolved species O_β. The second subsurface species, O_γ, is described as being interstitialcy dissolved in Ag. O_γ is formed from O_β via diffusion to Ag sites and its segregation to Ag(111) surfaces. The competing effect of thermal restructuring results in the formation of crystal different surfaces whose extent of formation shows a strong dependence on oxygen partial pressure. The methanol oxidation and the oxidative coupling of methane are believed to be catalysed by O_γ. The assumption that the segregation of O_β to the surface is necessary for O_γ formation implies that the kinetics of this step should play an important role for partial oxidation reactions[78] (Graph.: 3-4).

4 Specific Motivation

The motivation for this work is based on the results obtained for silver catalysts in selective partial oxidation reactions. The system copper-oxygen is one of the most investigated subjects in chemistry. Surprisingly some basic aspects are still unknown or already forgotten again. The relation between Cu morphology and redox processes may be the fundamental for the understanding of its catalytic activity. In order to obtain information about this relation, the material has to be chosen carefully. Most of the investigations on Cu used single crystals or foils and were conducted at UHV to guarantee defined conditions[79,80]. A real catalyst is polycrystalline, irregular in shape and thus prevents detailed structure-activity investigations. To render possible a transfer between surface science studies and real catalytic processes, defined spherical Cu particles of different diameters were chosen together with different cuprates. Using mainly the methanol oxidation as test reaction, chemical, metallurgical, crystallographic, physical and kinetic models can be applied to explain the phenomena occurring also under well defined conditions.

5 Morphological changes during the catalytic reaction

The Cu surface and the bulk undergoes a complete re-construction forced by the catalytic process. There are macroscopic and microscopic transformations that were detected subsequently to reaction by SEM (scanning electron microscopy), EDX (electron dispersive X-ray diffraction), and EBSD (electron back-scattering diffraction), and by detailed kinetic analysis of the obtained reaction data. The macroscopic changes of the Cu catalyst morphology could be described by six enhanced models.

5.1 Chemical model: Levenspiel control

In case of spherical Cu particles, the reconstruction during the catalytic action can be described by the core-shell formation according to Levenspiel[81] as a chemical model. The oxidation of the metal surface is a non-catalytic process, and moreover, it may be one reason for catalyst deactivation. Due to the spherical morphology of the Cu particles, fundamental microscopic aspects of the oxidation can be transferred to the macroscopic level. For spherical particles, Levenspiel developed the shrinking core and the crackling core models[82]. Both are based on the assumption of a spherical particle being surrounded by a concentric gas-shell. The reaction of both phases leads to the formation of a concentric reaction zone around the remaining metal core[83, 84, 85]. The growth of the oxide stops with the complete consumption of the core. During catalytic partial oxidation reactions, like OCM and MOX, several mechanisms may be assumed for metal oxidation. The oxidation process can be controlled by gas film diffusion, diffusion through the oxide, or the chemical reaction.

In the following, the basic model[82] for the rate of reaction for spherical particles of unchanging size is described by Equ.: 5-1.

(27) $A(g) + bB(s) \rightarrow rR(g) + sS(s)$

Equ.: 5-1 Basic Reaction equation for the reaction of a spherical solid with a gaseous shell (Levenspiel-approach)[82]

Step 1: Diffusion of gaseous reactant A through the film surrounding the particle to the surface of the solid B.

Step 2: Penetration and diffusion of A through the freshly formed shell S to the surface of the unreacted core B, forming the reaction surface.

Step 3: Chemical reaction of the gaseous reactant A with the solid B.

Step 4: Diffusion of the reaction products R through the shell S and gas film back into the main body of the fluid.

Because these steps successively occur for the reaction to take place, they can be considered as resistances in series. Whenever one of these steps offers the main resistance to the overall reaction, this step can be considered as the rate-determining step. The kinetics of these different steps usually vary greatly from each other. For easy application of this model, the particle is considered to be an individual sphere.

5.1.1 Reaction controlled by gas film diffusion

The reaction can be controlled by the diffusion through the gas film. In this case, reactants are not localised at the surface; hence, the concentration driving force of the concentration change $C_{Ag} - C_{As} = C_{Ag}$ is constant at all times during the reaction of the particle (Graph.: 5-1).

This step of the diffusion controlled model is defined by the resistance of a gaseous shell surrounding the particle.

The radius of the unreacted core in terms of fractional time for complete conversion is given by equation 28 (Equ.:5-2).

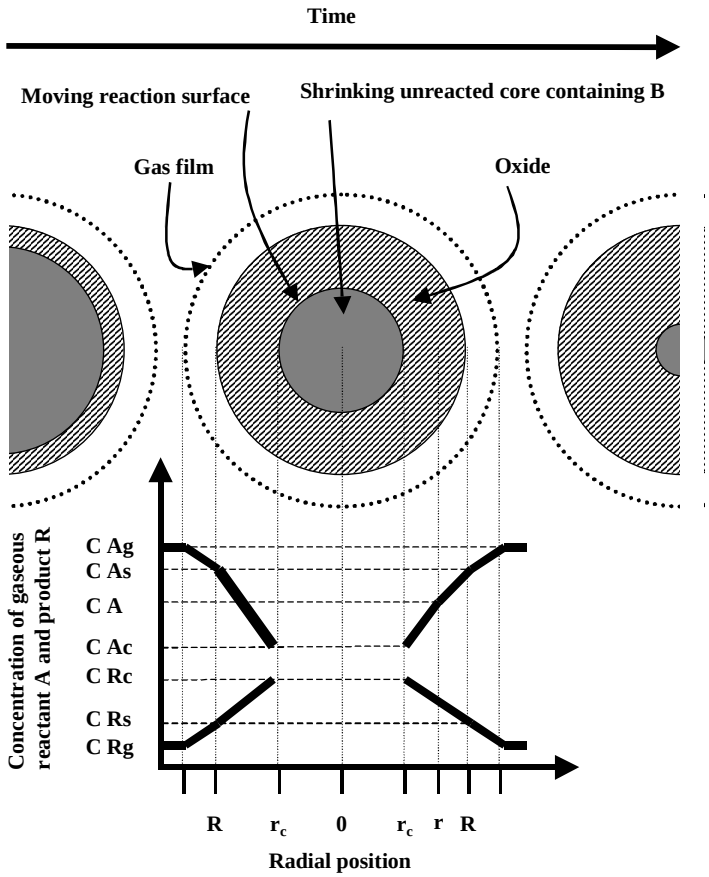

Graph.: 5-1 Concentration profiles of reactants and products for the reaction

A(g) + bB(s) → rR(g) + sS(s)

for a particle of unchanging size[82].

(28)

$$\frac{1}{\tau} = 1 - \left(\frac{r_c}{R}\right)^3 .$$

Equ.: 5-2

This can be re-written in terms of a fractional conversion, X_B, using equation 29 (Equ.:5-3).

$$(29) \qquad 1 - X_B = \left(\frac{\text{volume of unreacted core}}{\text{total volume of particle}} \right) = \frac{\frac{4}{3}\pi r_c^3}{\frac{4}{3}\pi R^3} = \left(\frac{r_c}{R} \right)^3 .$$

Equ.: 5-3

Therefore, the time for complete reaction of the particle is given by equation 30 (Equ.: 5-4).

$$(30) \qquad \frac{t}{\tau} = 1 - \left(\frac{r_c}{R} \right)^3 = X_B \text{, and}$$

$$\frac{t}{\tau} = 1 - 3\left(\frac{r_c}{R} \right)^2 + 2\left(\frac{r_c}{R} \right)^3$$

Equ.: 5-4

5.1.2 Diffusion through an oxide layer

The second possible diffusion resistance to oxidation that may occur is the diffusion through the formed oxide layer around the unreacted metal core (Graph.: 5-2). This mechanism is based on the difference between the rate of the core shrinkage and the rate of diffusion of reactant A through the oxide layer. It is assumed that diffusion of A is faster than the core shrinkage. The overall reaction rate is then related to the ratio of these two rates and a concentration gradient of A in the oxide layer has to be concerned. This leads to the assumption of quasi steady state conditions for diffusing A and for any radius of the core.

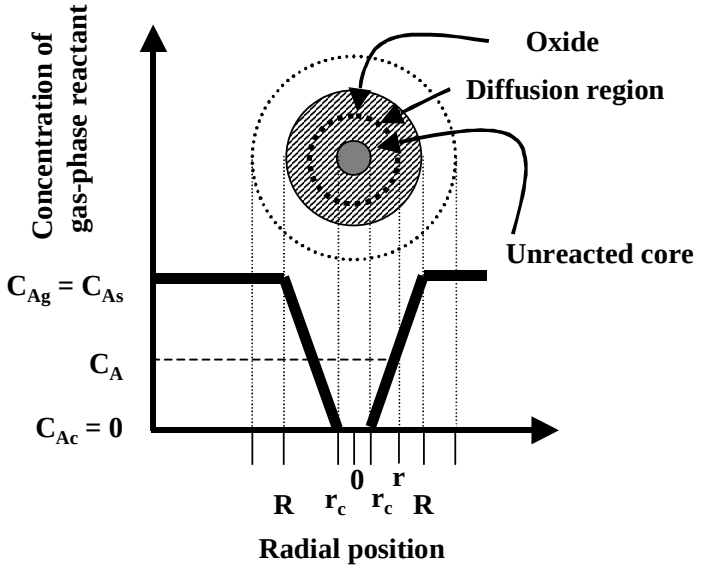

Graph.: 5-2 Levenspiel model for diffusion controlled reaction[82].

The radius of the unreacted core and the time required for complete conversion is defined by equation 31 (Equ.: 5-5) and the mechanism drawn in graph. 5-2.

$$(31)\ \frac{t}{\tau} = 1 \quad 3\left(\frac{r_c}{R}\right)^2 + 2\left(\frac{r_c}{R}\right)^3$$

Equ.: 5-5

5.1.3 Chemical reaction control

The reaction is independent of gas film and oxide layer diffusion and only depends on the chemical reaction rate. The quantity of reacting material is proportional to the available surface of the unreacted core under the assumption that the reaction occurs solely at the interface. The corresponding formalism is given by equ. 32 (equ. 5-6). The mechanism is depicted in graph. 5-3.

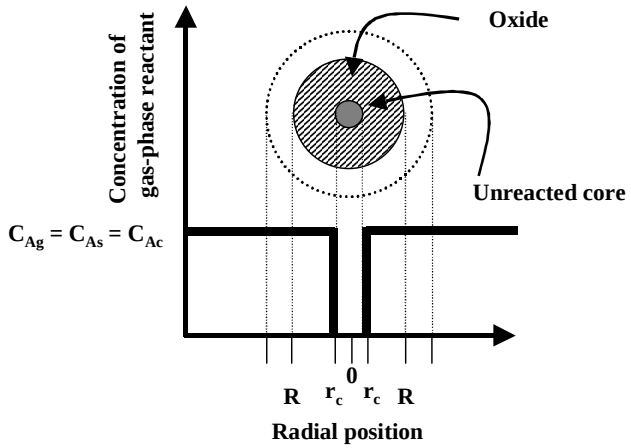

Graph.: 5-3 Levenspiel model for chemical controlled reaction[82].

$$(32)\ \frac{t}{\tau} = 1 - \frac{r_c}{R} = 1 - (1 - X_B)^{\frac{1}{3}}$$

Equ.: 5-6

5.2 Crystallographic model: Pilling-Bedworth-oxidation

The crystallographic model describes the removal of a highly facetted, oxidic shell from a highly facetted, metallic core. This effect is the well known Pilling

and Bedworth mechanism for the oxidation of metal surfaces[86]. This model is based on the reaction of gas phase A with solid B to form an oxidised solid product P. The goal of this model is the exact determination of the origin of the oxide growth stress. Reasons proposed for this stress are the volumetric difference between the oxide and the metal, the concentration gradient of ions in the shell, vacancy injection into the metal, and the formation of new oxide at the grain boundaries of the already existing oxide shell (Graph.: 5-4)[87].

The Pilling-Bedworth ratio (PBR) is the ratio of mass and density of the product P times the inverse ratio of mass and density of the starting material B (Equ.: 5-7).

$$PBR = \frac{\beta_P M_P}{\rho_P} \frac{\rho_B}{\beta_B M_B} \qquad (33)$$

Equ.: 5-7 Pilling-Bedworth ratio (PBR).

$$\beta_A A_{(g)} + \beta_B B_{(s)} \leftrightarrow \beta_P P_{(s)}$$

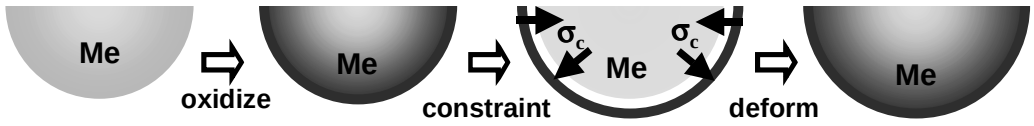

Graph.: 5-4 Model for application of the PBR ratio to spherical particles.

The model is developed for the case that the PBR is larger than unity, i.e. the growth of an initially thin oxidic layer to a thick oxide shell. Because the volume of the oxide is bigger than the volume of the metal, the oxide occupies a surface area larger than that of the metal substrate under hypothetical stress-free conditions. Hence, the oxide is compressed in order to occupy the same surface area as the metal surface. This compression results in a spherical, mechanical strain within the oxidic shell (graph. 5-4). In order to maintain this strain rate constant, radial stress is built up. In case of PBR>1, e.g. the oxidation of copper to CuO or Cu_2O, this stress is compressive. In order to maintain equilibrium, the spherical, compressive stress whthin the shell has to be balanced by a spherical, tensile stress in the metal (Equ.: 5-8).

(34) $S(total) = S_x (elastic) + S_y (creep) + S_z (volume)$

(35) $S_z (volume) = f[(PBR)^{1/3} - 1]$

Equ.: 5-8 Relation of the volume stress and the Pilling-Bedworth ratio.

This system of co-existing stresses leads to the removal of the oxide shell from the metal core. The total stress can be separated in an elastic, S_x, a creep, S_y, and a volume stress, S_z. The PBR is related to the volume stress, S_z (35, Equ.: 5-8). Because of the assumption of an isolated metal sphere in this model, it is insufficient with respect to parallel processes which certainly occur during catalytic reactions, e.g. particle sintering.

5.3 Metallurgical model: Nabarro-Herring and Coble creep

The oxidation of spherical particles is extended by the physical description of particle sintering. Sinter-kinetics can be described by several models[88]. The fundamental model is that developed by Nabarro and Herring[89], or Coble[90]. Sintering is described by a flow of vacancies either through the crystal lattice (Nabarro-Herring diffusion creep) or along the grain boundaries (Coble diffusion creep). The observable material shrinkage during sintering is a pressureless process. It is caused by the minimisation of the free energy due to the reduction of internal and external surfaces. The shrinkage highly depends on the morphology and composition of the powder particles, i.e. intrinsic and extrinsic parameters[91].

The driving force for the two possible creep mechanisms of porous materials is the Laplace pressure[92] σ (see equation 36, Equ.: 5-9).

(36) $$\sigma = A_0 \frac{2\gamma_S - \gamma_{GB}}{\overline{L_P}} \Theta$$

Equ.: 5-9 Laplace pressure

γ_s and γ_{GB} are the surface and grain boundary energies, respectively, L_P is the average powder particle size, Θ is the porosity, and A_0 is a number (1,..., 4,

according to the particle geometry, with A_0=4 for spherical particles). Usually this equation describes the driving force during the intermediate stage of sintering. For Nabarro-Herring and Coble creep, the estimated shrinkage rates are given by equation (37) (Equ.: 5-10) and equation (38) (Equ. 5-11).

$$(37)\quad \dot{\varepsilon}_{NH} = A_1 \frac{D_{vol}\Omega\sigma}{k_B T}\frac{1}{\overline{L_G^2}}$$

Equ.: 5-10 Nabarro- Herring equation

$$(38)\quad \dot{\varepsilon}_{NH} = A_1 \frac{\delta_{GB} D_{GB}\Omega\sigma}{k_B T}\frac{1}{\overline{L_G^3}}$$

Equ.: 5-11 Coble equation

L_G is the average crystallite size, and D_{vol} and D_{GB} are the volume and the grain boundary diffusion coefficients, respectively; A_1 and A_2 are empirical constants, Ω is the atomic volume, σ the external or internal (porous-body) tension, δ_{GB} the effective grain boundary width, k_b the Boltzmann constant, and T the absolute temperature.

The use of spherical particles also allows the application of a geometric model[93], developed for the pressure behaviour of spheres[94] to obtain information about changing morphologies. It estimates the shrinkage rate from the experimental shrinkage by equating the fraction of volume lost from an initial particle of radius, R, at the contact boundary (V_1) and transported toward the neck (V_2) expressed by the neck curvature r (Graph.: 5-5).

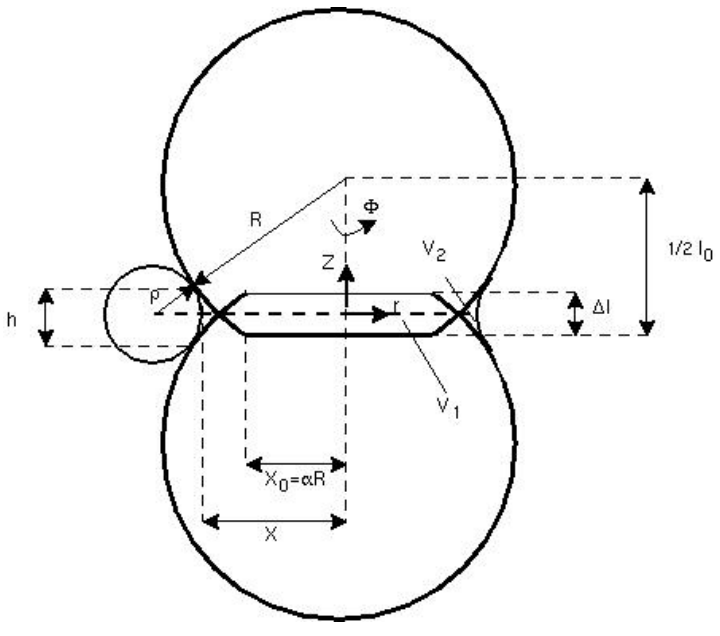

Graph.: 5-5 Two-particle model for Nabarro-Herring/Coble-sintering.

The flattening of both particles at the contact zone is described. α is the so-called initial flattening. X_0 and l_0 are the neck radius and the particle distance after sintering. The volume V_1 is transported to the neck region where it is deposited (V_2). Hence, the outer neck radius, ρ, the inner neck radius, X, and the neck heights, h, are enlarged during sintering.

Considering Ficks law and appropriate boundary conditions, an equation for the shrinkage rate is obtained. The boundary conditions are:

a) the vacancy concentration near the neck is above the equilibrium value due to the principal radii of curvature (ρ, X), and,

b) the sinter-neck has to be free of tension, σ, leading to a vacancy concentration in the middle of sinter-neck, which deviates by the same amount from the equilibrium value as the neck surface, but with the opposite sign.

The exact form for the shrinkage rate is then given by equation (39), (Equ.:5-12)

$$\frac{d}{dt}\left(\frac{\Delta l}{l_0}\right) = 2\left\{-\exp\left[-\frac{\Omega\gamma_S}{k_B T}\left(\frac{1}{\rho}-\frac{1}{\mathrm{X}}\right)\right]\right\} + \exp\left[\frac{\Omega\gamma_S}{k_B T}\left(\frac{1}{\rho}-\frac{1}{\mathrm{X}}\right)\right]\frac{1}{\mathrm{X}^2 R\sqrt{1-\alpha^2}}\int_{-h/2}^{h/2} D_{eff}(t,z)dz \tag{39}$$

Equ.: 5-12

with

(40) $l_0 = 2R\sqrt{1-\alpha^2}$, being initial length $l_{0,}$

Equ.: 5-13

and with R being the particle radius, and $\alpha = X_0/R$ is the flattening after catalytic action where X_0 is the initial neck radius.

5.4 Surface science model : Restructuring

Metal catalysts may undergo different types of restructuring processes, e.g. thermal and catalytic restructuring. Catalytic restructuring is generally defined as any surface reconstruction that only takes place during catalytic reactions. Thermal restructuring is defined as occurring in the absence of chemical reactions with the gas phase[95]. Catalytically induced morphological changes include the formation of non-equilibrium surface structures, such as pits, protrusions, particle fragmentation, weight losses, deep pore formation, and faceting[96].

Detailed investigations on catalytic restructuring were published only for a few metals like silver[97, 98], platinum[99] or copper, for different catalytic reactions. A very pronounced reconstruction of Cu was observed in hydrogen/oxygen atmospheres[100]. The roughening of Cu(110) and Cu(100) surfaces was observed at temperatures around 450°C[101, 102]. Even the early investigators in this filed observed that surface restructuring is influenced too by other macroscopic mechanisms, especially in case of copper due to its facile oxidation.

The material transport mechanisms for reaction induced restructuring are comparable to that of sintering, e.g. diffusion, evaporation-condensation, and plastic or viscous flow. The reduction of the total surface free energy is the requirement for a surface of a given macroscopic orientation to reconstruct into two new surfaces of different orientations[103]. Thus, a randomly oriented surface may reconstruct into a faceted surface with all facets corresponding to equilibrium surface planes present at thermal equilibrium. Therefore, a randomly orientated surface will often decompose into two or more low-indexed planes[104].

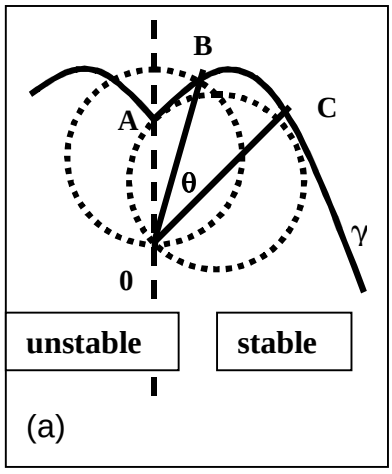

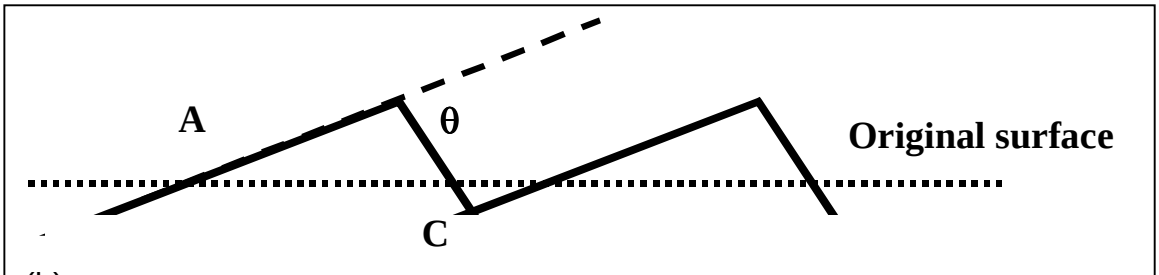

Graph.: 5-6 - Herring's tangent sphere construction for determination of the stability[95]

The requirement for a surface of a given macroscopic orientation B to break into two new surfaces of orientation A and C is that the total surface energy be reduced. The surface stability can be modelled by the tangent sphere construction of Herring[95] (see Fig. 5-14 a, Equ. 5-15)

$$(41)\ \gamma_A S_A + \gamma_C S_C < \gamma_B S_B$$

Equ.: 5-14 Basic Herring equation for surface tension[95].

where γ and S are the surface tension and the surface orientation of A, B, or C.

The stability can be treated in terms of tangent sphere construction in the polar γ plot. The surface of orientation, B, is unstable because the sphere (dashed circle) constructed through the origin, O, and the tangent to the area plot (dashed line B-O) at point, B, is intersected by the area plot. The surface orientation, C, is metastable because the tangent sphere (dashed circle) lies within the area plot Fig 5-15 shows a magnification of the situation at surface C.

5.5 Kinetic model: Nucleation

Crystallisation is occurs by nucleation and growth. One basic rule for the mechanisms was developed by Ostwald, who pointed out that " if the super saturated state has been spontaneously removed, then, instead of the solid phase which is thermodynamically stable under given conditions, a less stable phase will be formed"[105]. This rule can be transferred to the reconstruction of metal surfaces[106]. Solid state transformations occur by nucleation and subsequent growth of a second phase either in the volume or at an interface[107, 108]. The reaction kinetics may be controlled by the interface as in case of re-crystallisation in plastically deformed metals, by crystallisation as in metallic glasses, or by diffusion as in case of second-phase precipitation. For either type of kinetics, analysis is possible by the nucleation theory developed independently by Kolmogorov[109], Johnson and Mehl[110], and Avrami[111]. Accordingly, this kinetic model is called JMAK kinetics[, 112, 113].

The kinetic problem can be summarised as follows[112]:

a) phase transformation occurs by nucleation and growth processes;

b) nucleation seeds are randomly distributed throughout the volume;

c) the nucleus critical size is zero;

d) growth and the nucleation laws are assumed to be given a priori.

This theory assumes that the growth of the second-phase stops when contacting the surface of the same phase. The transformed volume V^{tr} can be described as (equ.: 5-15)

(41) $dV^{tr} = [1-(V^{tr}/V)]dV^{ex}$,

Equ.: 5-15 Johnson-Mehl-Avrami-Kolmogorov model. Description of the transformed volume V^{tr}.

with the extended volume V^{ex} being the volume of all isolated growing particles. Integrating this expression and normalisation to unit volume yields the basic JMAK equation for the transformed volume fraction, f. (Equ.: 5-16)

(42) $F = 1-\exp(-f^{ex})$,

Equ.: 5-16

with $f_{ex} = V^{ex}/V$. The particle growth mechanism is implicit in V^{ex} and can be determined, in principle, from the slope of the line obtained by plotting experimental values of log[-ln(1-f)] vs. log(t), with t being the time.

For example, f^{ex} equals $(4/3)\pi N(Gt)^3$ in case of spherical particles of density, N, and a constant growth rate, G, which is typical for an interface-controlled reaction. The exponent of t, and thus the slope of the line, is 3[114]. It was shown that under other conditions[115], such as continuous nucleation, growth in less than three dimensions, and heterogeneous nucleation on planar or linear defects lead to other exponents for t[116]. In practice, the behaviour of a given material shows a deviation from the expected linear dependence on log (t), which is ascribed to experimental conditions.

6 Kinetics

6.1 Model independent kinetic analysis

One of the main problems for the understanding of redox processes of catalysts is the exact determination of the reaction kinetics. Problems often arise from the uncritical use of the general kinetic approach, not taking into account the implement basic assumptions. As pointed out, changing morphologies can be influenced by several chemical, physical and metallurgical processes. Moreover, it is difficult to exactly express concentration profiles in the solid. Mathematical descriptions of these phenomena are given by several model-dependent and model-independent theories. Simplified models of reactant/product interface movement within hypothetical bodies have to be introduced in the kinetic analysis. One basic assumption in every kinetic investigation is the mechanism of the transformation. This limiting factor emphasises that model reactions often have to be used for the determination these processes simulating catalysis, for which the exact kinetics of these processes are often unknown. Thus, the obtained kinetic parameters rather correspond to the chosen idealised model than to the real catalytic process. Consequently, the available kinetic data is often meaningless with respect to catalysis. Their applicability to reaction mechanism studies have to be considered with care.

From this point of view, more attention should be paid to the formal kinetic analysis[117], i.e. the reaction rate is expressed as a function of time and temperature using empirical functions. In this case, the exact knowledge of the real reaction mechanisms is not necessary at first. Unfortunately, conventional kinetic methods do not permit an unambigious formal analysis[118]. As a rule, several kinetic models often provide similar statistical quality of data approximation, however, with quite different sets of kinetic parameters. To obtain a sufficient solution of a problem the application of several different models is necessary. Even the critical comparison of the obtained data gives only a view to the real process but not an exact mechanism description.

Usually, the basic equation of homogeneous kinetics is applied to the kinetic treatment of solid state processes (Equ.: 6-1)[119].

(43) $d\alpha/dt = k(T)f(\alpha)$,

Equ.: 6-1 basic equation for solid state kinetics.

with α being the degree of conversion.

Assuming the validity of the Arrhenius equation ($k = A \exp(-E_a/RT)$), the following rate equations (Equ.: 6-2, and 6-3) may be written for kinetic measurements at constant heating rates β :

(44) $d\alpha/dt = A \exp (E_a/RT)f(\alpha)$, or

Equ.: 6-2

(45) $g(\alpha) = AE_a/\beta R \exp(-x)[\pi(x)/x]$,

Equ.: 6-3

with $x = E_a/RT$ being the reduced activation energy and $p(\chi)$ being the temperature integral approximation which has to be introduced because Equ.: 6-2 cannot be solved exactly. The $f(\alpha)$ and $g(\alpha)$ functions (Equ.: 6-3) are derived on the basis of different models of the reaction interface movement. The corresponding mathematical expressions are well known[120].

The aim of the kinetic analysis of solid state reactions is the selection of the $f(\alpha)$ and $g(\alpha)$ functions, which give the best approximation of experimental data. The disadvantage that several kinetic models provide a similar description of the studied processes is caused by a strong interrelation between the used kinetic functions[121]. Often the choice of an appropriate model based on additional information, e.g. morphological studies, is hampered by the discrepancies between the real process and idealised models.

The model independent kinetic analysis, on the other hand, leads to an estimation of the activation energy without the definition of a detailed model for the reaction pathway. This seems to be the way of choice to bypass the model-inherent problems. But also in this case assumptions are necessary for a scientifically useful result. For instance, one assumption is that the same product is obtained irrespective of the heating rate.

1.1.1 Kissinger method

The basic assumption for this method is that the maximum conversion rate of a single step reaction is independent of the heating rate[122]. When plotting the logarithm of the heating rate vs. the reciprocal absolute temperature of the maximum rate a line is obtained whose slope is proportional to the activation energy[123] (see Equ. 6-4)

(46) $dx/dt = A(1-x)^n e^{(-E/RT)}$

Equ.: 6-4 Kissinger basic equation

1.1.2 Friedman method

Friedman suggested another appropriate model for the isoconversional analysis[124]. It follows directly from the logarithmised form of the Arrhenius equation (Equ. 6-5).

(47) $\ln (d\alpha/dt) = -E_a/RT + \ln[A\ f(x)]$,

(48) $\ln t = -E_a/RT + \ln[A / g(\alpha)]$

Equ.: 6-5 Basic Friedman equation.

Linear relationships of ln ($d\alpha/dt$) vs 1/T and ln t vs 1/T with slopes proportional to E_a can be established from different temperature-programmed data for which the same value of $\alpha = \alpha_k$ = const was reached. The transformation of equation 6-6 leads to an estimate of lnA for a 1st order reaction (f(x) = (1-x).

(49) $\ln (d\alpha/dt) = -E_a/RT + \ln[A\ f(x-1)]$

Equ.: 6-6 Friedman equation for reaction of 1st order.

A detailed interpretation of the Friedman analysis, i.e. the slope of the calculated curves, allows an interpretation for further model-dependent analysis, like auto-catalytic processes or multi-step reactions.

1.1.3 Ozawa-Flynn-Wall method

The method suggested by Flynn and Wall[125] together with Ozawa[126] can be applied for temperature-programmed experiments with different heating rates, β,. Equ.: 6-7 follows from Equ.: 6-6 and the Doyle approximation[127]

$$\ln\beta = \ln(AE_a)/R - 1.052\, E_a/RT - 5.33 - \ln g(\alpha) \quad (50)$$

Equ.: 6-7 Ozawa-Flynn-Wall equation

A plot of ln β_i vs $1/T_{ik}$, which corresponds to the chosen value $\alpha = \alpha_k$ = const., should yield a straight line with a slope proportional to E_a.

These three models can be applied without knowledge of the true f(α) and g(α) functions, implying a great advantage. However, these three models have to be invariant for all considered experiments. If this is not fulfilled, an apparent activation energy is calculated, which differs from the true value. Hence, the three models were derived mainly for the description of single step reactions[128]. The application to multistep reactions leads to apparent activation energy values which are affected by all reaction steps and change with respect to α [129]. A non-linear regression analysis with fixed activation energy values or an analysis using y(α) and y(α) functions are suitable[130]. The calculated model-independent values for E_a allow thus an unambiguous choice of the appropriate kinetics.

6.2 Model-dependent kinetic analysis

The pre-assumption of one ore more kinetic models that include a special type of physicochemical process like nucleation, or diffusion, leads to model-dependent kinetic analysis. The right choice of the model depends on additional information obtained from other techniques, like XRD or SEM/TEM. In the following

scheme some different reaction pathways for an one-step, two-step, and three-step reaction are listed together with some of the models mostly described in the literature. The equations given are based on the Arrhenius equation (Equ.: 6-8),

$$de/dt = -A \exp(-E/RT) * f(e,p) \quad (51)$$

Equ.: 6-8 Basic reaction equation

with e being the concentration of the starting material and p the concentration of the product.

No.	f(e,p)	Type of reaction
1	**e**	Reaction 1.-degree
2	**e^2**	Reaction 2. degree
3	**e^n**	Reaction n.-degree
4	**$2e^{1/2}$**	Two dimensional phase boundary diffusion
5	**$3e^{2/3}$**	Three dimensional phase boundary reaction
6	**0,5/(1-e)**	On dimensional diffusion
7	**-1/ln(e)**	Two dimensional diffusion
8	**$1,5e^{1/3}(e^{-1/3} -1)$**	Three dimensional diffusion (Jander)
9	**$1,5/(e^{-1/3} -1)$**	Three dimensional diffusion (Ginstling-Brounstein)
10	**e p**	Prout-Tompkins equation
11	**$e^n p^a$**	Enhanced Prout-Tompkins equation
12	**E(1+Kcat X)**	Reaction first degree with auto-catalysis by reactant X
13	**e^n(1+Kcat X)**	Reaction n.-degree with auto-catalysis by reactant X
14	**$2\ e(-\ln(e))^{1/2}$**	Two dimensional nucleation
15	**$3\ e(-\ln(e))^{1/3}$**	Three dimensional nucleation
16	**$n\ e(-\ln(e))^{(n-1)/n}$**	n-dimensional nucleation (Avrami-Erofeev)

Tab.: 6-1 Types of reactions for model dependent analysis

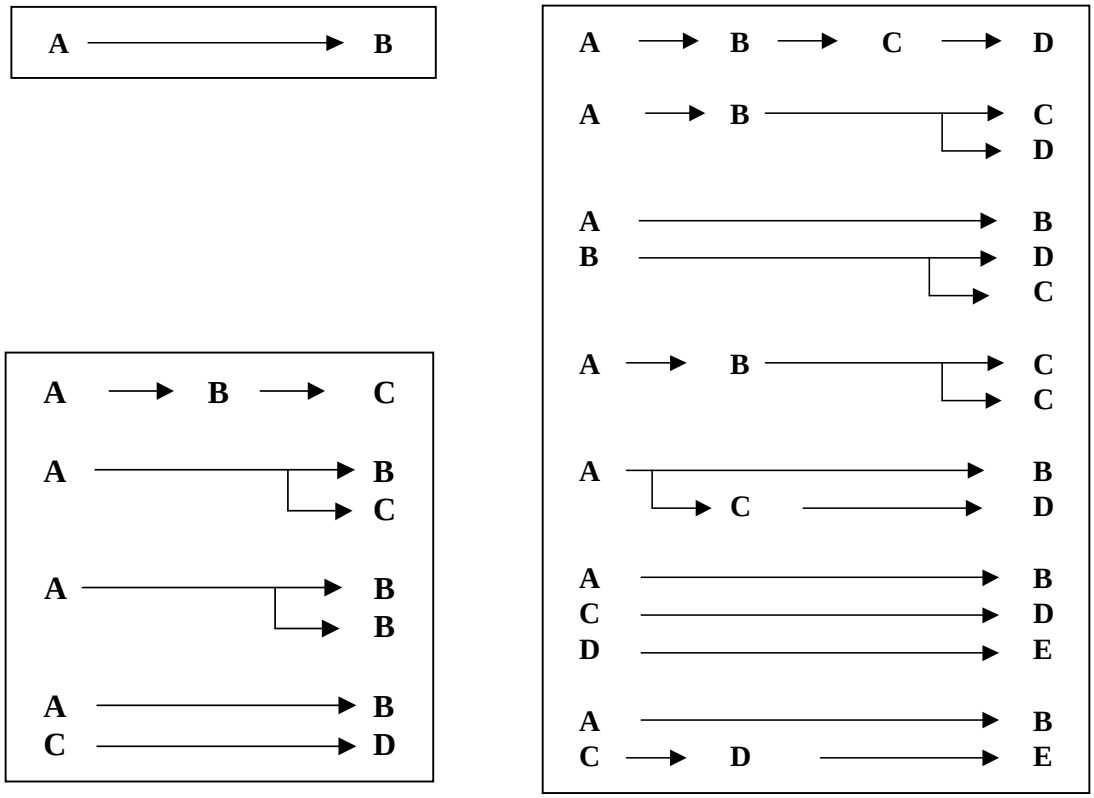

Graph.: 6-1 Set of schemes for single, double and triple step reactions

6.2.1 Diffusion model

Diffusion is usually slow in condensed phases irrespective of the chemical bonding, with the exception of some ionic transport reactions. Solid reactions, thus, are likely controlled by diffusion. The reaction of a metal surface with the gas phase to a solid product, however, is not always diffusion controlled. For example, tarnishing reactions tend to be controlled by diffusion only in cases of dense shells. Then the reaction rate is usually dependent on the low ionic or electronic conductivity[131]. Excessive volume changes or lattice mismatches often yield a porous shell, which, in this case, grows linearly with time as expected for interface control. Hence, mass transport in the gas phase is fast opposite to the interfacial reaction. The growth of a dense shell may also be reaction controlled. Several quasi-steady state models were developed in the literature for the explanation of solid state reactions. Most frequently used are the models of Jander[132], Valensi[133], Ginstling and Brounshtein[134], and Prout and Tompkins.

6.2.2 Nucleation model

The so-called “extended volume concept” for n-dimensional nucleation developed by Avrami and Erofeev[135, 136, 137] was already described in chapter 5 on the JMAK mechanism. This method can be applied to isothermal as well non-isothermal processes[138], which renders possible its use for TPR as well as catalytic reactions.

6.2.3 Mathematical estimation of the model correctness

The estimation of kinetic parameters should be based on a correct physicochemical model to ensure that the calculated data reasonably describe the process. As pointed out, this is almost impossible for complex reaction sequences. The kinetic parameters determined by the applied models were correlated with their standard deviations and to estimate their reliabilities[139]. This approach was realised using the Netzsch software programme for kinetic analyses.

7 Experimental methods

The inter-disciplinary character of catalysis in the field of sciences is emphasised by the broad spectrum of techniques that are used to answer the present questions. These techniques can be separated in three groups. Temperature-programmed desorption (TPD), photoelectron spectroscopy (XPS,UPS), electron back scattering diffraction (EBSD) and electron microscopy (TEM, SEM) belongs to the surface sensitive techniques that are used under ultra high vacuum conditions. Temperature-programmed reduction/oxidation (TPR/O), thermogravimetry (TG/DTA), Brunauer-Emmett-Teller Adsorption (BET) and the third one with diffusive reflection (UV/Vis), and X-ray diffraction (XRD) can characterise the bulk and surface together and are used under normal pressure conditions. Additional analytical methods like gas chromatography (GC) and mass spectrometry (MS) are used for reacting gas phase analysis. The preparation of the Cu-samples can also be differentiated into groups. Not only the chemical or physical preparation

of the starting material but also the treatment in a reactor system is most important for a detailed characterisation. The development of different reactor-systems and their comparison is as important as the catalyst characterisation. Physicochemical properties of the catalyst material can be dramatically changed under catalytic reaction conditions. The characterisation of the material before and after catalytic action is usually not sufficient to understand how the catalyst activity does develop and hence can be understood. In situ techniques are increasingly in the focus of catalysis research in recent years. In this context, not only the quantitative analysis of the gas phase but also the catalysts characterisation is possible at the same time.

7.1 Surface sensitive methods

7.1.1 Thermal Desorption Spectroscopy (TDS)

This method, denoted as Temperature-programmed desorption, TPD[140] if done at normal pressure TPD is able to determine the interaction between the surface and the gas phase[141]. This interaction is described by an adsorption-desorption-equilibrium. The amount of particles n which are adsorbed on the surface is defined by the surface coverage Θ:

(52) $\Theta = n_a/n_s$,

Equ.: 7-1

with n_a= the number of adsorbed particles and n_s= the number of substrate atoms.

At equilibrium, Θ depends on pressure p and temperature T (Langmuir adsorption-isotherm):

(53) $\Theta = f(p/T)$

Equ.: 7-2

If the pumping speed is infinitely high, readsorption may be ignored , and the relative rate of desorption, defined as the change of the in adsorbate coverage per unit of time, is given by (Equ.: 7-3).

$$r = -\frac{d\Theta}{dt} = k_{des}\Theta^n = \nu(\Theta)\Theta^n \exp\left(-\frac{E_{des}(\Theta)}{RT}\right)$$

$$T = T_0 + \beta T$$

Equ.: 7-3 relative rate of desorption

In which

r	is the rate of desorption
θ	is the coverage in monolayers
t	is the time
k_{des}	is the reaction rate constant for desorption
n	is the order of desorption
ν	is the preexponential factor of desorption
R	is the gas constant
T	is the temperature
T_0	is the temperature on which the experiment starts
β	is the heating rate, equal to dT/dt. [142]

The adsorption energy and the differential isosterical adsorption enthalpy depends on the concentration of the adsorbed particles and the temperature. Experimentally, this value can either be directly determined by adsorption calorimetry or by the determination of the activation energy of the desorption process. In general, adsorption is differentiated in chemisorption (E_{ads}≈60-250kJ/mol) and physisorption (E_{ads}<20kJ/mol). Due to the chemical interaction of the surface and the adsorbate, non-dissociative and dissociative chemisorption is observed[143].

The desorption process is monitored in the TDS experiment by the changing partial pressures in the UHV chamber as a function of the sample temperature (ideal gas equation). To minimise re-adsorption, the capacity of the pump system should be higher than the maximum desorption rate from the surface region, which results in a volume V containing the desorbed molecules. The pumping

capacity is defined by the pump rate, the desorption rate S of the molecules desorbing from the surface, and the chamber volume ($S=VdP_p/dt$).

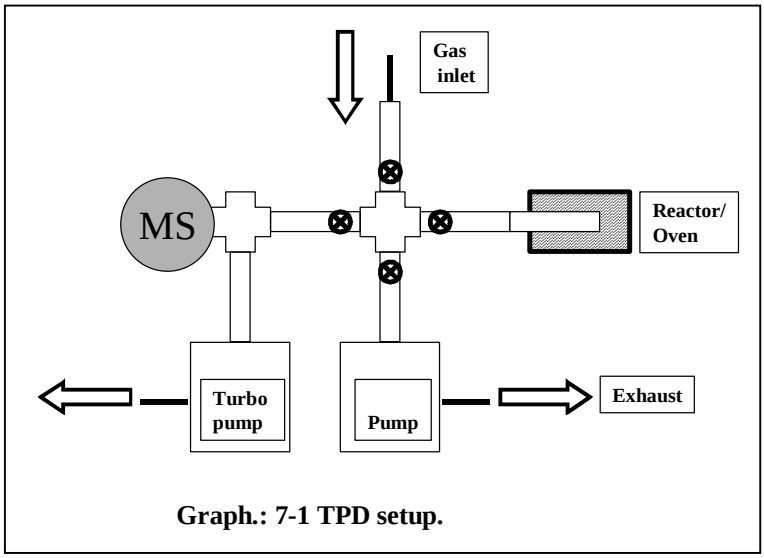

Graph.: 7-1 TPD setup.

The segregation of sub-surface species to the surface and their desorption may complicate the conventional desorption theory in special cases (see Ag surfaces). Also possible morphological surface changes during heating and possible adsorption induced re-constructions, which are removed during desorption are not taken into account by these static theories[144], but may lead to altering desorption energies.

The TPD experiment is shown schematically in Graph. 7-1. It consists of a quartz sample cell which is connected to a mass spectrometer (Hiden Inc.). The quartz cell is centred in a water cooled, reflector oven (Stroehlein Instr.) for temperature-programmed or isothermal treatments. The vacuum is pumped differentially, so that species desorbing from the sample are pumped to the spectrometer. The turbo molecular pump (Balzer's Inc.) is localised directly below the ionisation chamber in order to maximise the sensitivity of the mass spectrometer. The attached of gas dosing system allows sample pre-treatment in a range of pressures from 10^{-4}mbar to 1 bar. Pressures higher than 10^{-4} mbar are recorded using thermal conductivity pressure gauges (Pirani-Balzer's Inc.). Lower pressures are measured with ionisation gauges (Pfeiffer Inc.).

7.1.2 Photoelectron spectroscopy XPS/UPS

Photoelectron spectroscopy is based on the external photoelectron effect. The relation governing the interaction of a photon with a core level electron is described in equation (55) (Equ.:7-4).

(55) $E_k = h\nu - E_b - e\Phi$,

Equ.: 7-4

with E_k being the kinetic energy of the ejected photoelectron, E_b the binding energy of the emitting core level, and $e\Phi$ the spectrometer work function. The fact that all elements show unique binding energies renders XPS possible for the elemental identification and quantification of surface compositions.

A modified spectrometer (Leybold LHS 12 MCD) was used with a base pressure near 10^{-11} mbar and additional facilities for ion scattering spectroscopy (ISS). Non-monochromatised Mg K_α-emission (1253.6eV) was used as X-ray source. A fixed analyser band pass energy of 108eV gave an instrumental resolution of 1.0eV. The binding energy was calibrated using Au 4*f*7/2 (BE=84.0eV). Surface compositions were calculated after subtraction of a Shirley- or Bezier-type background. HeI ($h\nu$=21.2eV) and HeII ($h\nu$=40.8eV) radiation was used for the excitation of UP spectra which were acquired using analyser pass energies of 12 and 24eV, respectively.

XPS/UPS was used for the investigation of the redox behaviour of $Ag_2Cu_2O_3$. For these experiments, the sample pre-treatment in an attached treatment chamber was of main interest. The pre-treatment was based on the reaction conditions, which were determined by TPDRO (see chapter 10.7).

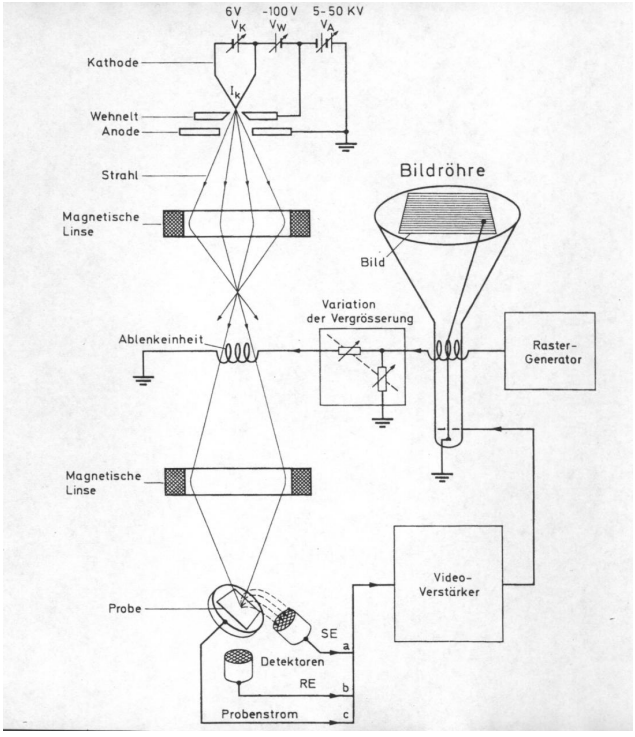

Graph.: 7-2 General SEM set up[145]

7.1.3 Scanning electron microscopy, SEM and Transmission elctron spectroscopy, TEM

The scanning electron microscopy is based on the interaction of electrons with an surface. The produced primary electrons were inelastically and

elastically scattered forced by the interaction with the materials surface. Elastical scattering is characterised by an energy loss of primary beam. The energy loss of the electrons forced by the scattering leads to an continuous background. Additionally, slow secondary electrons were produced (<50eV). These slow electrons can diffuse through a thin surface layer (10-100A). Only this species forms the high resolution picture, because area together with diameter of the primarly beam are well defined. The electrons (<50eV) that were scattered at large atom cores in large angles are called back-scattered electrons. Another group of secondary electrons is emitted during the pass of this electrons through the surface area. The back-scattered and the secondary electrons are formed I an area between 0.1 up to several µm around the primarly beam (electron-diffusion). The signal intensity of these both species is defined by the by the structure of the sample. In the case of transmission microscopy, the character of the first scattered electron type is defined by the thickness of the sample. If the samples thickness is larger than the leaving length of the electron beam, the result is comparable to that for SEM. The contrast is defined by the angle contribution of the transmitted electrons. Additionally the exit of the electrons out of the sample may vary and influence the resolution. The energy spectra of the transmission electrons is used for a detailed view on contrast and element analysis by filtering.

SEM was used for the determination of the sample morphology before and after catalytic action. A SEM S-4000 (Hitachi Inc.) with a field emission gun was used with an acceleration voltage of 15 or 30V. A sample distance of 8 and 18mm was used. For SEM, a heated filament produces a current of electrons which is focussed on the sample through a lense-aperture system[145]. The resolution of the instrument is limited by the diameter of the imaging electron beam. The scanning coils direct the beam across the sample surface. The interaction of the electron beam with the surface leads to the release of secondary electrons and X-rays. The secondary electrons are collected in the SEM detector for sample imaging. The X-rays are used for the determination of the elemental composition, by energy dispersive X-ray analysis (EDX) (EDAX Inc.). The problem of EDX quantification is the low sensitivity for the detection of the light elements. Due to this, the samples were carried in air to the instrument and the quantification of the oxygen content was not attempted.

7.1.4 EDX, element dispersive x-ray diffraction

The elemental dispersive x-ray diffraction is based on the relation of the continuum and the linienspektrum. The continuum is formed by the negative acceleration of electrons in the coulomb-field of a target atom core. The acceleration of charges results in the emission of electro magnetic radiation. Opposite to the x-ray diffraction method the EDX uses the energy dispersive detector system for elemental analysis. For the energy range of 1 to 50eV the Lithium-gedriftet silicium detector is used. The windows are made of an polymer. This detector is formed by the drift of lithium atoms in p-Si. This results in a large p-I-n-transition with an high resistance eigenleitungszone of several milimeters. The transiton is interrupted by an sperrspannnung (100V). This system results in a high energy resolution opposite to comparable scintilizer or proportional detectors.

7.1.5 Electron back scattering diffraction, EBSD

EBSD is a tool to investigate the surface orientation of solids. An electron back scattering pattern (EBSP) shows the angular variation of the intensity of the electrons scattered from a crystalline sample irradiated by an electron beam[146]. It consists of a series of relative intense bands intersecting one another on top of the regular distribution of back-scattered electrons. The diffraction of electrons is comparable to X-ray diffraction. When the electron beam of the microscope irradiates the sample, a divergent source of scattered electrons is generated. All electrons incident at Bragg angles will be strongly reflected. Since the electrons are diffracted by all possible lattice planes many cones of enhanced intensity will leave the sample in a number of directions (graph. 7-3).

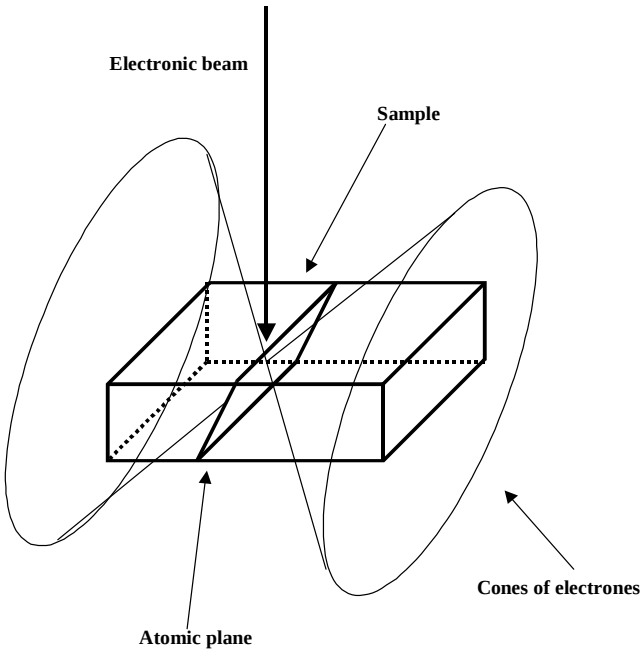

Graph.: 7-3 Electron diffraction model.

Consequently, a point on the EBSP (electron back-scatter spectroscopy pattern) corresponds to a direction in the crystal lattice[147] (graph. 7-4). This Kikuchi pattern arises from the substantial fraction of inelastically and incoherently scattered electrons. Their energy loss is much smaller than the incident energy of the electron. Hence, their electron wavelength is not appreciably changed. Inside the crystal these randomly scattered electrons impinge on the lattice planes from all directions, but preferentially in the forward direction, and can subsequently give rise to Bragg scattering[148].

The EBSD (Oxford Instruments Inc.) attached to the SEM S-4000 gave the advantage to image the surface and to determine its orientation. The illumination area for EBSD was about 0.1 to 1 µm with a penetration depth of ~600Å. A sample size of 25mm to 25mm to 10mm was needed for EBSD. The faceting of copper particle surfaces was investigated by this method. Data interpretation was done by software, which allowed only a low deviation of the stereo plot without data manipulation.

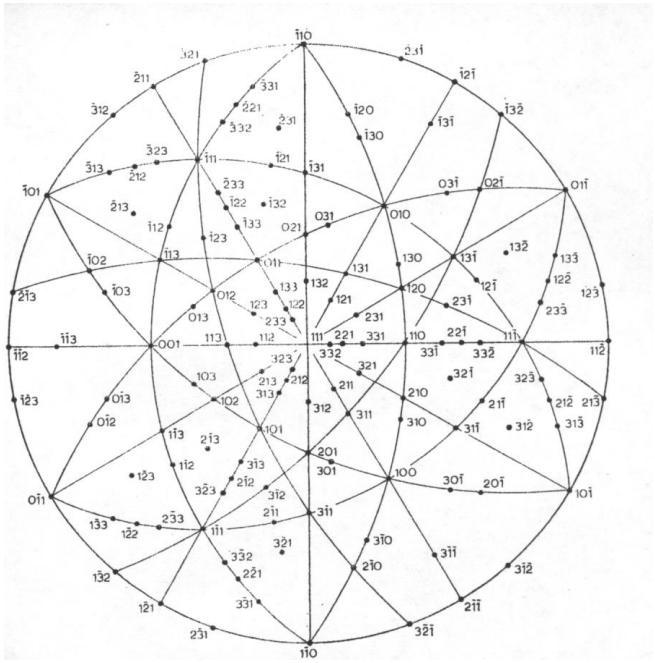

Graph.: 7-4 Stereograph of 111 planes for the cubic system[148].

The measurements were carried out using a EBSD (Oxford Instruments Inc.). The illumination area was about 0.1 to 1 µm with a penetration depth of ~600Å. A sample size of 25mm to 25mm to 10mm was needed.

7.2 Bulk specific methods

7.2.1 X-ray diffraction, XRD

XRD was only used for the characterisation of the oxides before and after catalytic action. (Additional treatment of the samples for XRD analysis see there). A STADI P diffractometer (STOE) was used equipped with an Cu-$K_{\square}$ radiation emitting HOPG-secondary monochromator.

XRD depends on the constructive interference of X-rays at crystal lattice planes. This interaction leads to an diffraction of the X-ray. The constructive interference is described by the Bragg-equation[149] :

(57) $N\lambda = 2d\sin\phi$,

Equ.: 7-5 Bragg-equation

with N being an integer, λ the X-ray wavelength, d the distance between the lattice planes and ϕ is the angle between the incoming X-rays and the normal to the lattice plane.

XRD was mainly used for the determination of the destruction of the cuprates after catalytic action. Data analysis was made using the Stoe data base (Stoe Inc.) for diffraction patterns as well as by literature data. The problem of the high reactivity of copper with oxygen made an XRD investigation of the copper samples after catalytic action impossible. The in situ study of the behaviour of copper during the methanol oxidation and synthesis in comparison to its redox behaviour has been studied elsewhere[150].

7.2.2 Temperature-programmed reduction/oxidation (TPR/O)

The reduction of metal oxides with hydrogen is the basic reaction for the temperature-programmed reduction (TPR). Accordingly, temperature-programmed oxidation (TPO) is the reaction of oxygen with the reduced metal.

The change of the standard free energy for the reduction $\Delta G°$ is negative for most metal oxides and thus reduction is thermodynamically feasible (Equ.: 7-6)[151].

(58)

$$\Delta G=\Delta G°+RT\log(pH_2O/PH_2)$$

Equ.: 7-6 TPR thermodynamics

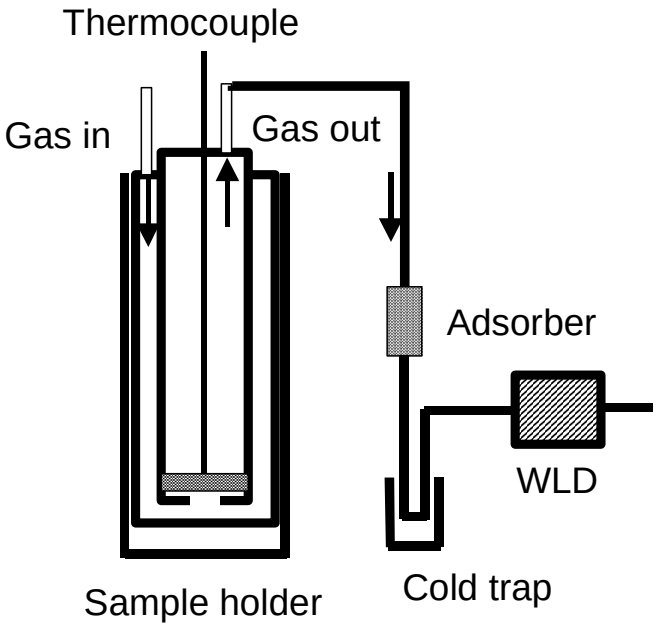

Graph.: 7-5 TPD/R/O set up.

The kinetics of reduction as well as the oxidation can be described by two different models. The redox process can either be ruled by nucleation or contracting sphere processes. Both mechanisms are interdependent. Nucleation finally leads to the contracting sphere, and also the spherical reduction can be described as one large nucleus. Both types can never be observed isolated. The process kinetics are mainly influenced by the reaction conditions, like temperature programme and gas phase[152, 153]. The diffusion through the material may also affect the observed TPR/O traces[154]. Hence, the TPR/O profiles are influenced by the hydrogen or oxygen concentrations, the flow rates, and the heating rates. Variations of the heating rates and of the gas atmosphere allow a detailed analysis of the reaction kinetics[155, 156]. Peak shape analysis also allows kinetic interpretation[157, 158]. The present work was focussed on the variation of the heating rate to obtain information about the kinetics of the redox processes.

A new commercial equipment (TPDRO 1100, CE Instruments Inc.) was tested. The sample was placed in a commercial quartz sample holder. A thermal-conductivity detector was used. Gas mixtures of 5% hydrogen in argon or 5% oxygen in helium were used.

7.2.3 Thermogravimetry/Differential Thermal Analysis,TG/DTA

Like TPR/O, TG characterises weight changes of catalysts as function of atmosphere, flow rate, temperature, and heating rate in isothermal or temperature-programmed experiments. Additionally, information about the exo- or endothermicity of processes can be determined by DTA. Reduction and oxidation of copper catalysts as investigated by TG/DTA are widely discussed in the literature[159].

In the commercial TG/DTA (Seiko Inc.) the balance is placed in a horizontal ceramic tube. The samples were placed in alumina crucibles. It was equipped with a gas mixing panel and mass flow controllers which allowed the investigation of the behaviour of copper catalysts in situ during the methanol oxidation reaction (Graph.: 7-6). The carrier gas line could be directed to an evaporator with methanol. The reactor exhaust was sampled by a capillary and led to an Ion-Molecule-Reaction Mass Spectrometer (IMR-MS; Atomica, Germany). The balance reaction tube was treated like an usual tubular flow reactor.

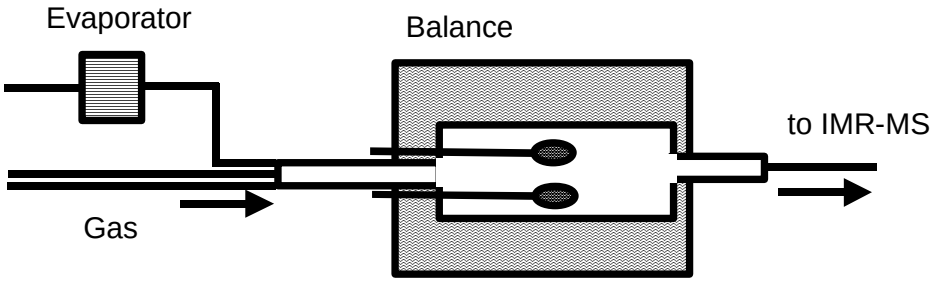

Graph.: 7-6 TG/DTA-reactor for methanol oxidation reaction

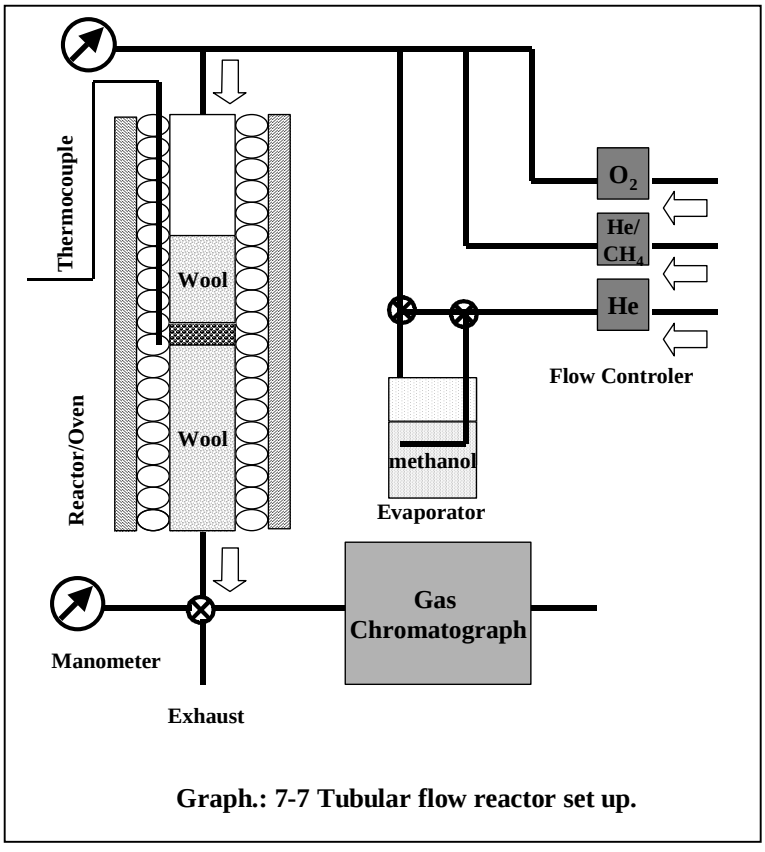

Graph.: 7-7 Tubular flow reactor set up.

7.2.4 Catalytic Reactors

Two different reactor types were used for

the catalytic test reactions. Both reactor types belong to the gas chromatographic types of tubular flow reactors[160]. The difference between both is the way the catalyst is contacted with the organic substrates.

A tubular flow reactor (plug flow) was used for methanol oxidation, oxidative coupling of methane, and alkene oxidation reactions over Cu powders (Graph.: 7-7). It consists of a quartz tube which is heated by a cylindrical oven. The space between tube and inner oven wall was filled with quartz wool pads to minimise temperature gradients over the length of the oven. Two different reactor tube diameters were used, 100mm and 40mm, depending on the amount of catalyst. The catalyst was placed in the isothermal zone in the middle of the oven. The thermocouple was placed directly at the bed outside the quartz tube to prevent the reaction of the reaction gases with the containing Ni and Cr.

The way the catalyst was placed in the reactor tube was also varied to study its influence on the on-set temperature for the reactions. The copper particles were diluted by SiC (silicium carbide) granulates and powders in different ratios. Blind tests showed that the SiC powder, the quartz wool, as well as the empty reactor quartz tube did not lead to conversion at temperatures below 800°C. As documented (see Graph.: 7-8), the influence of dilution on the reaction onset is rather small. Only a reactor prepared using different SiC particle sizes in a “sandwich-style” led a remarkable shift to higher temperatures. Due to these observations SiC was not used for dilution in further experiments especially to render possible a subsequent analysis by SEM/EDX.

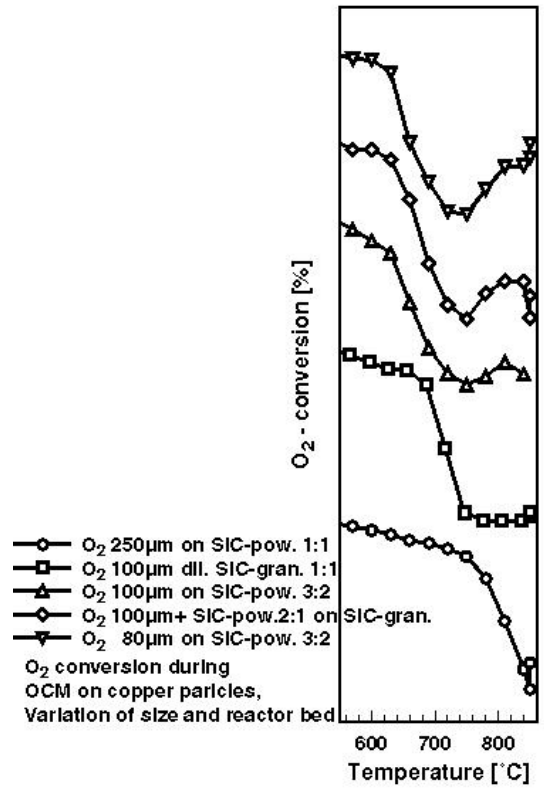

Graph.: 7-8 Influence of SiC to reaction on-set. Curves vertically shifted.

The other reactor type used for the methanol oxidation reaction was an ultra-short contact-time wall reactor[161]. The Cu-reactor tube itself acted as the catalyst[162, 163]. The tube, with an outer diameter of 3mm and a length of 3cm, was placed in the centre of a heated region. The temperature was controlled by an external thermocouple directly placed at the reactor wall.

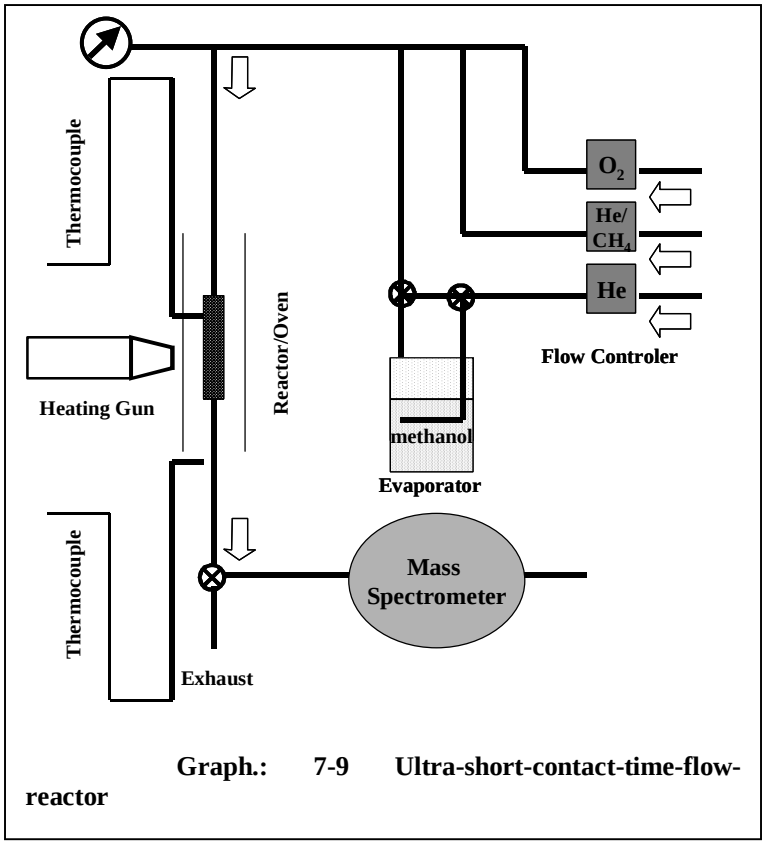

Graph.: 7-9 Ultra-short-contact-time-flow-reactor

This type of reactor had the advantage the possible variations of high flow rates, and an exact definition of the gas–Cu contact by the length of the tube and its diameter.

Two different reactor models or operation modes of a tubular flow reactor can be distinguished, the differential and the integral reactor[164]. The advantage of an integral reactor is the optimisation of the reaction conditions to reach high yields. The differential reactor mode is used at low conversion rates for the determination of reaction kinetics. Tubular flow reactors are integral reactors by principle of design. Accordingly, catalytic data can only be kinetically analysed when operated under differential conditions, i. e. at low conversion rates. Differential interpretation of reaction data means the differentiation of the measured concentration/time-dependence to obtain activation energies and reaction orders of the participating reactants. In this work, integral reactor conditions could not be avoided due to the high conversion rates (100% O_2) in case of the methanol oxidation. Several different model-dependent and model-independent kinetic analysis were applied and are described later.

7.3 Material

Since the development of its phase diagram most of the fundamental investigations on copper in heterogeneous catalysis were focussed on the behaviour of copper under low-pressure conditions using single crystals[56]. However, copper supported on different materials, e.g. in zeolites,[165] or copper compounds gained over pure Cu.

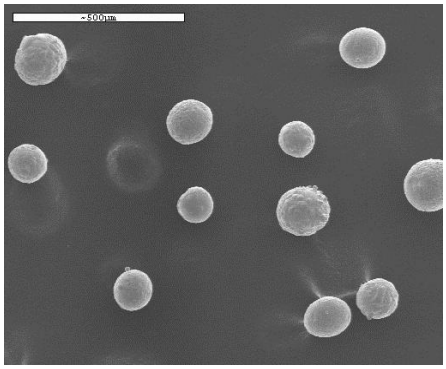

Graph.: 7-10 Spherical copper particles, untreated.

The goal of this study was to show that copper in different catalysts finally exhibits the same behaviour for the same reactions and comparable conditions. Three types of cuprates were chosen to manifest a relation between oxidic copper and copper metal catalysts, the copper aluminate spinel for the macroscopic view on reaction-induced surface segregation of Cu, the perowskite-type oxides for the structural view on reaction-induced reconstruction and Cu formation, and $Ag_2Cu_2O_3$ as an perowskite-related structure for the “combinatorial” view of a possible Ag-Cu synergy either in the oxide or in alloys formed Spherical copper particles of different diameters were chosen as the pure metal for comparison. Spherical particles have several advantages. a) Opposite to supported copper, a chemical preparation is not necessary. b) A sphere is the simplest geometric form that could be imagined for a particle. c) Particle size effects as well as morphological changes during the catalytic reaction can easily be detected. d) The different diameters of the material ranging from 20µm to 250µm allow the transfer between supported “powder-like” copper, on one side, and copper foils or single crystals on the other. e) Spherical particles are comparable to large size commercial Cu catalysts.

8 The macroscopic view: Ceramics

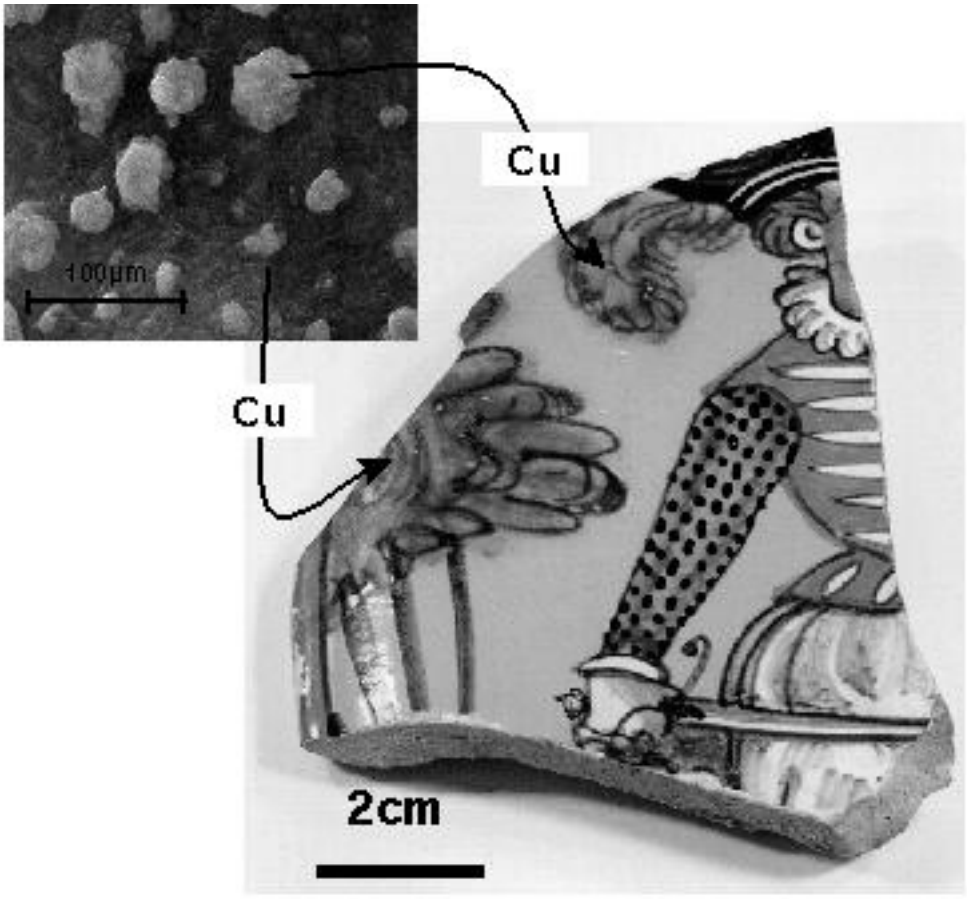

(Majolica sherd decorated in the „Montelupo-style“. The trees and the plumes were analyzed to contain copper in trace amounts. On a white tin containing ceramic layer an engobe painting was added. Finally the painting was coated by a transparent glaze. SEM of a $CuAl_2O_4$engobe after TPR showed poly-crystalline copper particles at the matrix surface. The reaction of these particles with the final coating led to the green colour of the glaze.)

Abstract

Ceramic is one of the most important materials that is produced by mankind for the last past 10 000 years. Its importance is ruled by a wide field of applications. The manufacturing of it is corresponding to its application and to the expected properties. Due to that, many different properties of ceramics are known. Surprisingly, the item itself is not defined. The group of ceramic materials include plates as well as super-conducting oxides. This work is focussed on the elementary common use of ceramics as object for everybody.

The form of the ceramic object is the most important aspect of the ceramic piece. The application defines its decoration. It is human nature to design an object in a way that makes it more precious, describes the use or just labels it. For this and not only the clay itself but also the decoration with coloured coatings were used depending on the preparation process as a technical aspect and according to the historical period the ceramic was produced.

Colour-pigments are very important in our society. It is not possible to imagine any place or thing that has got no decorated surface. Investigations of this topic render necessary the inter-discipline dialogue between scientists of different disciplines. Given the proper question, archaeologists, chemists, physicists and potters have to combine their forces to handle the open problem. The main problem for this interdisciplinary work is based on the different “languages” of the different disciplines. One example is the exact definition of an engobe or a glaze for the decoration of a ceramic object. Cu-Al-Si-O as a model system is of importance for the potter as brown or green coloured pigment. This pigment, $CuAl_2O_4$, was also tested as catalyst for the methanol synthesis and $DeNO_x$-reaction and thus is of importance for science and for application in the chemical industry as well. The formation of this pigment and its transformation at high temperatures in the glass phase may give general informations about the copper oxygen interaction. The determination of the spinel on original ceramic fragments can help the archaeologist to learn about the manufacturing of ancient ceramics.

8.1 Introduction

An engobe is defined as a homogeneous mixture of clay and water[166]. The oxidative or reductive calcination process for its preparation ends at 1000°C. In contrast a ceramic glaze[167] is a coating of glassy material on a ceramic surface. The content of this glass can include different admixtures of compounds according to the wished properties of the resulting object. The preparation of a glaze happens in different calcination atmospheres in the temperature range from 800°C up to 1400°C. The melting of the glaze is, in addition to the temperature and its composition, the most important difference to the character of an engobe. An engobe is exclusively used for the decoration of the ceramic surface, a glaze also a affects its function.

These definitions lead to some questions. Is it possible to differ between both types of coatings by natural science techniques in addition to the usually art-historical more techniques? Are there examples for the application on ceramic products? Does the “engobe” describe a chemical state or a visual character of a ceramic surface? And is there some indicator system that makes it possible to differ between both surfaces, engobe and glaze, without any enhanced professional equipment?

Especially this last point underlines the interdisciplinary aspect of such investigations. The combination of sciences like chemistry, physics, archaeology and the history of arts is combined in an artificial subject called archaeometry, manifested now for several years. Archaeometry means that all these sciences should work together to obtain informations about ancient manufacturing, and conservation of artefacts, the age of the sample[168] and its composition[169]. The increasing environmental pollution as environmental problem and the increasing problems of museums to conserve their different collections make progress in this field urgent. Probably some forgotten techniques of the last centuries could extend modern industrial processes. The durable protection of surfaces is an actual problem in many industrial processes.

The main problem of the most scientific methods used for investigations on precious historical objects is, that they are destroying techniques. That means that a piece of the artefact is needed for the investigation. The size of such “pieces” has

decreased during the last years[170] because of the development of new methods and their increase of sensitivity[171, 172]. The development of transportable RFA- or IR-spectrometer render possible the investigation of the surface of the object directly in a museum or the original situation where it was found. For an archaeologist the surface sometimes is not as interesting as the bulk of the material. According to the age and surrounding conditions if it was buried in an aggressive ground, the consistence of the surface could have been changed. Reliable informations about the original composition of the material are often not possible. To organise the ceramic piece and most important the accompanied objects in an historical context, preparation and use of it are necessary to know. If there is any decoration left on the fragment, without any additional application of scientific equipment an analysis of the manufacturing should be easily possible.

8.1.1 Decoration techniques

It is possible to decorate a ceramic object by different techniques. The coating is of course one of the last steps during the production routine. Decoration is not only a problem of the design but also a physicochemical problem. For this, the clean surface of the ceramic object should fulfil some basic aspects like type, purity, roughness, wetness, composition and colour. All these properties together decide which kind of durable coating is possible.

The perfection of glazing in history is the art of the majolica and fayence of the Italian renaissance period[173]. Influenced by Spanish-Moorish ceramics of the early 12. century these types reach levels of technical perfection and quality until the 18. century that still modern ceramic is influenced by it[174]. After the preparation[175] of the ceramic layer and its drying a fist firing step was done at temperatures between 800°C – 900°C. Than the resulting piece was covered by a tin glaze. The glaze was fixed by drying or a second burning. This tin glaze was not transparent, white or coloured, and had the function neutral ground for the subsequent painting with different types of ceramic colours. The type of the colours defined the temperature of the third burning step. Subsequently, a transparent glaze was added for protection with a fourth burning. The complexity of these process resulted in a highly rate of damaged products and hence an increased value of the perfect pieces. Of course the value was also defined by the decoration and the size. The manufacturing of the

fayence or majolica led to a wide filed of different application of the pigment. It is possible to differ between three types:

a) in-glaze painting: the colours were painted directly to the dry tin glaze and burned together in one step.

b) On-glaze painting: On the already calcined glaze a new layer of painting was added to the object and burned again.

c) Under-glaze painting: The painted object was covered by a transparent last glaze at lower temperatures.

8.1.2 Pigments

One very interesting step in this preparation is the painting with ceramic colours. These colours and their application are subject of many archaeometric studies[176, 177, 178, 179, 180]. The pigment[181] analysis is also known in the investigation of pictures. But in opposite to that for the creation of a ceramic colour the firing process is necessary. Thus chemical reactions during the firing process form the final pigment. The character of these pigments also depends on the character of the surrounding matrices, the calcination atmospheres and the composition of the ceramic pieces. Because of the main importance of ceramics for the human life the prescriptions for many colours are well known[182]. Some production techniques have never really interrupted and just new materials were added due to the parallel progress in material science. A well known example of the use of chromium ($2PbSO_4*PbCrO_4$) for a yellow pigment after its discovery in the beginning of the 19. Century by M.H. Klapproth[183] in Berlin. Some tractates by potters of the 16. century like the text of Picolpasso[184], gives advise how to prepare a glaze or pigment in the majolica-style.

A glaze is a composition of several glass forming substances like known in the glass manufacture. The colour of a glaze is indicated by the addition of trace amounts of transition metal oxides. These oxides dissolve in the glass phase and the electronic interaction of light with the solved ions leads to the colour which is defined by the charge of the ions[185]. The definition for an engobe excludes the sintering or melting processes which are necessary for the formation of a glaze. So the colour of a engobe must be the result of other chemical processes than the dissolution of ions in a glass matrix. In case of an engobe a chemical reaction is responsible for the pigment formation.

For this work, copper was chosen as colour giving ingredient for glazes and engobes. Because copper containing pigments were used for a long time[186] for red, green and blue colours in ceramics.

Several copper containing materials are known, but most of them, as documented in the literature, were used for cold painting, i. e. decoration after the firing process of the ceramic object (Table 8-1).

Name	compound
Malachite[187]	$CuCO_3*Cu(OH)_2$
Paratacamite[,188]	$CuCl_2*Cu(OH)_2$
Egyptian green[189,190]	$CaCuSi_4O_{10}$
Chrysocolle[191]	$CuSiO_3*nH_2O$
Grünspan[192]	$Cu(CH_3COO)_2*nH_2O$

Table 8-1 Summary of copper-containing green pigments for cold painting

The use of copper for ceramic coatings is proved for antique Greek pottery[193] and modern ware until now[194]. Many different authors of handbooks for ceramic classification describe the preparation of masses and engobes[195, 196, 197].

The problem is an insufficient definition of the term “engobe”. In opposite to the primary definition of a homogeneous mixture of clay and water, some other substances are proposed for addition.

For an classic engobe, clay is used which already gives a specific colour by its own when calcined. The basic substances discussed as supporting materials are gypsum, feldspar, quartz, glaze and metal oxides. The character of the raw surface varies between the wet and calcined state depending on the composition or classification of the material. The loss of water during the calcination leads to a strong decrease of weight and volume of the body. This could lead to the destruction or removal of the engobe from the surface of the sherd. One of the most interesting examples for the use of a ceramic coating probably without any additions is the roman *terra sigillata*[198, 199].

As defined above, an engobe is a homogeneous mixture of clay and water. The clay-mineral is the possible reaction partner for an added metal oxide like CuO or Cu_2O. The transformation of the clay mineral due to the temperature should be taken into account. The reaction partner or the matrix for the metal oxides undergoes a stepwise changing. The calcination of a clay mineral is a very complex

reaction and depends also on the kind of the chosen mineral. Clay minerals, belonging to the group of phyllo-silicates contain a different amount of cations and additional salts and carbonates, hence their purification is difficult. To minimise this problem, the kaolinitic system was chosen in this work as sample because the structure[200] is well known.

The colour of the system Cu-Al-Si-O is due to two possible reactions in the investigated temperature range. The first one is the solution of copper ions in a glass matrix formed during the calcination process and the second one is the reaction between Al_2O_3 and Cu_2O/CuO or SiO_2 and Cu_2O/CuO.

The existence of water-free copper-silicate compounds could not be proved until now. The synthesised compounds described in the literature[201] were identified as non-stoichiometric amorphous mixtures of different silicate phases combined with copper oxide[202]. In addition, the formation of a glass matrix[203] with dissolved copper could be detected in amounts.

8.1.3 The system Cu-Al-Si-O

As defined above, the formation of an engobe leads to no glass phase. In this context the system Cu-Al-O is much more interesting. It is a well known fact that it is possible to obtain $CuAl_2O_4$, one possible copper aluminate (Graph. 1-2), by calcination of a mixture of CuO and Al_2O_3 at 900°C for five days[204]. This aluminate crystallises in a cubic space group (Fd3m) and belongs to the partly inverse spinel structure (a_0 : 8.075Å)[205, 206]. The structure of the second aluminate, $CuAlO_2$ belongs to the rhombohedral system (D_3^5d-R3m; a: 5.896Å; α: 28.1°)[207, 208]. The colour of $CuAl_2O_4$ is red-brown, the one of $CuAlO_2$ is blue.

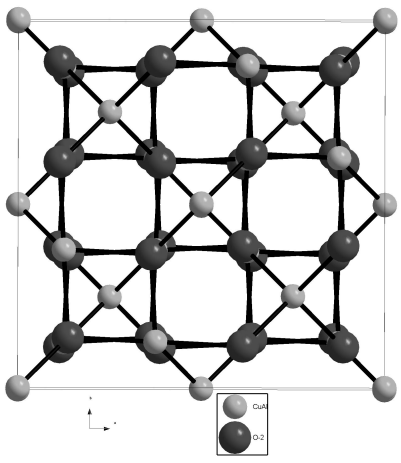

Graph.: 8-1 Crystal structure of $CuAl_2O_4$

The phase diagram of the Cu-Al-O-system[209, 210, 211, 212] is related to that of the system Cu-O[213]. The results of the investigations on Cu-Al-O are based on it. The high temperature region of the Cu-O[36, 214] phase diagram is much better investigated

than the low temperature region. Wrong informations about redox reactions of copper can influence the calculated phase diagram of Cu-Al-O.

There are experiment described in the literature with may be used for an interpretation of the engobe samples. The dissociation curves of Cu-Al-O phases of molar mixtures of 10%, 20%, 25%, 29% and 50% Al_2O_3 in CuO were determined in air. The curves for the mixtures with 10, 25 and 50% Al_2O_3, which illustrate the different features are shown in Graph. 8-2 and 8-3.

The vertical steps of these represent compositional changes associated with mono variant transitions, which will proceed at constant oxygen pressure to completion at constant temperature. Graph. 8-3 shows the isobaric ternary diagram constructed from the curves. The thin horizontal lines represent the "dissociation paths" along which the compositions of the experimental mixtures change with changes of the oxygen content. Compositions are expressed in terms of molar percentages of the components CuO, Al_2O_3 and $1/2Cu_2O$[215]. The symbols on the dissociation paths represent the compositions reached at the beginning and end of the vertical steps on the dissociation curves. The isotherms at 1130°C and 1238°C were constructed from the compositions reached at these temperatures. The compositions are $Cu_2O*Al_2O_3$, Cu_2O, and a liquid phase of composition *a* at 1130°C, and $Cu_2O*Al_2O_3$, Al_2O_3, and a liquid phase of composition *b* at 1238°C, respectively. Finally the dashed lines joining $CuO*Al_2O_3$ to $Cu_2O*Al_2O_3$ and $CuO*Al_2O_3$ to Cu_2O are tie-lines joining phases which are compatible with each other in the solid state. Of these, the former is inevitable in the

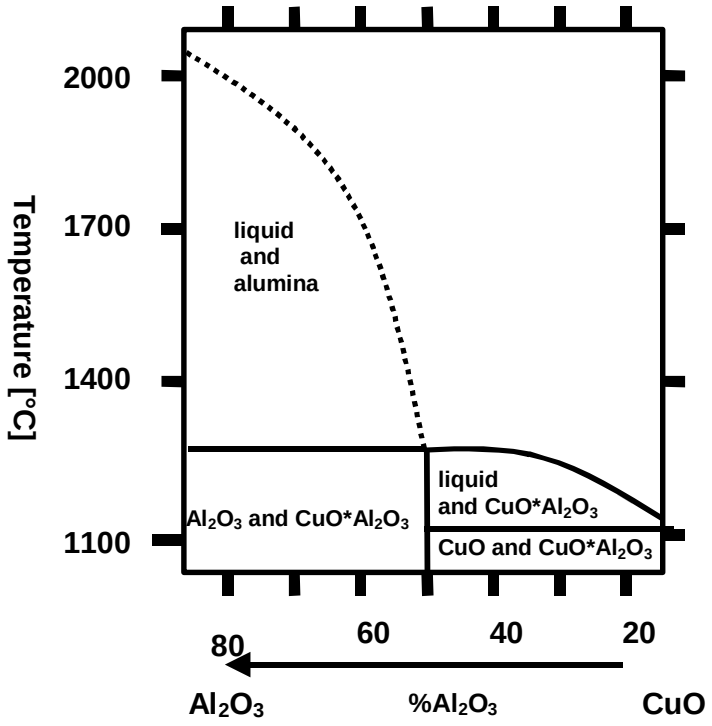

Graph.: 8-2 Phase diagram of Al_2O_3-CuO in the temperature range between 1000°C and 2000°C[209].

absence of an intermediate phase on the CuO-Cu_2O edge of the diagram. Evidence for the existence of the latter is provided by the two-stage dissociation of the CuO in the mixtures containing 10% and 25% Al_2O_3 indicated by the double step at 1026°C and 1032°C on the dissociation curves of the mixtures.

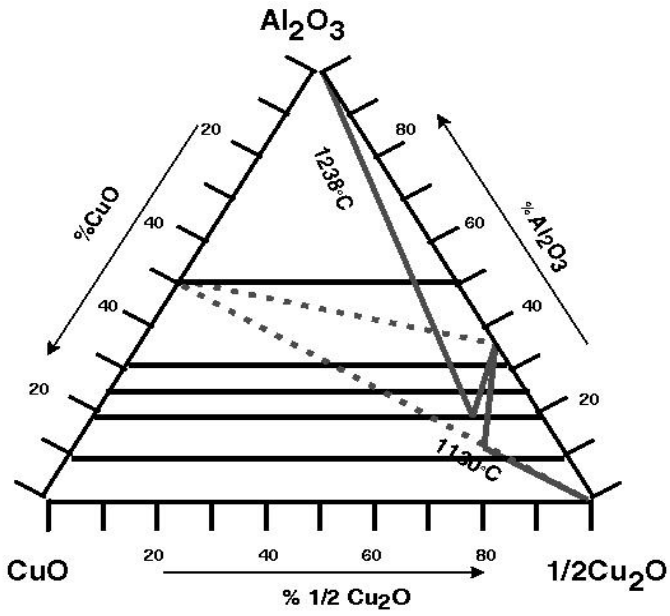

Graph.: 8-3 Phase diagram of the system Cu_2O-Al_2O_3-CuO[209].

The lower temperature is known as the dissociation temperature of CuO to Cu_2O in air[216]. The 10%-Al_2O_3 mixture consists initially of CuO and CuO*Al_2O_3 and the first step represent the dissociation of the free CuO to Cu_2O at 1026°C. The second step at 1032°C, represents the dissociation of the CuO in the CuO*Al_2O_3 in the presence of Cu_2O according to the following reaction documented in equation 1.

(56) $4CuO*Al_2O_3 + 2Cu_2O \rightarrow 4Cu_2O*Al_2O_3 + O_2$, ...

Equ.: 8-1 Dissociation step of the thermal treat met of $CuAl_2O_4$.

The reaction product is a mixture of Cu_2O* Al_2O_3 and Cu_2O. At 1130°C partial melting occurs, with a oxidation giving an eutectic liquid *a* and Cu_2O. With a further rise of temperature, progressive solution of the Cu_2O occurs with progressive loss of oxygen. The 25% Al_2O_3 mixture differs from the first one in the proportions of CuO and $Cu_2O*Al_2O_3$. Upon heating, it undergoes the same two-stage dissociation in the solid state at 1026°C and 1032°C, resulting in the same products, $Cu_2O*Al_2O_3$ and Cu_2O. Also the re-oxidation at 1130°C could be detected. In the case of the 50% Al_2O_3 mixture, the first phase initially consist only of CuO*Al_2O_3, the copper-spinel. Oxygen loss occurs at 1180°C according to the reaction documented in equation 2.

(57) $4CuO*Al_2O_3\,(s) \rightarrow 2Cu_2O*Al_2O_3\,(s) + 2Al_2O_3\,(s) + O_2(g)$, ...

Equ.: 8-2 Spinel formation reaction.

This results were partly confirmed by thermal-analysis (TG/DTA) and X-ray diffraction[207]. Experiments with CuO-γ–Al_2O_3, CuO-η–Al_2O_3 and CuO-α–Al_2O_3 showed that $CuAl_2O_4$ is not formed during the calcination only in the case of the α-Al_2O_3. One explanation of this might be the difference in the reactivity of the different alumina systems. In the case of α-Al_2O_3 the structure has to change from h.c.p. to f.c.c. due to its corundum structure, while for η–Al_2O_3 and γ–Al_2O_3 the spinel structure is retained.

One problem of the analysis of the investigated samples is the temperature behaviour of the used kaolinite system as compared to the discussed Cu/Al-oxide. In opposite to pure Al_2O_3 different mixed phases of Al-Si-O can be formed during the calcination process. Diffusion of copper ions on one side or complete oxidic phases on the other in this system makes it impossible to predetermine in which ratio the reaction partners will react and where. When kaolinite is heated, it transforms to mullite via two intermediate phases[217]. These phases are not easy to identify if they are formed by γ-Al_2O_3 (spinel type) or γ-Al_2O_3 containing Si atoms (Al-Si-spinel)[218]. At temperatures about 500°C, the kaolinite is transfomed in an endothermic reaction to metakaolinite[219]. The further decomposition at higher temperatures is characterised by two exothermic reactions at ~950°C and ~1150°C. Kaolinite is converted into metakaoline without the loss of amorphous SiO_2 at 500°. The cubic phase containing SiO_2 and Al_2O_3 is produced at the first exotherm conversion peak at 980°C an amorphous SiO_2 is liberated. The amount of this SiO_2-phase depends on the composition of the kaoline. It was suggested that this cubic phase, which has the same composition like 3:2 mullite, reoriented directly to the orthorhombic mullite structure without loss of SiO_2 at the second conversion temperature of ~1150°C, indicating that Si-O-Al linkages persist from kaolinite to metakaolinite to Al-Si-spinel and ultimately to mullite (see equations 3 to 5 in Equ. 1-3).

(58) $2(Al_2O_3{*}2SiO_2) \xrightarrow{550°C} Si_3Al_4O_{12} + 14\%\ SiO_2\ (amorphous)$
Metakaolinite Al-Si-Spinel

(59) $Si_3Al_4O_{12} \xrightarrow{950°C} 2Al_2O_3{*}2SiO_2 + SiO_2$
Transitional (1:1)Mullite

(60) $Al_2O_3{*}2SiO_2 \xrightarrow{1150°C} 2Al_2O_3{*}11/3SiO_2 + 2/3\ SiO_2$
(3:2)Mullite Cristobalite

Equ.: 8-3 Thermal transformation of kaolinite.

8.2 Experimental

8.2.1 Preparation

For the preparation of the engobe material 100g clay-powder (white, Boerkey) was mixed with 1%, 3%, 6%, 9% and 12% CuO powder (Aldrich) in a ball mill and mortar. Subsequently, the mixture was suspended with 100ml dest. H_2O and intensively stirred for 1/2h. The suspension was passed through a sieve (50 mesh) and left for one day. For calcination, the clay-copper oxide mixture was carefully stirred again and put on a handmade clay layer, dry porcelain layer (KPM) and additionally in a 5ml porcelain-vessel (KPM). After 5d, the samples were calcined in air (3K/min to 500°C, 5 K/min to the end temperature, 15 min at this temperature) at 800°C, 950°C, 1000°C, 1150°C. The samples were slowly cooled down to room temperature within two days and were carefully removed from the porcelain layer to prevent contamination by porcelain fragments. For further characterisation, the material was ground milled by hand in a mortar. The preparation based on the description by Picolpasso[184].

8.2.2 RFA, X-ray Fluorescence Analysis

To obtain a more detailed element distribution of the surface areas of the ceramic object, the X-ray fluorescence analysis was used. Small pieces of the

different regions of the original sherd were taken and placed undiluted and as a piece in the sample holder. Also a probe of the body was taken as reference. A RFA-2001 by Seiko Instruments was used for the measurements.

8.2.3 IR, infrared spectroscopy

The samples were milled by hand and pressed in KBr, potassium bromide for transmission and also for reflective spectroscopy. A Perkin Elmer 9125 equipment was used for the measurements. The low sensitivity of this method was only able to give a fingerprint of the different samples

8.2.4 XRD, Xray diffraction

A STADI P (Stoe) diffractometer equipped with a scintillation counter was used for the XRD studies with monochromatized Cu K_α-radiation in Bragg-Brentano geometry (see experimental chapter).

The samples were milled by hand in a mortar to get a homogeneous powder mixture. The problem of this procedure is that surface compositions were also destroyed by that. The geometry of the XRD equipment did not allowed a application of a complete unmilled sample. Additionally, the progress of glass formation of the probes led to an increase of an amorphous spectral underground that implied problems with the detailed peak analysis.

8.2.5 UV/Vis-spectroscopy

The samples that were milled for the XRD analysis were also used for the diffusive reflectance spectroscopy. In this case a comparison between the milled and not ground samples led to assumption that the differences due to the procedure are neglectable. Reference material was barium sulfate powder. The equipment that was used was a $\Lambda 9$ –Spectrometer (Perkin Elmer Inc.).

8.2.6 SEM/EDX

SEM images were taken with a Hitachi S-4000 SEM equipped with an EDX DX-4 (energy dipersive X-ray diffraction) (EDAX Inc.) for element identification. The problem to analyse the samples was that the sintered material showed extremely high conductivity of the ceramics surface. The bad quality of the pictures is

due to that problem. It was not possible to investigate one original sample in the SEM chamber, because this would have meant to interrupt the complete service routine of the institute.

8.3 Classification

The simple classification of a ceramic object is based on a system developed by Hennicke[220] (Table 3-1).

ceramic object → fine →porous →coloured →earthenware →majolica

Table 8-2 Hennicke system[220]

The body of the sherd (sample No. 899)[221] (Graph. 8-4) is white coloured with a Mohs value of 6 – 7 (quartz)[222]. The piece belongs to a open form like a plate or bowl (Graph. 3-2) The edge shows a fine grain structure. The porosity is below 0.2 mm mean pore size. The water up taking was not tested. The particle size of the inclusions is below 0.2 mm and consists of quartz and not identified minerals. The sherd shows nor direction structure due to its production. The colour of the sherd is Munsell Nr.: 4.00YR 8/2 with a homogeneous distribution. A formation on a throwing wheal can be supposed because of the equal thickness of the material. In this case the decoration of the sherd is most important. The piece is completely coated on both sides by different multicolour glazes. The smooth surface shows variable thickness due to the different colours and the decoration. The mean thickness is near 0.4mm. It is formed by a combination of different techniques well known for the majolica type. The painting was made by using in-glaze colours in combination with scratching of

Graph.: 8-4 Photo of majolica sherd 899.

the contours of some parts of the figure of a soldier of the 16th century armed with a sword. The person wears a brown coloured waistcoat with a white neck and a shirt with blue sleeve and brown trousers. The violet hat is decorated with a green plume. The monochrome yellow background is completed with green trees. The style of the painting is typical for the production of the manufacture in Montelupo/Fi. during the late Italian renaissance period[223] in the 16. century (colours described in Table 8-3).

area / figure	colour
background	Yellow 2.00GY 9/10
tree	Green 9.00G 5/6
arm	Blue 5.00PB 5/8
hat	Violet 4.00P 1/2
backside	White 5.00R 8/2
body	Grey 4.00YR 8/2
edge	Orange 7.00YR 4/12

Table 8-3 Colour key for 899 glazes based on Munsell system.

The complete archaeological description of the majolica fragment is given by its pottery recording sheet (Table 8-4).

Topography: Area: manufatury City: Montelupo County: Fiorentino/ Italy Piece: fragment			Form: decorated ceramic fragment			
Inv.-No.: 899			Type: Majolica			
Graphic: No	Foto: 1	Throwing wheel: X	Free formed			
Earthenware: X	Protoearthenware:		Near earthenware:	Pocelain:		
Status:	complete	Wall fragment:	Verge fragment: X	Floor fragment:		
surface	Colour: multi colour		Inside: Fig. decorated	Outside: decorated		
	Engobe.	Glaze: X	Sinter engobe:	Outside: X	Inside: X	Terra sigillata
	Structure	Smooth: X	Fine sandy:	Rough:		
		Chalky:	Rough sandy:			
	Mark by pistill: no		Lettering: no			
body	Colour: light grey					
	Structure: Porous:	fine porous: X	Smooth: X	Layered: X		
	Structure: Densly	rough porous:	Granolous:	Splinted:		
	addition: Kind: quartz sand					
	Granulate	fine (<0,2 mm)	Middle (0,2-0,63mm): X	Rough 1 (0,63-1,0mm)	Rough 2 (1,0-2,0mm)	Very rough 3 (>2,0mm)
	Round:	Edge: X	Homogeneous: X	Inhomogeneous:		
	Amount	less (<5/0,5cm^2)	Middle (5-10/0,5cm^2) X	Much (10.20/0,5cm^2)	Very much (>20/0,5cm^2)	
	Mohs: 6	Oxidised	Yes:	No: X	particularly	
Parameter	High: 2,9cm	Aperture diameter : 36cm	Max. diameter: 36cm	Floor diameter: unknown		
Remarks:						

Table 8-4 Pottery recording sheet (RLMB).

8.4 Characterisation and Discussion

8.4.1 Colour

The colour impression of the samples changes with the copper content. It changes from light grey (1%CuO, 800°C) to black (12%CuO, 1150°C) via a brown region between 850°C 10 1000°C through all concentrations (Table 8-5).

CuO[%]	colour							
1	grey 5.00YR 8/N	grey 5.00YR 8/N	grey 5.00YR 8/N	grey 5.00YR 8/N	grey pigment 10.00R 9/2	grey pigment 10.00.R 9/2	grey pigment 10.00R 9/2	grey pigment 10.00R 9/2
3	grey 5.00YR 8/N	beige 6.00YR 8/2	brown 6.00YR 7/4	brown 6.00YR 6/6	brown pigment 5.00YR 6/4	black pigment 3.00YR 6/4	black pigment 6.00YR 5/2	black pigment 3.00YR 6/4
6	grey 5.00YR 6/N	brown 7.00YR 6/4	brown 6.00YR 5/8	brown 6.00YR 3/6	brown pigment 5.00YR 2/4	black pigment 3.00YR 3/4	black 6.00YR 2/2	black 6.00YR 4/2
9	grey 5.00YR 6/N	brown 9.00YR 5/4	brown 4.00YR 5/6	brown 6.00YR 3/6	brown 5.00YR 1/2	black 3.00YR 2/N	black 3.00YR 2/N	black 3.00YR 1/N
12	grey 5.00YR 4/2	brown 9.00YR 4/2	brown 3.00YR 4/4	brown 8.00YR 2/6	black 5.00YR 1/N	black 3.00YR 1/N	black 3.00YR 1/N	black 3.00YR 1/N
T[°C]	800	850	900	950	1000	1050	1100	1150

Table 8-5 Comparison of the sample-colour (Munsell system).

Opposite to the description in the literature, the samples did not show a green colour. The sample colour can be divided in three different regions: 1. grey; 2. brown; 3. black. At 800°C, the grey colour of the sample may indicate that a reaction did not occur. At 850°C, the formation of a homogeneous brown coloured material is observed for concentrations higher 3% CuO. Between 950°C and 1000°C, a change to black occurred. At higher temperatures, a pigmentation started for concentrations of 1-6% CuO. For higher concentrations the formation of a dark-black material with a glassy character could be detected. The increase of sintering forced by temperature

and copper concentration is obvious from light-microscopy. It seems, that a reaction started in the temperature interval of 850°C to 1000°C which led to colour-changes of material. At higher temperatures, the formation of a glass phase at the engobe surface was observed parallel to the disappearance of the brown character of the samples. Together with this colour change to black the formation of black coloured pigments in a dark grey matrix happened in case of low copper concentrations. SEM/EDX of these samples showed that a highly porous material was formed with an inhomogeneous distribution of copper(oxide). The material is formed of sintered particles with no uniform characters was proven by EDX and SEM. The pore size distribution decreased parallel to the temperature as shown by BET. At temperatures above 1000°C, a SiO_2 matrix seemed to cover the particles. (Graph. (8-5 to 8-7.).

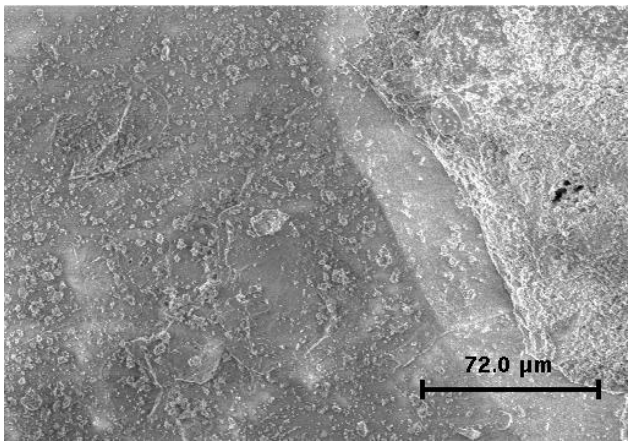

Graph.: 8-6 SEM of piece of the majolica 899 sherd surface.

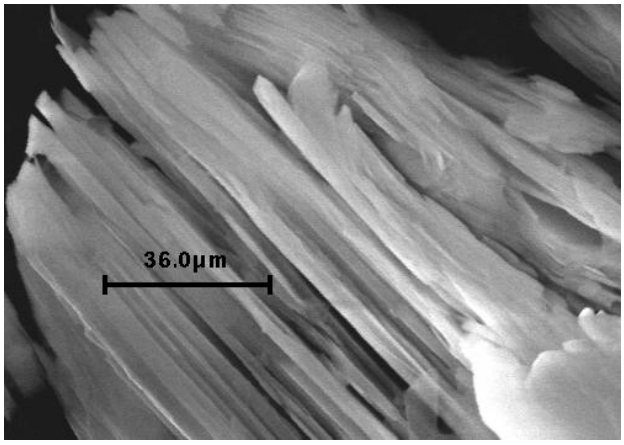

Graph.: 8-7 SEM of untreated kaolinite.

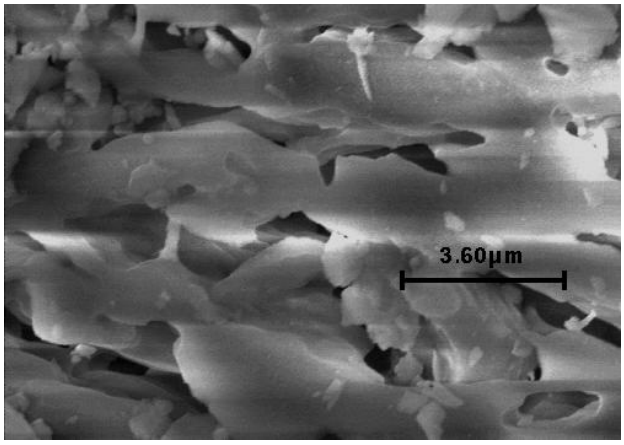

Graph.: 8-5 SEM of engobe surface of sample 113, calcined at 950°C.

8.4.2 RFA, X-ray fluorescence analysis

The results of the RFA are listed in table 8-6.

colour	Pb	Fe	Al	Si	Ca	K	Mn	Ti	Sb	Cu	Ni	Sn
body	2.196	12.220	10.092	34.513	31.883	5.177	0.643	1.025	-	-	-	-
yellow	45.379	0.721	-	46.650	-	4.739	-	-	1.145	0.122	-	-
orange	29.305	5.260	10.170	45.829	-	6.639	-	-	2.050	-	-	-
violet	10.848	1.173	12.746	41.096	27.334	6.217	0.586	-	-	-	-	-
green	17.494	2.193	11.262	40.190	24.403	-	0.287	0.868	-	2.390	-	-
blue	22.748	1.582	5.005	20.488	4.265	-	0.701	-	-	-	0.363	-
white	30.836	2.922	7.483	42.021	4.026	-	-	0.381	-	-	-	1.894

Table 8-6 Composition of body and glaze of the majolica fragment 899.

The composition of the colours can be determined by RFA. The glaze is about 1.5mm. It contains the white coloured ceramic basic layer. On that, the painting was layered with a subsequent transparent lead-glaze. This preparation followed the well known routine for majolica ceramics. For the analysis, some small pieces of nearly $2mm^2$ were carefully removed from the surface. It was not possible to separate the different layers completely. The analysis is a summary of all existing compound in the chosen region of the motive. Because of the tin-layer between sherd and painting an contamination with material of the body is deniable. It is interesting, that every colour contains alumina in different amounts. That possibly means, that the colour was prepared like an engobe with kaolinite as supporting material. As expected, the green colour was prepared with copper as colour giving metal. The orange-brown part is indicated by antimony.

8.4.3 IR, infrared spectroscopy

The detection and estimation of the high temperature phases, especially mullite, is of great importance in ceramics research. One of the main problems in detecting for mullite is due to its crystallographic rather than chemical transformation. Therefore conventional chemical analyses are of little use. XRD (X-ray powder diffractometry) can be used for its identification when mullite is present in a well-

crystallised form. IR spectroscopy does not depend on the crystallinity of the sample but only on the local co-ordination of the ions in the lattice. The IR method has the additional advantage of requiring only small amounts of samples[224].

The position and scope of the IR bands documents the state of transformation of the kaolinite (Table 8-7) or mullite matrix (Table 8-8)[225, 226, 227.] To obtain pure phases of mullite or metakaolinite (Table 8-9), the samples have to be calcined for more than 1d. Such long period, high-temperature treatment are unusual for the preparation of engobes and glazes. Thus, a mixture of several components was produced due to the short reaction times.

Si-O bond from SiO_4	$(Al^{VI}$-O)-H bond from Al[O(OH)]	Al^{VI}-O bond from Al[O(OH)]
1114 ms 1096 m 1072 s, br 1060 s, sh 1035 s 1012 s 794 m 152 m 693 m 471 s 430 m 411 mw, sh 370 mw 345 ms	938 m 914 ms 789 m	540 s 370 mw 345 ms

Table 8-7 Assignment of kaolinite band wave numbers [cm^{-1}][228] (s, strong; m, medium; w, weak; v, very; sh, shoulder; b, broad).

Si-O bond from SiO_4	Al^{VI}-O bond from AlO_4	
1260 w, sh 1203 s, sh 1152 s, sh 1071 s, br 665 w. sh 479 m 456 m, br 428 m, sh	807 m, br	

Table 8-8 Assignment of metakaolinite band wave numbers [cm^{-1}][228](s, strong; m, medium; w, weak; v, very; sh, shoulder; b, broad).

Si-O bond from SiO_4	Al^{VI}-O bond from AlO_4	Al^{VI}-O bond from AlO_6
1171 s 1120 ms,sh 960 ms, sh 927 s, sh 901 s, br 542 s, sh 500 m, sh 445 m 362 w, sh	832 s, br 740 m	613 m, sh 567 s

Table 8-9 Assignment of mullite band wave numbers [cm^{-1}][228](s, strong; m, medium; w, weak; v, very; sh, shoulder; b, broad).

The interpretation of IR spectra of compounds with spinel structure has been based since 1955 upon the theory first proposed by Walderon[229]. In this model, the crystal structure is referred to as a rhombohedral primitive cell which for a normal spinel contains two AO_4 tetrahedral consisting of four oxygen ions with a tetrahedral cation A at the centre and one B_4 tetrahedron composed of four octahedral cations. The vibrations of each of these groups are classified according to the symmetry species of the point group T_d which is also supposed to be appropriate for the vibrations of the crystal as a whole. Due to this four of the crystal modes would be IR active. Two of these are supposed to arise from the motion of the oxygen ions and two are related to the motion of the metal cations. In praxis these strong bands are accompanied by a number of weaker bands or shoulders depending on structural distortions. A large number of spectra have been obtained for a number of spinel pairs[230, 231].

The pure $CuAl_2O_4$ spinel system shows a strong band formed by two peaks at 700cm^{-1} and 610cm^{-1} completed by shoulders at 780, 520 and 470cm^{-1}[232] and a weaker band at 180cm^{-1}. In comparison to that, the IR band pure alumina unfortunately appears in nearly the same frequency regime like the one obtained for the copper spinel (Table 8-10).

ν Al-O-H	ν Al-O	δ Al-O
1085 w	625 w	370 w
1050 w	610 m, b	365 m
935 w	585 sh	350 m
915 m	540 m	322 m
890 m	510 m	295 v, w
840 m	460 w	
	415 w	
	410 w	

Table 8-10 assignments for the IR band wave numbers [cm^{-1}] of the spinel phase of Al_2O_3 heated at 1100°C[225](s, strong; m, medium; w, weak; v, very; sh, shoulder; b, broad).

The low concentrations of the pigment within the inhomogeneous matrix led to the problem of the exact determination of the copper spinel phase (Table 8-11). Transport processes forced by the low sinter temperature and influenced by the presence of copper oxide support the formation of a bulk and a surface region[233]. The bulk contains more oxidic material, while the surface is characterised by the deposition of an amorphous glassy material as proven by SEM.

1% 800°C	1% 950°C	1% 1150°C	3% 800°C	3% 950°C	3% 1150°C	6% 800°C	6% 950°C	6% 1150°C
1879w	1882w	1877w	1880w	1877w	1881w	1880w	1879w	1881w
1621vw	1620vw	-	1621vw	1620vw	-	-	-	-
1164sh	1164sh	1164sh	1164sh	1164sh	1164sh	1164sh	-	-
1078sb	1082sb	1082sb	1078sb	1079sb	1081sb	1080sb	1080sb	1083sb
797s	797s	797s	797s	797s	796s	797s	796s	795s
778s	779s	778s	778s	778s	778s	778s	778s	778s
695w	694w	694w	695w	694w	693w	694w	693w	694w
479sb	493	493sh	481sb	-	-	-	493sh	493sh
-	460sb	459sb	-	460sb	459sb	463sb	459sb	459sb

Table 8-11 IR band wave numbers [cm^{-1}] of the engobe samples (s, strong; m, medium; w, weak; v, very; sh, shoulder; b, broad)

The differences of the band shapes are very low and seem to be independent of the copper content and the calcination temperature of the samples. The detected IR bands correspond to that of mullite or alumina. IR-spectroscopy seems to be not sensitive enough for the determination of low spinel concentration. May be that one reason for that is the preparation. If the pigment formation occurred mainly at the ceramic surface due to the preparation for the analysis by milling these

surface structures were destroyed. The mixture with the spinel less-bulk decreased the concentration of the sample.

8.4.4 XRD, X-ray diffraction

The structure of $CuAl_2O_4$ as describe above leads to a characteristic X-ray diffraction pattern. However, the X-ray pattern of the samples were similar to that of mullite[234] or γ-Al_2O_3. This is not unexpected because γ-Al_2O_3 has a defect spinel structure with a close-packed oxygen lattice very similar to that of $CuAl_2O_4$. The formation of trace amounts of the Cu-spinel at the surface seems to be possible, when the intensity of the diffraction lines at d=2.8 and 2.4Å is analysed, which are strong lines for the Cu-spinel. These lines should increase with the copper content as found for the Ni^{2+}/Al_2O_3 system[235] (Graph 8-8, Table 8-12 to 8-13).

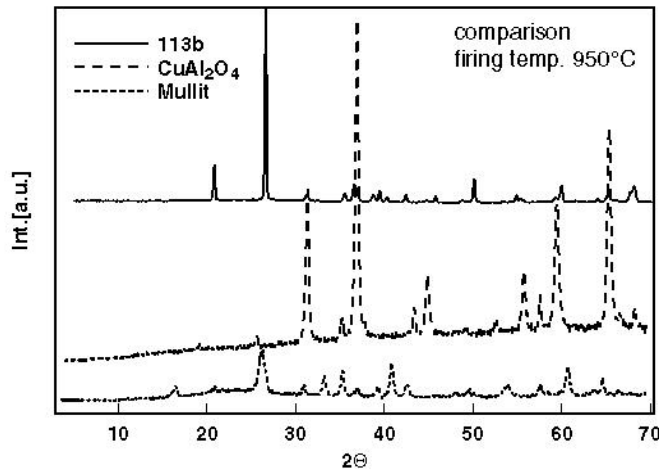

Graph.: 8-8Fig.: 8 Comparison XRD pattern of mullite, copper aluminate and engobe sample (12% Cu).

d [Å] Mullite	I/I_1	d [Å] cristobalite, high	I/I_1	d [Å] CuO	I/I_1	d [Å] $CuAl_2O_4$	I/I_1	d [Å] γ-Al_2O_3	I/I_1
5.37	7	4.110	100	2.752	8	4.66	4	4.56	40
3.758	2	2.518	12	2.531	60	2.856	55	2.80	20
3.418	9	2.149	1	2.524	100	2.436	100	2.39	80
3.383	10	2.056	4	2.311	100	2.019	16	2.28	50
2.878	7	1.782	1	1.961	3	1.649	16	1.977	100
2.686	8	1.636	7	1.867	25	1.554	25	1.520	30
2.538	9	1.455	5	1.712	7	1.428	35	1.395	100
2.414	6	1.372	2	1.581	12	1.277	3	1.140	20
2.392	1	1.261	2	1.501	16	1.231	7	1.027	10
2.289	8	1.203	3	1.418	12	1.165	3	0.989	10
2.201	9	1.188	1	1.410	14	1.080	4	0.884	10
2.196	2	1.128	2	1.379	9	1.051	8	0.806	20
2.115	8	1.088	1	1.375	14	1.010	3		
2.103	4	1.075	1	1.304	6	0.932	6		
1.967	2	1.029	1	1.266	6				
1.918	2	0.999	1	1.262	7				
1.886	5	0.953	1	1.196	2				
1.858	1	0.929	1	1.170	4				
1.839	7	0.892	1	1.161	4				
1.829	1	0.872	1	1.155	4				
1.791	3	0.841	1	1.124	2				
1.709	6	0.824	1	1.091	5				
1.698	7								
1.693	7								
1.596	8								
1.573	6								
1.562	3								
1.544	2								
1.522	9								
1.459	6								
1.439	8								
1.420	4								
1.404	5								
1.391	3								

Table 8-12 Comparison of the diffraction data of the references.

d [Å] 1%/950	I/I_1	d [Å] 3%/950	I/I_1	d [Å] 6%/950	I/I_1	d [Å] 9%/950	I/I_1	d [Å] 12%/950	I/I_1
4.500	2	5.412	2	5.446	7	5.351	2	4.677	2
4.257	17	4.255	20	4.831	7	4.790	2	4.260	19
3.577	2	3.521	2	4.260	23	4.226	19	3.524	3
3.519	2	3.341	100	4.026	7	4.006	3	3.344	100
3.343	100	3.250	3	3.717	7	3.667	3	3.249	3
3.251	2	2.875	2	3.580	7	3.581	3	2.858	5
2.454	8	2.528	2	3.517	7	3.527	3	2.751	2
2.279	7	2.455	8	3.344	100	3.324	100	2.523	5
2.235	4	2.280	7	3.249	7	3.231	3	2.452	10
2.127	5	2.235	4	2.860	7	2.946	2	2.320	5
1.979	4	2.127	6	2.703	5	2.843	4	2.280	7
1.817	13	1.979	4	2.526	5	2.741	2	2.236	4
1.670	5	1.817	13	2.454	11	2.684	2	2.127	5
1.658	3	1.670	4	2.319	4	2.514	4	2.022	2
1.540	10	1.658	3	2.281	8	2.443	9	1.980	4
1.451	3	1.540	8	2.236	5	2.316	3	1.817	13
1.381	5	1.451	3	2.128	7	2.281	5	1.670	5
1.374	8	1.381	6	2.023	3	2.237	3	1.658	3
1.288	3	1.374	9	1.980	6	2.127	5	1.540	9
1.236	4	1.287	3	1.818	14	2.021	2	1.452	3
1.228	2	1.255	3	1.686	3	1.979	4	1.429	5
1.199	4	1.228	2	1.671	5	1.817	13	1.374	9
1.833	3	1.199	4	1.658	4	1.671	5	1.288	3
1.180	3	1.182	4	1.623	3	1.658	3	1.256	4
1.153	2	1.152	2	1.541	10	1.540	10	1.229	3
1.081	3			1.452	3	1.452	3	1.200	4
1.047	2			1.429	4	1.428	4	1.183	4
1.034	2			1.381	6	1.374	9	1.153	3
1.014	2			1.375	8	1.288	3	1.052	2
				1.288	4	1.256	4	1.047	3
				1.256	4	1.229	3	1.013	3
				1.229	3	1.200	4		
				1.200	4	1.183	4		
				1.181	4	1.153	3		
				1.152	3	1.081	4		
				1.081	3	1.047	3		
				1.047	3	1.047	3		
				1.014	2	1.014	3		

Table 8-13 Comparison of the diffraction data of the engobes.

In comparison to the references, the data for the engobes documents the phase transformation of the kaolinite matrix to mullite and cristobalite but the detection of the spine is not possible. Probably the destruction of $CuAl_2O_4$ to CuO and alumina could be proved by the identification of the diffraction patterns of CuO for the samples treated at temperatures higher 1000°C.

In comparison to the references, the data for the engobes documents the phase transformation of the kaolinite matrix to mullite and cristobalite but the detection of the spine is not possible. Probably the destruction of $CuAl_2O_4$ to CuO and alumina could be proved by the identification of the diffraction patterns of CuO for the samples treated at temperatures higher 1000°C.

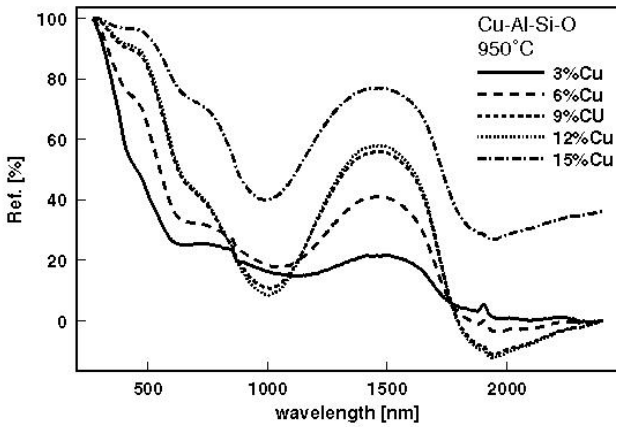

Graph.: 8-9 UV/Vis spectra of engobes with different copper content calcined at 950°C.

8.4.5 UV/Vis, diffusive reflectance

The copper containing samples show not only the two typical adsorption bands due to Cu^{2+} ions in octahedral and in tetrahedral symmetry with maxima located in the absorption regions between 1400-1600nm and 750-850nm, but also a band at 500nm. In general two bands are important for the characterisation of this system. The octahedral absorption band due to the spin allowed transition $^2E_g \rightarrow {}^2T_{2g}$, and the tetrahedral band, due to the transition $^2T \rightarrow {}^2E$. For the pure spinel the band of the octahedral absorption band is much more intensive and rather symmetric relative to that of the tetrahedral band. The extinction coefficients for tetrahedral sites is roughly 10 – 100 times that of octahedral sites so it can be deduced that about 98% of the cupric ions are located at the octahedral sites. With increasing the calcination temperature up to

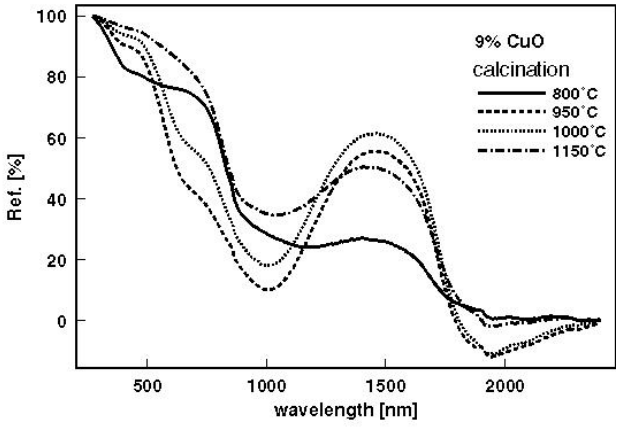

Graph.: 8-10Fig.: 10 UV/Vis spectra of engobe 113 with 9% copper content calcined at 800°C, 950°C, 1000°C, and 1150°C.

1150°C the peak shape changes to a more asymmetric signal with a lower intensity. Comparable studies interpreted this behaviour with the segregation of CuO at the surface[236] due to the decomposition of $CuAl_2O_4$[237]. This segregation can also be seen in the spectral regime of the tetrahedral signal (Graph. 8-9 to 8-12). The intensity of this signal is as high for the 1150°C sample as for the sample treated at 800°C. At 800°C nearly no reaction to $CuAl_2O_4$ could have been started and at 1150°C. At this temperature the decomposition into CuO at the surface happened parallel to its and dissolving in the cristobalite phase.

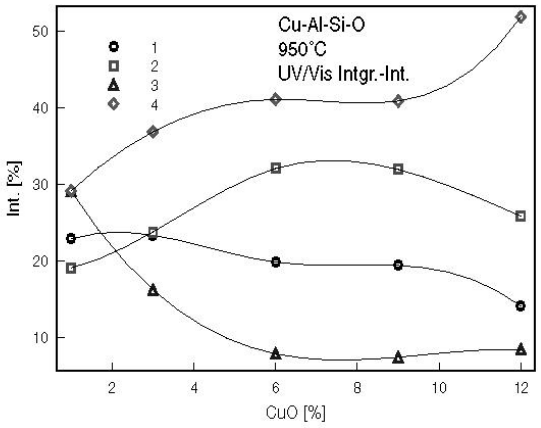

Graph.: 8-11 Comparison of the int.-intensities.

8.4.6 Temperature-programmed Reduction, TPR

The problem of understanding the firing process of the ceramic material is due to the in situ determination. It is very difficult to investigate reactions at temperatures higher than 800°C by a spectroscopic method. The measurements of the weight loss during the calcination is limited by the vessel material[238]. If the sample holder is of alumina (corund) like the sample material a reaction of both compound could not been prevented. The other possibility is to determine not the sample change but the surrounding gas

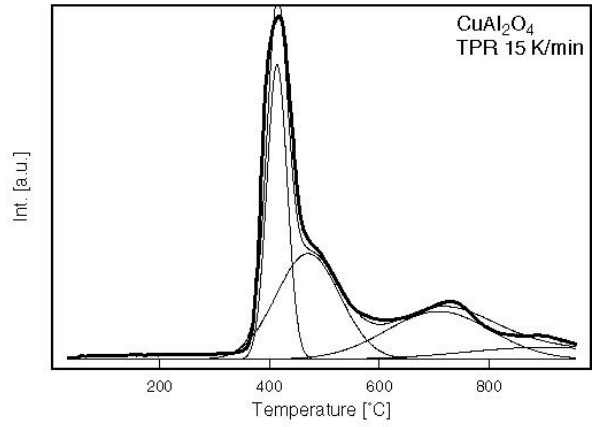

Graph.: 8-12 TPR signal of the reduction of $CuAl_2O_4$.

phase and subsequently the prepared sample by SEM or XRD.

The reduction of the material should led to the formation of the blue or green coloured $CuAlO_2$ aluminate together with a transformation of the cristobalite matrix. In the temperature range of 390°C to 900°C the reduction of the material happened, characterised by a multi-step signal. The main reduction peak appeared at 400°C followed by three more steps at 500°C , 722°C and 830°C (Graph 8-13). The re-oxidation of this material is characterised by a sequence of several small signals in the temperature range between 200°C and 800°C.

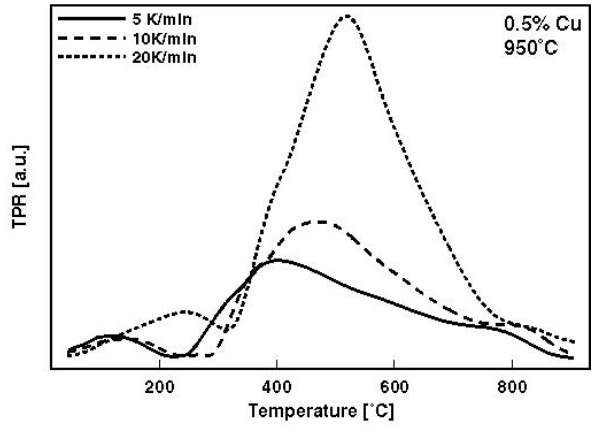

Graph.: 8-13 Comparison of heating rates of TPR curves, 0.5% Cu content engobe.

Subsequently SEM showed the segregation of copper particles to the ceramic surface (Graph 8-14). The particles have a mean diameter of 300nm. The formation of the $CuAlO_2$ was not proved. Obviously, led the inhomogeneous distribution of copper oxide in the amorphous matrix to the formation of structure copper phases on the surface. These copper is fine dispersed and should be easily reacted with subsequently added coatings during the further manufacturing of the ceramic object as described for the majolica.

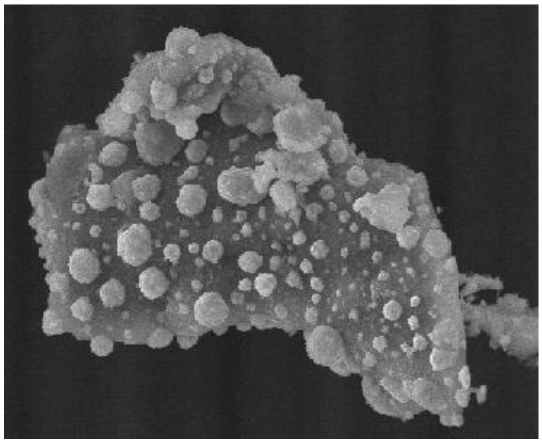

Graph.: 8-14 SEM of copper aluminate particle after TPR treatment.

The temperature dependence of this process was compared to the TPR of engobe samples (0.5% Cu and 9% Cu). The engobe behaved comparable to the pure spinel. At 380°C, a sharp signal is followed by the main reduction peak at 420°C. The profile for the low copper concentration is not as accentuated as that of

$CuAl_2O_4$. Signals with lower intensity occurred at 800°C. The profile is shifted to higher temperatures depending on the heating rate. It is interesting that the reduction is not completed at 800°C. The profile for the high copper concentration is very close to that of the spinel. It showed the same peak separation and position due to the temperature.

The model independent analysis of the reduction resulted 56.48kJ/mol, the model-dependent analysis was separated into four parts ruled by nucleation and n-th order kinetics (Table 8-14). The best fit for nucleation corresponds to the obtained SEM-data.

Model	Parameter	Value	Stand. Dev.
n-dim. Avrami-Erofeev	lgA1/s^{-1}	30.1678	0.7247
	E1 kJ/mol	356.2989	9.0378
	Dimension 1	0.1966	1.26E-02
n-th order	lgA2/s^{-1}	1.3482	5.21E-02
	E2 kJ/mol	51.5674	0.7867
	React.ord. 2	2.2748	0.1182
n-dim. Avrami-Erofeev	lgA3/s^{-1}	0.7425	3.19E-02
	E3 kJ/mol	35.2828	5.04E-03
	Dimension 3	0.9093	5.04E-03
n-th order	lgA4/s^{-1}	-2.6670	1.98E-02
	E4 kJ/mol	4.8163	0.2370
	React.ord. 4	0.3961	1.08E-02
	FollReact.1	3.17E-02	3.06E-03
	FollReact. 2	1.7033	0.3564
	FollReact. 3	-1.055	0.3367
	Correlation coeff.	0.9885	

Table 8-14 Model-dependent kinetic analysis worksheet.

8.5 Conclusion

The reaction of CuO and a kaolinitic clay was investigated in the temperature range of 800 to 1150°C. Several copper oxide concentrations were used at different calcination temperatures. The resulting ceramic material were

characterised with respect to its different colour impression due to temperature and copper content. Because of ist important properties for cataytic reaction, the system Cu-Al-O was intensively investigated for years. Knowledge on the bulk behaviour of Cu-Al-O could be extended to the behaviour of the ceramic surfaces. At temperatures above 900°C, the metakaolinite is transformed into mullite, an alumina-rich phase, and higher temperatures a complete destruction into alumina and cristobalite phases occurs. The brown colour is generated by the reaction of CuO with Al_2O_3 to $CuAl_2O_4$. This aluminate is a brown coloured pigment of the spinel type. The formation and stabilization of the blue coloured $CuAlO_2$ was not proven. The copper concentration the colour of the ceramic surfaces varies between light-brown to red-brown. At temperatures above 1000°C, the Cu-spinel is destructed parallel to the transformation of the mullite. Copper-ions possibly were dissolved in a SiO_2 matrix to form the well know green coloured character of copper glass (Graph. 8-16). Because of the low concentration of pure SiO_2 phases, the surplus copper

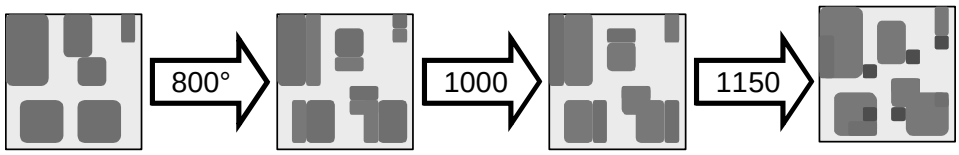

Graph.: 8-15 Model for macroscopic nucleation and transformation process due to the calcination temperature.

segregated to the surface. This segregation led to the formation of the black colour of the samples treated at higher temperatures. The presence of CuO lowers the temperature for this process and supports the segregation of SiO_2 phases to the surface.

Enhanced sintering is documented by the decreasing pore-sizes and the formation of a glassy surface as proven by SEM. The sinter process started at 800°C. So, in any case a glass phase as possible matrix for the copper is present in addition to a pigment formation. For a majolica potter, this aspect is less important. The surface of majolica is modified by a coating of transparent lead-glaze. The firing process renders possible the solution of copper with an inherent colour change (Graph 8-17). Thus, the strict separation between the both terms of engobe and glaze is insufficient. Both are co-existent in an actual sherd. Using copper as indicator system the engobe definition is due to the colour of the ceramic material. A

brown coloured coating means that the spinel formation is preferred. A green coloured sample with the same composition means that the glass formation has happened and overflows the pigment. The macroscopic rough surface character as sign for an real engobe is fulfilled however in both cases. The addition of quartz to the initial mixture allows a continuous transition between both species. This result means that the archaeologist is able to classify the firing temperature of a decorated ceramic object easily by comparing the colour of an possibly engobe. This may support the investigations at this field about comparison of sherd colours, especially if the sherd is weather-beaten or too precious for a destruction for analysis. It is expectable, that also for other well known metal oxides which were used for the

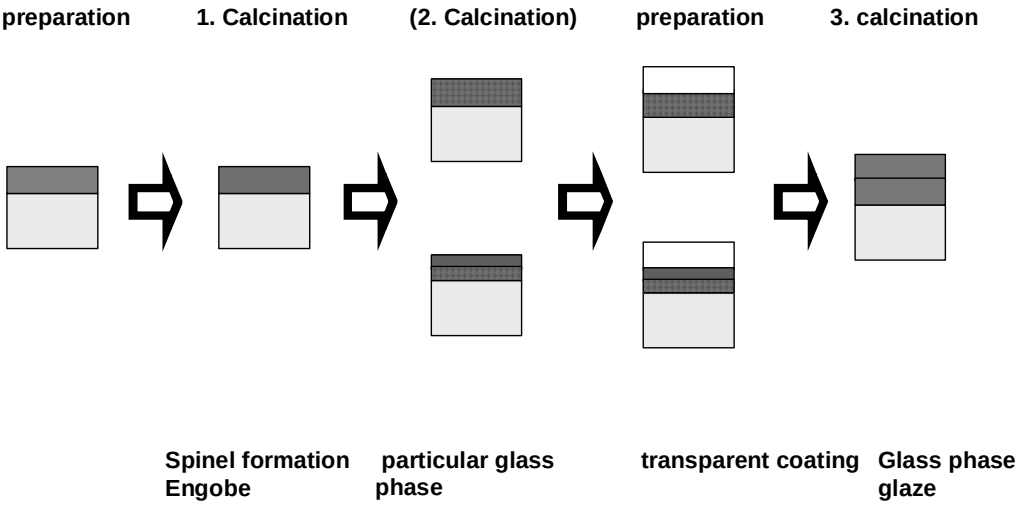

Graph.: 8-16 Model for the preparation of green coloured ceramic coatings.

preparation of colour pigments, such an concentration and temperature dependence could be obtained.

9 The structural view: Perowskite-type oxides

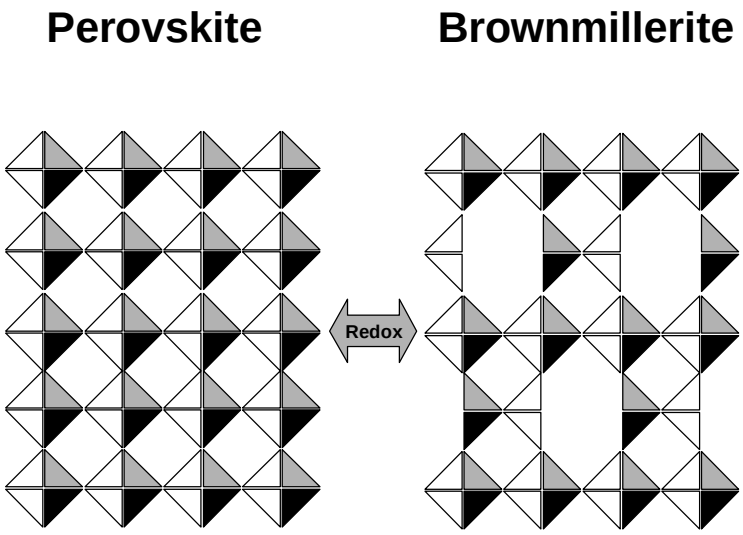

(Model for the perowskite-type oxides and the brownmillerite-type oxides redox system)

Abstract

The tested perovskite-type materials catalyse the total oxidation of the hydrocarbons in the temperature interval of 400-700°C irrespective of structure, type of transition metal or degree of oxidation. Although copper and iron oxide phases did not show different behaviour in their catalytic activity, the *post mortem* structural analysis revealed remarkable differences in their structural stability under reaction conditions.

(a) The iron oxide phases were found to be stable under catalytic conditions. The oxygen content of the used catalyst depended on the reaction atmosphere. Because of this dependence, the oxygen stoichiometry of the catalyst precursor is of importance for the catalytic action. For example, $SrFeO_3$ (Perovskite) and $SrFeO_{2.5}$ (Brownmillerite) showed the same phase composition, i.e. oxygen content, after reaction and their catalytic activity was similar. Therefore, only the cation stoichiometry seems to be a preparation parameter to define the oxidation state and the structure of the catalyst, and hence its catalytic performance.

(b) Copper perovskites, on the other hand, were destroyed during the catalytic tests. Under reductive conditions Cu was formed, under oxidative conditions CuO/Cu_2O. The oxides and (oxy)-carbonates of the other present elements were additionally detected. Therefore, the catalytic steady state activity does not arise from the type of copper perovskite but can be understood as being due to the decomposition products.

Because Fe-perovskites and Cu-perovskites exhibited similar catalytic properties and because the structural stability of these phases strongly differed, it can be concluded that a) the actual crystal structure of the starting material and b) the type of transition state metal is not important for catalysis. Furthermore it may be concluded that the investigated catalytic reactions are truly initiated at the catalyst surface, because bulk structural or compositional differences in the catalysts, or precursors, did not lead to different catalytic behaviour.

9.1 Introduction

Current interest in perovskite and perovskite-related compounds is based on a wide spectrum of their electrical properties which reaches from insulators, ionic and /or metallic conductors, p- and n-semiconductors to superconductors. This has led to a considerable attention with respect to their potential use as superconductors, electrode materials for batteries and fuel cells, for oxygen separation, and membrane catalysis processes for exhaust purification. Oxygen mobility which has a major influence on the attractive physical properties of perovskite-type oxides are of particularly interest in this respect. Some perovskite related compounds reveal a high reactivity upon topotactic oxidation at temperatures from 400°C to room temperature.

Transition metal oxides with perovskite-type structure are also increasingly investigated for activity of different catalytic reactions [239 ,240 ,241 ,242]. Studies are mainly reported in the literature on Co and Mn containing compounds. Surprisingly, structural or stoichiometric alterations during catalytic reactions are less well described. Because of the high lability of such compounds with respect to the oxygen stoichiometry, hence the oxidation state of the transition metals and their microstructure (ordered or disordered defects), it may be questionable in certain cases that oxides are the actual working catalysts.

On the other hand, the creation of new catalytic materials seem to be possible due to the high variability of the cation stoichiometries (solid solvents) and the existence of different structural modifications. On the other hand, this structural variability most probably leads to uncontrollable phase transitions during the catalytic reaction. Therefore, the focus of this study was the characterisation of stoichiometry, defect and crystal structure of different perovskite-type phases *before*, *during* and *after* the catalytic reaction in order to possibly establish a structure/redox-catalysis relationship.

The selected materials exhibit a wide area of different properties, *e. g.* microstructure, oxidation state and chemical activity (reactivity, ionic conduction). This broad variability arises from the possible variation of cation stoichiometry (isovalent or non-isovalent cation substitution) and the preparation method used. Selective total oxidation of ethene, propene and methanol were used as test reaction over ternary and quarternary Fe- and Cu-phases.

9.2 Structural background

Almost every element of the periodic table is able to crystallise in a perovskite-type lattice[243] of the general form ABX_3, with A and B being cations and X the anion. The resulting unit cell is cubic (a□3.93Å) in the distorted spacegroup PM3-m. The structure is formed by a three-dimensional lattice of edge-shared regular octahedra, whose centres are occupied by the B-cations. The bigger A-cations are placed at the dodecahedral sites between the eight octahedra. This aristo-type structure can be modified by three mechanisms to the hetto-type structure of a lower symmetry[244]. The character of the bonding, however, remains fixed. The mechanisms are:

A) distortion of the $[X_6]$-octahedra

B) displacement of the B-cations from the octahedral centre

C) co-operative filting of the $[X_6]$ octahedra along for two-, three- or fourfold rotational axes.

Two or three mechanisms may occur simultaneously. The resulting structures are either ordered or statistically or dynamically disordered. The symmetry of these perovskite-structures are cubic, tetragonal, rhombohedral and orthorhombic or triclinic varied sub-groups of Pm3-m. Such structural changes of the structure may occur as function of temperature and pressure. Especially the substitution of cations or anions with different ionic radii leads to structural differences. Even the mineral perovskite, $CaTiO_3$, is not cubic at room temperature, but $SrTiO_3$.

In the case of modifications of the A- or B-positions or both together, by exchange with differently valent cations, valence compensation occurs via vacancies in the A- and/or X-lattice. That is why many different defective perovskite-structures with variable stoichiometries can be prepared. In opposite is is as difficult to isolate a stoichiometric perovskite. In the literature the amount of A-cations in the structure is often label with A_x to underline the possible impurity. An example for that nomenclature are WO_3 or ReO_3. Here the x-value is x=0. The A-position is completely unoccupied. WO_3 and ReO_3 are defective-perovskites with the maximum content of free A-positions.

A well know example in the literature is the theoretical localisation of copper once in a square-planar oxygen environment ($NdCeCuO_4$), in a square-pyramidal surrounding ($NdCeSrCuO_4$) and in an octahedral co-ordination ($LaSrCuO_4$)

with the formal oxidation state of two, but neglecting the real oxidation state of the copper ion. In practice it is nearly impossible to synthesise a homogeneous material in large amounts. The influence of the third cation is important in this respect. This results in the formation of solid solutions of the metal cuprates with the additional metal oxides. The perovskite lattices are thus separated by layers of sodium-chloride lattices which makes the mixed oxide more complicate and inhomogeneous.

In general, copper-based oxides form easily under standard ceramic processing conditions and therefore many compounds are known. The size of the Cu^{2+} ion in oxides is such that when in combination with alkaline and rare earth ions, the perovskite family of compounds and their derivatives are accessible. One problem in the Cu-perovskite chemistry is the variable formal valence of copper from +1 to +3. This results in a variety of co-ordination polyhedra available for copper and oxygen. The various formal valencies of copper are easily accessible under straightforward temperature and oxygen partial pressure conditions. Hence, the copper oxidation state can theoretically vary between ”+2.5” and +1 at temperatures between 500°C and 1200°C and in different oxygen partial pressures.

The copper oxygen co-ordination can be linear (twofold) for Cu^{+1}, and square planar (fourfold), pyramidal (fivefold) and octahedral (sixfold) for valence states of +2 and higher. The octahedra for Cu^{+2} are Jahn-Teller distorted. This variability in possible co-ordination polyhedra increases the variety of Cu-based compounds, but also is critical for the accommodation of non-ideal oxygen stoichiometries. The co-ordination requirements of copper ions in the formal valence between 2+ and 3+, are similar enough so that oxidation/reduction may occur for a given single basic co-ordination polyhedron without structural rearrangement.

$LaCuO_3$ has a distorted structure of the basic ideal perovskite-type in which Cu-O-Cu bonds angles are not 180°[245]. For copper-based materials, it is best the perovskite structure as made ideally of alternating CuO_2 and AO layers where A represents the larger cation (s. above). The CuO_2 layers have the basic geometry of a corner shared array of square planar copper-oxygen polyhedra. Each oxygen is bound to two copper ions, to form CuO_4 units with approximately 180° Cu-O-Cu bond angles. The AO layer is also comprised of square planar co-ordination polyhedra but is completely edge shared such that each oxygen is bounded to four A atoms resulting in a AO stoichiometry. The A-O length is approximately two times the Cu-O bond length for successful stacking of the AO-CuO_2 arrays, in which the O from the

AO layer stacks directly above the Cu of the CuO_2 layer. The stacking sequence is CuO_2-AO-CuO_2-AO-.

In most of these compounds, copper prefers to be co-ordinated to less than six oxygen ions, and the smaller rare and alkaline earth ions prefer to be bound to eight or nine oxygen-ions. Thus the ideal perovskite co-ordination numbers are not generally found in copper based oxides. The compound $Ca_{0.4}Sr_{0.16}CuO_2$ is one of the simplest oxygen deficient variation of the perovskite structure, with an 1:1 A to B ratio and with one third of the oxygen ions missing in an ordered manner. The stacking sequence is CuO_2-A-CuO_2 with A being $Ca_{0.4}Sr_{0.16}$. The infinite CuO_2 planes are complete, with all oxygen atoms missing in the A layer, resulting in fourfold Cu-O co-ordination and eightfold A-O (square-prismatic) co-ordination. This defect structure variation is the basic structure for all super-conducting compounds of this kind. This structure is only stable if “impurities” of one of the metal ions are present. $CaCuO_2$ is not as stable as $SrCuO_2$ under ambient pressure conditions. The exchange of Sr for Y leads to the formation of a quasi-one-dimensional compound[246]. Compounds of this type belong to the so called spin-ladder systems [247].

The La_2CuO_4 structure is derived from that of $LaCuO_3$ by the insertion of one additional AO layer. The new stacking sequence is now (CuO_2)-(AO)-$(AO)_c$-$(CuO_2)_c$-$(AO)_c$-(AO)- . The c-labeled layers have been shifted by 1/2a +1/2b in the plane of the layer. The (AO)-$(AO)_c$ sequence is equal to that of the NaCl lattice. In La_2CuO_4, the Cu is surrounded by six oxygen atoms, as in the simple perovskite. But the large A cations are only co-ordinated by nine oxygens, as their neighbouring layers are CuO_2 and centred AO[248]. For super conduction at 20-30K, the variation of this structure is important. The so-called T*-phase is formed when A site ions are a mixture of larger rare earth metals, which prefer nine oxygen neighbours, and smaller rare earth metals, which prefer eight oxygen neighbours. The result are single layers of corner shared CuO_5-pyramids, opposite to octahedra as are found in La_2CuO_4 (T-structure). The structure that is found at the 2:1 stoichiometry for the intermediate size rare earth metals is called T’-structure.

La_2CuO_4 is the parent compound for a large family of materials based on its K_2NiF_4-structure[249]. The holes necessary for superconductivity may be introduced for instance by partial replacement of La by alkali or earth-alkali metals like Sr[250, 251, 252] or K[253]. Compounds with a formula of $La_{2-x}K_xCuO_{4-\delta}$ show a deviation of the ideal K_2NiF_4 structure. The orthorhombic-tetragonal phase transitions occurs with values of

x= 0.03-0.05. With increasing x, the c-axis value also increases due to a larger radius of K^+ to La^{3+} and the elongation of the CuO_6 octahedra. The length of the a-axis decreases with increasing x which leads to a shortening of the Cu-O bond due to the higher oxidation state of copper. The structure of the $La_{2-x}K_xCuO_{4-\delta}$ phases can be described with a tetragonal unit cell of the space group ***I***4/mmm (Z=2) as for alkali earth substituted phases. The tetragonal structure implies an alignment of the CuO_6 octahedra parallel to the c-axis as observed for undoped and slightly earth alkali doped La_2CuO_4 in the high temperature tetragonal phase.

$YBa_2Cu_3O_7$ is the most well known member of another series of compounds. The Y^{3+} and two Ba^{2+} -cations occupy the A positions in the ideal perovskite lattice. The Y^{3+} and Ba^{2+} -ions are ordered along the c-axis as Ba-Y-Ba-Y-Ba-.... Some of the oxygen atoms are missing in real compounds, so the formula represents a non-existing compound. For $YBa_2Cu_3O_{7-x}$ (O<x<1), it has been shown that copper ions are present as Cu^{2+} and Cu^{3+}. While charge equilibrium is attained by removing all oxygen atoms from the central plane containing the Y ions. Additional vacancies in the basal plane account for the different stoichiometries, according to the value of x[254, 255].

9.2.1 Oxygen content

Oxygen transport in non-stoichiometric oxides usually occurs by motion of oxygen-ion vacancies [256]. These vacancies may be created by doping or reducing a material or may be inherent to the structure [257, 258, 259, 260, 261].

In the cubic high-temperature phase of the $SrFeO_{3-\delta}$ system, defect concentrations up to δ= 0.5 can be realised experimentally, tantamount to a complete formal reduction of the Fe^{4+} ions to Fe^{3+} ions without altering the symmetry of the lattice. For low temperatures, stable phases have been observed at 3 - d=2.5, 2.68, 2.73, 2.86, 2.97 and 1.0, usually rationalised within a δ = 1/n rule, where n denotes an integer number[262]. Interestingly this compound can be reduced to a defined defective structure of the brownmillerite type[263], [264]. This reduction/oxidation can easily be managed by electro-chemical treatment. The brownmillerite structure is based on the perovskite lattice and can be represented as a sequence of octahedral (o) and tetrahedral (t) layers o-t-o-t'-o-t-o-t'...along the b-axis. In the case of a

preservation of the overall composition of $SrFeO_{2.5}$ for instance, two main types of stacking defects are possible. One is represented by the sequence o-t-o-t-o-t-o-t'-o... and the other by o-t-t-o-o-t-o-t'-o....This structure includes a high intrinsic mobility of oxygen anions. The presence of monovalent O-species with reduced charge/radius ratio were suggested originating from the unsual high valence state of the transition metal ion Fe^{4+}. It is known that some brownmillerite type compounds are oxygen ionic conductors at 800°C to 900°C[265, 266, 267, 268, 269].

This special redox behaviour implies a growth of the surface at an atomic level. The activation of molecular oxygen is supported by the vacancies of the lattice[270] (Graph. 9-1). In this case, the oxidation state directly influences the oxygen permeability and thermal expansion of the material[271]. Conductivity measurements in different atmospheres generally yield diffusivities of oxygen ion vacancies being significantly lower than those of protonic defects. It is supposed that oxygen diffuses via a vacancy mechanism[272]. Therefore, the oxygen diffusion is too low to account for the proton transport.

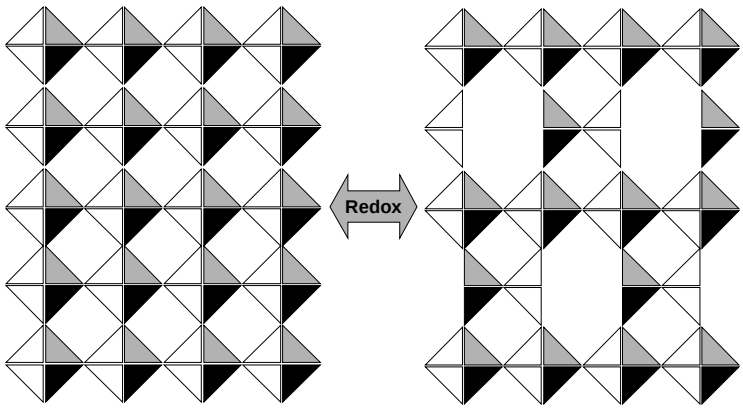

Graph.: 9-1 Perovskit-Brownmillerite redox system.

9.3 Catalytic activity

The high-T_c-superconductors have mostly been studied as catalysts for oxidation reactions[273]. Their oxygen content influences this electro-physical behaviour as well their catalytic activity[274, 275, 276]. A distinct correlation has been found between the catalytic activity and the reactivity of oxides with respect to complete oxidation and the binding energies of oxygen in their surface layer. It has

been shown by Boreskov[277] that a relationship is valid for a large series of complete oxidation reactions (Equation 9-1):

$$(61)\ E_a = E_0 +- \beta q_s ,$$

Equ.: 9-1

where E_a is the activation energy of the reaction, β is a constant, and q_s is the binding energy of oxygen in the surface layer of the catalysts.

Several publications were focussed on the determination of the oxygen content and its variation[278]. The results of these experiments lead to some assumptions:

1. High T_c-super-conductors should exhibit a moderate activity with respect to complete catalytic oxidation of organic and inorganic compounds. Because of the higher temperatures that are needed for their reduction in comparison for instance to copper-oxide, CuO, their specific activity might be lower than for the isolated metal oxide.
2. The non-conducting cuprates should exhibit a higher activity with respect to complete oxidation, due to lower binding energies of their surface oxygen.
3. Due to the more or less basic character of some perovskites, e. g. the system Y-Ba-Cu-O, they should exhibit predominantly dehydrogenation activity.

Those assumptions are extremely depending on the factors which also directly influence the catalytic reaction, like surface acidity, ionicity of the metal-oxygen-bond, structural sensitivity of the reaction, etc. Because of the temperature dependence of the perovskite structure, also changes of surface and bulk compositions should also be taken into account.

Perovskite-type oxides are used for several catalytic reactions. Especially, the system Y-Ba-Cu-O was tested for many decomposition reactions (decomposition of iso-propanol[279, 280]; dehydrogenation of methanol, decomposition of nitric oxide) and oxidation reactions (oxidation of ammonia, methanol oxidation to formaldehyde, selective oxidation of aliphatic alcohols, oxidation of ethanol to acetaldehyde, selective oxidation and amoxidation of hydrocarbons, totaloxidation[281, 282, 283].

The oxidative coupling of methane (OCM)[284, 285, 286, 287, 288, 289, 290, 291, 292, 293, 294, 295] and the DeNOx-reaction[296, 297, 298, 299, 300, 301, 302, 303, 304, 305, 306, 307] are the most discussed reaction types in the literature due to their importance for applied and environmental chemistry[308].

9.3.1 Activation of hydrocarbons

The chemisorption and reaction of hydrogen and hydrocarbon fragments on catalytically active transition metal surfaces also received great attention due to the commercial importance. Perovskite-type oxides are also active in this reaction but usually in the high temperature region above 500°C. The reason for it is the initial step of the methane activation which requires the formation of methyl radical. This activation involves oxygen species present at the surface at high temperatures. The presence of alkali as promoter seems to increase the catalytic activity[309]. A modification of this reaction is the partial oxidation of methane to syngas. CO and H_2, can be obtained as equilibrium product of the reaction between CH_4 and O_2. The catalyst should activate methane and oxygen and avoid total oxidation and coke formation. A syngas catalyst works under reducing atmospheres and high temperatures. This includes the destruction of the material and finally dispersed metal particles may react as active sites. Perovskite-type oxides are attractive catalysts for hydrocarbon combustion. The variation of the A- and the B-site mainly influences the activity of the material for this reaction. For example, it was observed that the specific activities decreased according to the variation of $LnBO_3$ (Ln: lanthanides; B: Cr, Mn, Fe, Co, Ni) for the propene oxidation, in the way $LnCoO_3$>$LnMnO_3$>$LnNiO_3$>>$LnFeO_3$~$LnCrO_3$[310, 311].

9.3.2 Methane activation

Keller and Bhasin[312] proposed a mechanism for the oxidative coupling of methane[313] on metal oxides, in which methyl radicals are formed through a surface reaction and are coupled on the surface, whereas Lunsford and co-workers[314, 315] proposed a mechanism, in which surface-generated methyl radicals were released into the gas-phase where they couple to form ethane. The existence of methyl

radicals was proven by matrix-isolation electron spin resonance (MIESR) [316]. Especially the lanthanide oxides are known for a high selectivity for the reaction to ethene[317, 318, 319, 320].The complexity of the problem of alkane activation is associated to with the low reactivity of alkanes[321].The breakage of the thermodynamically strong C-H and C-C σ-bonds in alkanes is efficient only at high temperatures in gas phase reactions (400 –1000°C)[322]. However, these processes are energy consuming and rather unselective. Methane is known to have the lowest reactivity of all alkanes. The comparing analysis of physical and chemical characteristics of hydrogen, methane, ethylene and other hydrocarbons showed that methane holds an intermediate position between hydrogen and ethylene according to its ionisation potential, proton affinity and electron affinity[310, 323, 324].

9.3.3 Propene oxidation

The high costs of propene production renders necessary the development of methods for the direct transformation of propane to acrolein, acrylic acid or acrylonitrile. Most of the possible mechanisms to obtain these oxidation products from propane as starting molecule depend on a the formation of propene as an intermediate by direct oxidative dehydrogenation (Equations 9-2)[325]. Acrolein is formed in a two steps process through the allylic alcohol intermediate. The second reaction step is more exothermic than the first one, probably due to the stabilisation energy of the conjugated electronic system of acrolein.

(62) $CH_3\text{-}CH_3\text{-}CH_3 + 1/2O_2 \rightarrow CH_2{=}CH_2\text{-}CH_3 + H_2O$

(63) $CH_2{=}CH_2\text{-}CH_3 + 1/2O_2 \rightarrow [CH_2{=}CH\text{-}CH_2OH]$

(64) $[CH_2{=}CH\text{-}CH_2OH] + 1/2O_2 \rightarrow CH_2{=}CH\text{-}CHO + H_2O$

(65) $CH_2{=}CH\text{-}CHO + 1/2O_2 \rightarrow CH_2{=}CHCOOH$

Equ.: 9-2 The main oxygenate products of the partial oxidation of propene [325].

Cu_2O is reported to exhibit significant activity and selectivity in the partial oxidation of propene to acrolein[326]. It was suggested that propene gives rise to reversibly and irreversibly adsorbed species on Cu_2O powder: the former leads to partial oxidation products whereas the latter give CO_2 and H_2O. The formation of acrolein via the π–allyl species intermediate was determined by IR-spectroscopy[327]. Investigations on poly-cristalline CuO_2 with a low surface area showed, that the formed copper rich phase during the reaction led to acrolein whereas oxygen-rich Cu_2O preferred total oxidation[328].

9.3.4 Methanol oxidation

The conversion of methanol to methyl formate is an industrially important reaction because the formate is the raw material in the production of formic acid, dimethyl formamide, acetic acid, formamide, cyanhydric acid and carbon monoxide[329]. This reaction can be conducted by direct dehydrogenation or by oxidative dehydrogenation (Equ.: 9-3). The latter preferably occurs over most catalytic materials. Copper catalysts are exceptionally active and selective for this reaction.

(66) $CH_3OH \rightarrow CH_2O + H_2$

(67) $2H_2 + O_2 \rightarrow 2H_2O$

Equ.: 9-3 Dehydrogenation of methanol[329].

Many copper-containing catalysts used in the dehydrogenation of methanol, showed significant activity losses during operation. It was suggested from comparable experiments with nickel catalysts that this deactivation is due to the formation of polymerised formaldehyde at the catalyst surface. But for well dispersed copper particles this effect could not been proven[330]. Hence the question of deactivation is still open.

9.4 Influence of hydrogen

The presence of hydrogen in the reaction mainly influences the catalyst surface. The structures of the perovskite-type cuprates are strongly temperature dependent. Changes of temperature and oxygen partial pressure support a decomposition to copper oxides and related oxides of the alkali or rare earth metals (see above). It is possible to dissolve hydrogen in perovskites at 1bar H_2 e.g. as $YBaCu_3O_7H_{0.6}$ (Equ.: 9-4)[331]. These compounds which are formed by reaction with hydrogen gas however are metastable and transform to the stable reaction products of metallic Cu and the different Ba, Sr, La, Y oxides. Thermodynamic calculations show that cuprates are reduced to metallic copper at equilibrium conditions according to the reactions. The oxygen loss corresponds to a weight loss, the solution of hydrogen to a weight gain, which can be measured by thermogravimetry[332], for instance. The weight can also increase if the formed water does not evaporate but reacts with the oxides to hydroxides or hydroxy-hydrates.

(68) $YBa_2Cu_3O_7 + H_2 \rightarrow YBa_2Cu_3O_6 + H_2O$

(69) $YBa_2Cu_3O_7 + H_2 \rightarrow 0.5Y_2BaCuO_5 + Ba(OH) + CuO + 0.5BaCuO_2 + 0.5Cu_2O$

(70) $YBa_2Cu_3O_7 + 3.5H_2 \rightarrow 0.5Cu^0 + 3.5H_2O + 2BaO + 0.5Y_2O_3$

(71) $YBa_2Cu_3O_7 + H_2 \rightarrow YBa_2Cu_3O_7H_2$

Equ.: 9-4 Possible reaction path for reduction of cuprates with hydrogen [333, 334]

The effect of hydrogen treatment on the formed structures depends strongly on the reaction conditions. Hydrogen intercalation is only possible in closed systems. At higher temperatures (>200°C), hydrogen intercalation and oxygen de-intercalation are competing processes[335].

9.5 Water interaction

Water vapour can react with $YBa_2Cu_3O_7$ thin films[336] in a topotactic mechanism at temperatures below 200°C[337]. The reaction of water appears to proceed on three different levels a) initial conversion of the outer surface, b) reaction in the grain boundary region, and c) topotactic reaction with the bulk material. The first reactions, a) and c), can be fast, irreversible, two phase processes at ambient temperature depending upon the activity of H_2O (Equations 72-74). The third process is an acid/base reaction without significant change in the transition metal oxidation state[338].

(72) $YBa_2Cu_3O_7 + x/2H_2 \rightarrow (H_2O)_{x/2}[YBa_2Cu_3O_7] = H_x[YBa_2Cu_3O_{7+x/2}]$

(73) $H_2O + O_L^{2-} \rightarrow [OH^-] + OH^-$

(74) $YBa_2Cu_3O_7 + x/2H_2O \rightarrow H_x[YBa_2Cu_3O_7] + x/4O_2$

Equ.: 9-5 Reaction of cuprates with water [337]

The intercalation of water is possible via lattice channels along the b-axis. This reaction is described as an acid/base process with reversible proton transfer equilibria between H_2O and lattice matrix oxygen anions O_L^{2-}. Because of the unsually high oxidation state of copper in $YBa_2Cu_3O_7$ at higher oxygen stoichiometry, water can principally also be involved in a topotactic redox process via the oxidation of H_2O to molecular oxygen at the outer surface and simultaneous electron/proton transfer with the formation of a hydrogen bronze.

9.6 Preparation

The preparation of these compounds is rather complex. Many different methods are documented. Depending on the properties of the material, sol-gel-processes or ceramic methods at high temperatures are applied (Table 9-1). Subsequent to such routes a subsequent purification of the product is not possible.

reaction	method	
	physical	chemical
solid-solid liquid-solid	- dry evaporation explosion spray-drying freeze-drying	ceramic crystallisation co-precipitation single compounds mixtures complexation

Table 9-1 Preparation methods for perovskite-type oxides [341]

Homogeneous perovskites with high surface areas are only obtained by those procedures which require enhanced specialised equipment. The chemical liquid-solid methods yield lower surface areas but require much simpler laboratory equipment. By close control of the reaction conditions, values of about $40 m^2/g$ for BET (Brunauer-Emmet-Teller) surface could be obtained. The methods based on solid-solid reactions are quite simple, but the very low surface area values and the lack of chemical homogeneity render these procedures inadequate for the preparation of pure perovskites. The ceramic method has to be restricted to perovskite-type oxides whose textural characteristics are not important for their use. Even in this case, care should be taken to check the purity and degree of homogeneity of the samples[339, 340, 341]. An additional electro-chemical treatment is necessary to obtain a well defined oxygen stoichiometry of the perovskite[342].

9.6.1 Investigations on the brownmillerite/perovskite-type oxide system

The cubic $SrFeO_{3-\delta}$ system can be understood as the defined, defective structure of the brownmillerite type[266]. Reduction/oxidation of this oxide can easily be managed by electro-chemical treatment. This structure allows a high intrinsic mobility of oxygen anions. This peculiar redox behaviour implies the change of the internal surface at the atomic level due to the formation of channels. The presence of monovalent O-species with reduced charge/radius ratio was suggested originating from the unusually high valence state of the transition metal ion, Fe^{IV}, in this oxide.

The initial intention of this study was to prepare a series of brownmillerite/perovskite-type oxide catalysts by cation variation with improved redox and hence improved catalytic properties. This goal could not be achieved. SEM/EDX analysis of the samples after the final preparation step, i.e. the electrochemical treatment, proved inhomogeneous starting materials (Table 9-2, Graph. 9-2, 9-3). The stepwise variation of the cation ratios from $Ca_{0.1}Sr_{0.9}FeO_x$ to $Ca_{0.9}Sr_{0.1}FeO_x$ led in all cases to inhomogeneous mixtures of different phases with Ca, Sr, and Fe stoichiometries far away from the desired compositions. Especially, wide stoichiometry ranges of the Ca to Sr ratios were found. Therefore, the oxidation state of Fe and hence the oxygen content could not be determined from the Ca, Sr, and Fe ratios.

Prepared: $Ca_{0.7}Sr_{0.3}FeO_x$	EDX	Ca	Sr	Fe	Morphology	Calculated
A%	30kV	**15.70**	**5.87**	**22.74**	Grain	$Ca_{0.7}Sr_{0.3}FeO_x$
A%	30kV	**15.09**	**7.14**	**22.22**	Grain	$Ca_{0.7}Sr_{0.3}FeO_x$
A%	30kV	**15.24**	**4.85**	**23.93**	Grain	$Ca_{0.8}Sr_{0.2}FeO_x$
A%	15kV	**15.20**	**6.12**	**22.94**	Surface	$Ca_{0.8}Sr_{0.2}FeO_x$
A%	15kV	**15.52**	**6.26**	**22.58**	Grain	$Ca_{0.7}Sr_{0.3}FeO_x$
A%	15kV	**17.34**	**9.79**	**18.30**	Needle	$Ca_{0.6}Sr_{0.4}FeO_x$

Table 9-2 EDX data of the starting material: $Ca_{0.7}Sr_{0.3}FeO_x$.

Accordingly, $Ca_{0.7}Sr_{0.3}FeO_x$ and $Ca_{0.3}Sr_{0.7}FeO_x$ showed different types of particle morphologies. The sintered surface of bigger aggregates was coated by needle-like crystallites and spherical particles. The needle-like material contained only trace amounts of calcium. The spherical grains, on the other hand, were characterised by calcium contents higher than the formal

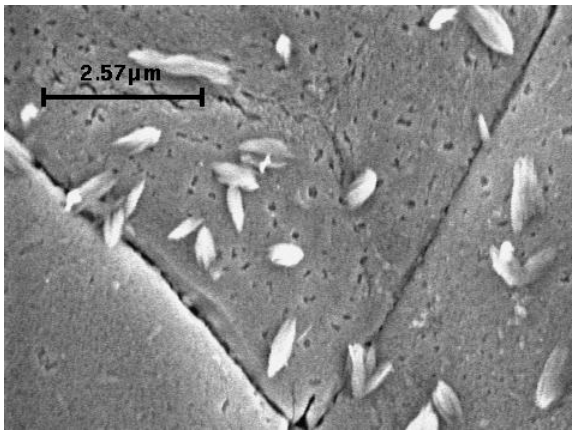

Graph.: 9-2 SEM of $Ca_{0.3}Sr_{0.7}FeO_x$ surface.

stoichiometry.

This inhomogeneity of the perovskite-type oxides renders an exact definition of the catalytically active material impossible, which is mandatory when attempting structure-activity-relations. These resulting inhomogeneous materials after such enhanced preparation techniques underlines the problem of a precise stoichiometric definition of perovskite-type oxide catalysts.

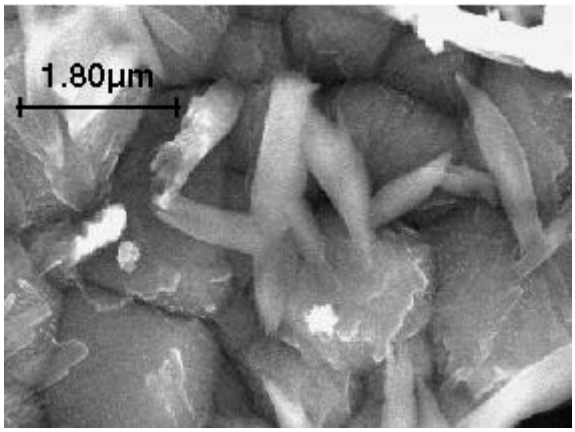

Graph.: 9-3 SEM of $Ca_{0.7}Sr_{0.3}FeO_x$ surface.

Ethene oxidation began at 420°C over $Ca_{0.5}Sr_{0.5}FeO_x$, (figures not shown). Maximum conversions of 100% ethene and 90% oxygen were reached at 510°C. Only 15% ethene conversion was obtained at the lower temperature of 490°C indicating the sharp light-off over this material. Total oxidation was the preferred reaction at this temperature. Interestingly, partial combustion to CO and methane formation was detected at still higher temperatures above 510°C. $Ca_{0.7}Sr_{0.3}FeO_x$ showed similar catalytic behaviour in this temperature range. Total oxidation took place at 510°C followed by combustion to CO and methane formation at higher temperatures.

$SrFeO_x$ was tested as the reference oxide for these compounds (data not shown). Total oxidation was determined over $SrFeO_x$ at temperatures above 500°C followed by combustion to CO and methane formation at higher temperatures. The comparison with the perovskite-type oxides clearly revealed that the altered Fe oxidation state in the perovskite-type material due to the Ca addition did not affect at all the catalytic properties.

XRD of the Ca-Sr-FeO_x materials prior to and subsequent to catalysis revealed their stability under these conditions. These perovskite-type oxides were not destroyed during the reaction opposite to the copper containing perovskite-type oxides (data not shown).

Hence, it must be concluded from the catalytic tests combined with the structural investigations that improved partial oxidation properties for alkene and methanol oxidation could not be induced by the variation of the Fe oxidation state and the supposedly easy oxygen activation via diffusion through the crystal lattice.

9.6.2 Investigation of the Cu perovskite-type oxides

The systems La-K-Cu-O and Y-Ba-Cu-O were tested for the ethane, and propene oxidation reactions. Copper oxide powder, Cu_2O, Lanthanum hydroxide, and lanthanum potassium carbonate were used as reference materials.

Total oxidation was found for all tested materials and both oxidation reactions in the temperature rage between 250°C and 600°C. 100% alkene conversion was reached for all tested materials at temperatures above 500°C. The activity toward ethene conversion followed the series Cu_2O < CuO < La-K-Cu-O > LaOH < La-K-C-O < Y-Ba-Cu-O_6 < Y-Ba-Cu-O_7.

The reaction over copper oxide started close to 250°C (data not shown). Maximum conversion was found between 370 and 420°C. The main product was carbon dioxide with a selectivity of 100%. A conversion hysteresis indicated the irreversible degradation of the material. Partial oxidation products were also not detected for the lanthanum hydroxide and lanthanum carbonate references (data not shown). The reaction started at temperatures between 350°C and 400°C, e.g. higher as compared to copper oxide. The selectivity to carbon dioxide was also 100% at an ethene conversion of 15%. Conversion hystereses again confirmed the irreversible degradation of the material.

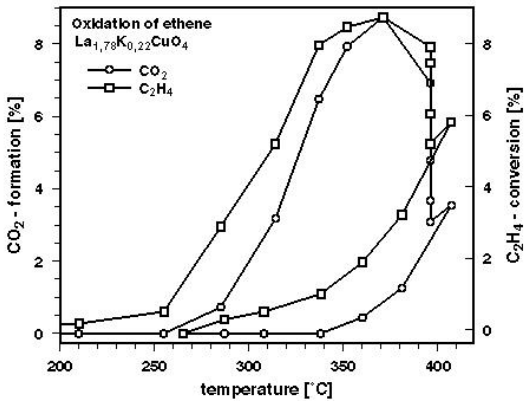

Graph.: 9-4 Oxiation of ethane. $La_{1,78}K_{0,22}CuO_4$

Subsequent X-ray diffraction of the reference samples (data not shown) showed the oxidation of the

Cu_2O powder to CuO, and the oxidation of the copper particles to copper(I)- and mainly copper(II)-oxide. $La(OH)_3$ decomposed to La_2O_3.

The lanthanum cuprate, La_2CuO_4, showed low catalytic activity at 390°C for ethane oxidation. 100% selectivity to carbon dioxide was found at the very low conversion of 2% ethene. The compound was not stable under catalytic conditions as shown by the conversion hysteresis. Ethene oxidation began at about 250°C over $La_{1.78}K_{0.22}CuO_4$ close to the temperature found for the copper oxide reference. A maximum conversion of only 7% ethene was reached at 370°C. The main product again was again carbon dioxide. The observed hysteresis of the reaction rates also suggests the destruction of the oxide. X-ray diffraction proved that the structure of the initial compound was not preserved. Copper particles, copper oxides, lanthanum oxide and carbonates were formed (Graph. 9-4, 9-5, 9-6).

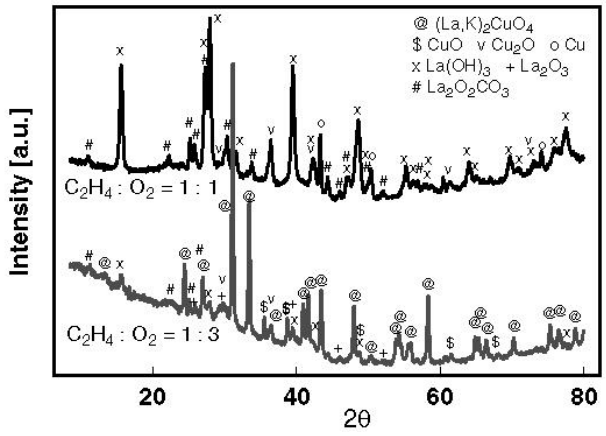

Graph.: 9-5 XRD of $La_{1.78}K_{0.22}CuO_4$ after catalytic action.

The reference measurements have shown that copper or copper oxide was the main catalytic active compound of the matrix because of there comparable behaviour in the same temperature range. Accordingly, it can be assumed that alterations of the surface region additionally to the main changes of the bulk structure led to the change of the catalytic activity.

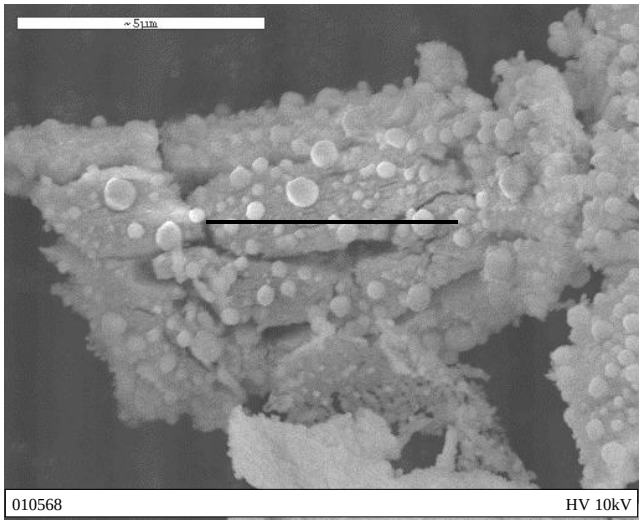

Graph.: 9-6 SEM of $La_{1.78}K_{0.22}CuO_4$.subsequent to etnen oxidation reaction treatment.

$YBa_2Cu_3O_7$ also showed only a very low ethene conversion of 4% with 100% selectivity to carbon dioxide (data not shown). The catalytic reaction started at 390°C and again showed a hysteresis of the conversion rates indicating sample destruction. $YBa_2Cu_3O_{6.5}$ was oxidized for 12h to obtain a fresh $YBa_2Cu_3O_7$ material. This in situ obtained $YBa_2Cu_3O_7$ already showed catalytic activity at 300°C (data not shown). However, conversion and selectivity levels were not improved. The addition of steam to the feed during the reaction at the temperature of highest conversion affected the oxygen conversion, which was slightly increased during water addition. The hysteresis observed for both catalyst materials, however, documented catalyst activation during catalysis.

Subsequent XRD and SEM/EDX proved the destruction of the perovskite oxides (Graph.: 9-5, 9-6). Again the formation of copper rich phases was proven at the perovskite oxide surfaces. These observations emphasise that the segregation of copper-rich phases to the surface is related to the development of catalytic activity. Hence, it may be suggested that the kinetics of this phase destruction, on one side, and phase segregation on the other by nucleation-diffusion mechanisms govern the development of the catalytic behaviour.

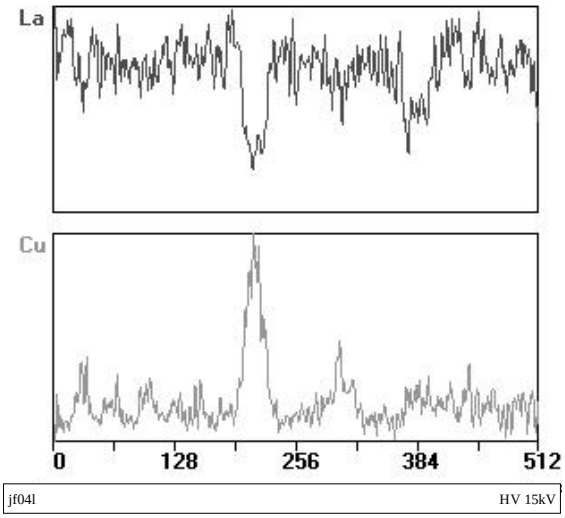

Graph.: 9-7 EDX to SEM of $La_{1.78}K_{0.22}CuO_4$.subsequent to ethene oxidation reaction treatment (see Graph.: 9-5)

3. 3. Kinetic investigation on the reduction of lanthanum cuprates

TPR was used to determine the redox behaviour of the lanthanum cuprates. The reduction of the materials showed a single TPR profile at 350°C. The reduction temperature and the occurrence of a single peak suggests that copper is situated in one Cu^{II} co-ordination in the latticed[343]. The kinetic analysis of the TPR peaks supported the results obtained from the catalytic tests and SEM. Appropriate

modelling of the TPR trace could only be achieved by the nucleation-diffusion, Avrami-Erofeev kinetics[344] which gave an activation energy of 65 kJ/mol for the reduction (Table 4). Model-independent TPR analysis yielded a comparable value of 62 kJ/mol. A comparably low activation energy of 42 kJ/mol was found for the known nucleation controlled reduction of Cu_2O. The assumption of a diffusion controlled TPR process using the Jander equation, on the other hand, gave an activation energy of 200kJ/mol which is much too high for diffusion-limited reactions and therefore can be rejected. Therefore, it can be concluded that the reduction of the perovskite-type cuprates occurs via a nucleation-controlled mechanism. It suggested that this nucleation and segregation of copper phases at the surface of the perovskite-type oxides is the underlying mechanism which is responsible for the catalytic activity of these cuprates. The perovskite-type cuprates themselves are catalytically inactive.

4. Conclusions

All tested perovskite-type oxides catalysed the total oxidation of the hydrocarbons in the temperature interval of 400-700°C irrespective of their initial structure, composition, type of transition metal ions, or degrees of oxidation. Although copper and iron containing perovskite-type oxides did not show different behaviour in their catalytic activity, the *post mortem* structural analysis revealed differences in their structural stability under reaction conditions.

(a) The iron oxide phases were found to be stable under catalytic conditions. The oxygen content of the used catalyst was found to depend on the reaction atmosphere. Because of this variability, the oxygen stoichiometry of the initial perovskite-type oxide is not of importance for the catalytic action. For example, $SrFeO_3$ (perovskite) and $SrFeO_{2.5}$ (brownmillerite) showed the same phase composition after reaction and accordingly their catalytic activity was similar. Therefore, the non-transition metal cation stoichiometry seems to be the only parameter to define the oxidation state and the structure of the catalyst, and maybe its catalytic performance.

(b)Copper perovskites were destroyed in all catalytic tests. Under reductive conditions Cu was formed, under oxidative conditions CuO/Cu_2O. The oxides and

(oxy)-carbonates of the other elements present were additionally detected. Therefore, the catalytic steady state activity does not arise from the initial type of copper perovskite. It may be understood as the sum of the activities of all decomposition products.

In the case of the copper containing samples the nucleation process seemed to rule the catalytic properties. The interpretation of the reduction kinetics by the application of Avrami-Erofeevs model. The mechanism of the destruction led to the formation of copper rich phases or copper particles. This may led to the assumption that this copper phases are responsible for the catalytic behaviour.

Because Fe-perovskites and Cu-perovskites exhibited comparable catalytic properties and because the structural stability of these phases strongly differed, it can further be concluded that

a) the actual crystal structure and

b) b) the type of transition state metal is not important for the tested reactions.

Moreover, it may be concluded that the tested catalytic reactions are truly initiated at the catalyst surface, because bulk structural or compositional differences in the catalysts, or precursors, did not lead to different catalytic behaviour.

10 The combinatorial view: Ag2Cu2O3

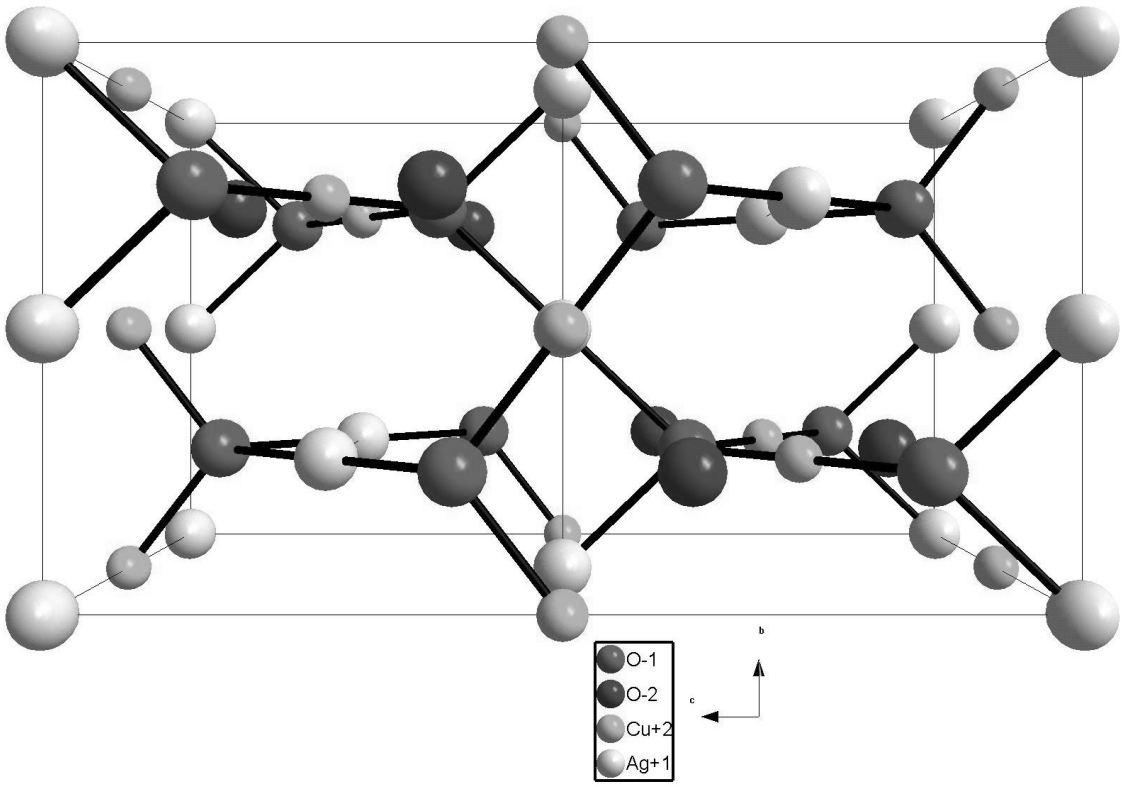

(Structure model of $Ag_2Cu_2O_3$.)

Abstract

$Ag_2Cu_2O_3$ is the first silver cuprate synthesised at comfortable conditions. The presented investigations are based on the presumption that this compound possibly combines the catalytic activity of both metals either in the perovskite-type oxide or by alloy formation. The catalytic activity of the silver cuprate was studied in model high- and low-temperature reactions, *e.g.* oxidative coupling of methane, oxidative dehydrogenation of ethane, and methanol oxidation. The physicochemical properties of this compound were examined by thermoanalytic techniques and temperature-programmed oxidation and reduction combined with photoelectron spectroscopy. Scanning electron microscopy, transmission electron microscopy and X-ray-diffraction were additionally used. Only minor catalytic activities were observed for the high temperature test reactions. Hystereses of conversion versus temperature of all reactants described irreversible catalyst degradation. It exhibited the catalytic properties of Cu or Ag metal depending on the reaction conditions. At low temperatures, however, this material showed reversible methanol partial oxidation properties. At temperatures higher 175°C, complete conversion of H_3COH to formaldehyde and CO_2 could be detected.

10.1 Introduction

The redox behaviour of copper is often discussed in the literature[56,345, 346, 347, 348, 349] which is based on its importance for heterogeneous catalytic reactions. Copper catalysts are used for many different industrial processes like the glycol oxidation to glyoxal (Cu)[350], or the methanol synthesis (Cu/Al-Zn-O)[5, 351].

Despite the industrial application, the fundamental reactions underlying the catalytic processes are less understood, being exemplified by the current phase diagram of the system copper-oxygen, which is based on measurements in the years before 1929[36].Thus, the phase transition of CuO and Cu_2O is described as a sharp phase boundary at 320°C, or alternatively as a very fast, one-step process being not resolved yet. The existence of copper sub-oxides at this phase boundary is neglected.

A large number of publications deals with the catalytic behaviour of copper up to 1000°C. Different model systems/reactions were used far from industrial catalysts or catalytic reaction conditions[33, 49, 53, 352, 353, 354, 355]. Copper sub-oxides were one suggested explanation for the catalytic activity of copper, although, never being detected[356]. Recently, the active copper species was suggested to be oxygen dissolved in copper metal having interesting properties[79, 357].

The oxidation states $Cu^{[I]}$ and $Cu^{[II]}$, are most common in copper chemistry, but there are other stable states like $Cu^{[III]}$ and $Cu^{[IV]}$. The oxidation state of the active metal during the catalytic reaction is one aspect of catalytic activity. Variable redox systems, like copper, may experience morphological[358], and electronic changes forced by the catalytic reaction[359].

A possible way to obtain information about such alterations is the molecular tailoring of starting materials containing metal ions in well-defined oxidation states, and the characterisation of the catalyst by high end in situ techniques combined with calculations of possible surface species, if possible. $Ag_2Cu_2O_3$ renders possible the investigation of two well-known, active metal ions, Ag and Cu in one compound with special structural properties[360, 361]. Thus, the activation of molecular oxygen on $Ag_2Cu_2O_3$ may occur differently than over Ag and Cu catalysts.

For silver catalysts, a model could be developed that describes the influence of the surface on the catalytic activity during partial oxidation reactions like the oxidative coupling of methane or the oxidation of methanol. Three different

oxygen species were detected by XPS/UPS and TDS experiments at relevant temperatures[362]. Chemisorbed surface oxygen, O_α, was suggested to be responsible for total oxidation. Bulk-dissolved oxygen, O_β, may diffuse through the lattice at elevated temperatures and may react with dissolved hydrogen, the reaction enthalpy leading to pore formation. The third species, O_γ, was assumed to be responsible for the catalytic partial oxidation. It is localised in silver (111) surfaces, which are formed during reaction by faceting[363]. This Ag-model can also be transferred to the catalytic behaviour of copper catalysts during partial oxidation reactions[364].

The structures of the copper oxides are well known and only summarised here for further argumentation. CuO is described by the tenorite lattice in which Cu is in a quadratic planar oxygen co-ordination and O is tetrahedrally co-ordinated by Cu with copper-oxygen distances of 1.94Å[365]. Cu_2O, the cuprite lattice-type oxide, also shows tetrahedrally co-ordinated oxygen and is an example for linear co-ordinated copper, i.e. the anti-cristobalite structure type, with copper-oxygen distances of 1.84Å[366]. The corresponding silver oxide, Ag_2O, also crystallises in this lattice type[367]. In contrast, the silver oxide, AgO, is a compound constructed by units of $Ag^{[I]}$ and $Ag^{[III]}$ ions with linearly co-ordinated $Ag^{[I]}$ and quadratic planarly co-ordinated $Ag^{[III]}$. These basic structural rules led to the presumption that the metal oxidation state defines its co-ordination.

For example, perovskite-type oxides accommodate different ionic radii, i.e. oxidation states[368 369]. In ($NdCeCuO_4$), Cu is in a square-planar oxygen environment, in $NdCeSrCuO_4$, it is in a square-pyramidal surrounding, and in $LaSrCuO_4$, it is in an octahedral co-ordination with the formal Cu oxidation state of plus two[370, 371].

This broad structural chemistry with variable co-ordination spheres of copper and oxygen is motivation for the development of new compounds with new properties. The successful synthesis of $Ag_2Cu_2O_3$[360], may provide the link between the catalytic activity of copper and silver, their oxides, and perovskite-type oxides due to its structural and morphological properties and its redox-behaviour. $Ag_2Cu_2O_3$ could combine the Ag and Cu properties and may have increased catalytic activity [33, 362].

10.2 Experimental

$Ag_2Cu_2O_3$ was prepared by the group of Dr. P. Gomez-Romero[360]. The catalytic experiments were performed in a tubular quartz reactor (length: 15cm, diameter: 4mm). The silver cuprate was placed in the isothermal zone of the reactor by quartz wool plugs. A nickel-chromium-nickel thermocouple was contacted outside reactor walls. An evaporator (Peco Inc.) was used for the methanol reaction mixtures. The methanol to oxygen ratios were varied between 3:1 to 0.5:1 using constant flow rates of 30ml/min in 100ml/min helium. Helium was used as inert diluent. Product analysis was done by on-line GC (Varian Star 3400, (Varian Inc.) equipped with a Carboxen 1000 GC column. The catalyst was quenched down to room temperature by pressured air in flowing helium or in the reaction atmosphere.

It was characterised by transmission electron microscopy (TEM), scanning electron microscopy (SEM), X-ray photoelectron spectroscopy (XPS), ultraviolet photoelectron spectroscopy (UPS), X-ray diffraction (XRD). SEM and TEM were applied at different stages of the reactions. SEM images were taken with a Hitachi S-4000 SEM equipped with electron dispersive X-ray analysis (EDX) for element identification. For TEM an CM 200 (Philips Inc.), 200kV, was used. The TPR (temperature-programmed reduction) experiments were performed with a TPDRO 1100, (CE Instruments Inc.) using a mixture of 5% hydrogen in argon (Linde Inc.), a flow rate rate of 50ml/min, and heating rates of 5 to 20 °C/min.

For XPS analysis, done with a modified Leybold Heraeus spectrometer LHS 12 MCD, the samples were first heated in a special preparation cell attached to the XPS chamber at different temperatures (80°C, 125°C, 225°C, 250°C) in 1 bar 5% hydrogen in argon with a heating rate of 10K/min. The sample was then subjected to XPS and UPS. Non-monochromatised Mg K_α (1253.6 eV) radiation was used as excitation source for XPS. A fixed analyser pass energy of 108 eV was used corresponding to an instrumental resolution of 1.0eV. The binding energy was calibrated using Au $4f_{7/2}$ (BE:84.0 eV). Surface compositions were calculated after subtraction of a Shirley-type background using the instrumental sensitivity factors. For UPS, HeI ($h\nu$: 21.2eV) and HeII ($h\nu$: 40.8eV) radiation was used with analyser pass energy of 12 and 24eV. After the each reduction step, the sample was re-oxidised in 5% oxygen in helium at identical reaction temperatures, and accordingly analysed.

A STADI P (Stoe Inc.) diffractometer equipped with a scintillation counter was used for the XRD (X-ray diffraction) studies with monochromatised Cu K_α-radiation in Bragg-Brentano geometry (see chapter 7).

10.3 Results and Discussion

10.3.1 Catalytic test and SEM-EDX characterisation

Several test reactions were used to investigate the catalytic properties of $Ag_2Cu_2O_3$. The ethane oxidation by NO / NO reduction ($DENO_x$), oxidative coupling of methane (OCM) were used as high temperature test reactions. Dehydrogenation of ethane (OCE) and the methanol oxidation (MOX) were applied as low temperature test reactions.

10.3.2 High temperature reactions

10.3.2.1 OCM, oxidative coupling of methane

Since the work of Keller and Bhasin[312] , the oxidative coupling of methane (OCM) has received attention. C-H bond breakage is the rate limiting step in OCM[372]. Temperatures are usually applied higher than 900K. Catalysts studied in OCM are often related to perovskite-type oxides, e.g. the system La-Sr-Co-Fe-O or La_2O_3[373]. Because of the structural relation of $Ag_2Cu_2O_3$ to perovskites on one side and because of the activity of silver for OCM, $Ag_2Cu_2O_3$ was tried as catalyst or catalyst precursor in this test reaction.

An extremely low methane conversion to carbon dioxide of ~1% was observed at 200°C. The conversion ceased again with increasing temperature. Hence, this first regime of conversion is not catalytic but due to a stoichiometric reaction with the parent oxide. A second regime of activity had its maximum at 600°C. At this high temperature, the methane conversion to carbon dioxide and that of oxygen was 20%. The main reaction product, however, was carbon dioxide. Oxidative coupling to ethylene could not be detected (data not shown).

Subsequent SEM, however, revealed spherical copper particles partly covered by a silver copper alloy after the catalytic test with facetted surfaces and the

formation of amorphous carbon material. Ag was nearly complete separated from Cu and sublimed to the reactor tube and to the quartz wool plugs (Graph.: 10-1, 10-2).

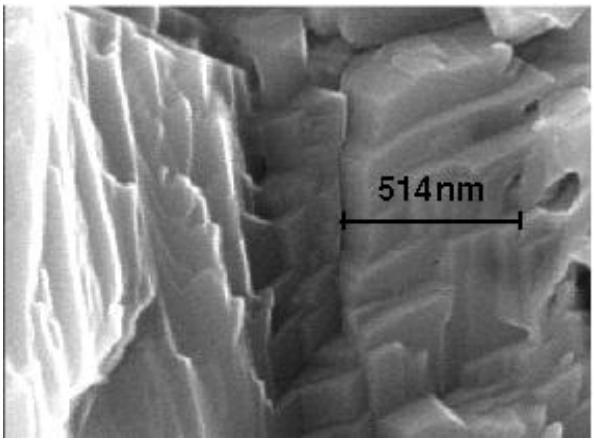

Graph.: 10-1 SEM of $Ag_2Cu_2O_3$ after DeNOx reaction. Formation of highly facetted spherical particles.

The melting point of silver metal is about 1089°C[65]. The exothermicity of the reaction may have influenced the separation of the metals. The formation of spherical particles during the high temperature treatment of $Ag_2Cu_2O_3$ is comparable to the behaviour of Ag-CuO particles in the same temperature range. This powders, generated by spray pyrolysis allowed a detailed view on its sinter characteristics. The preparation of this Ag-CuO mixtures followed the preparation routine developed for $Ag_2Cu_2O_3$ by using copper and silver nitrate The variation of the silver content and sinter temperatures between 600°C to 1000°C in air led to segregation and formation of spherical silver particles. The external particle morphology varied with the powder composition. Surface smoothness and particle sphericity increased with the silver content as proven by SEM. The internal morphology were similar for all tested composition as proven by TEM. At 95vol.% Ag, the degree of sintering retardation was minimal opposite to that at 60vol.%, and a temperature of 800°C, the sintering of Ag was almost eliminated[374].

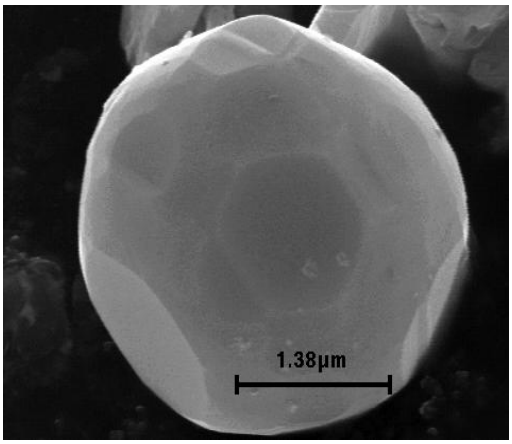

Graph.: 10-2 SEM of $Ag_2Cu_2O_3$ after OCM reaction. Formation of spherical copper-rich particles, the silver-rich material was sublimed to the reactor walls or to the quartz wool fibers.

Alloy formation was not detected after the OCM reaction at 800°C. Pure Cu is almost inactive for OCM, hence, the minor OCM activity, which was lost during the experiment, has to be attributed to the Ag sublimating from the hot reactor zone.

10.3.2.2 Oxidative ethane dehydrogenation by O_2 and NO

The oxidative dehydrogenation of ethane was also used to probe the activity of the oxygen species in $Ag_2Cu_2O_3$. Two different subsequent heating-cooling cycles were conducted. Only minor conversion of oxygen and C_2H_6 was detected up to 390°C (data not shown) caused by the stoichiometric destruction of the metal oxide as found for the oxidative coupling. Carbon doixide was the only product that was detectable as proven by a two cycle experiment at low temperatures (400°C) and high temperature experiment (800°C).

The structural alterations were subsequently characterised by SEM. After the first reaction cycle the material was sintered to larger, oval particles (images not shown). After the second reaction cycle, separation of copper and silver was again observed and spherical copper particles were detected with a silver copper alloy coating (images not shown).

Copper dispersed on oxidic supports, especially copper ion-exchanged zeolites, are known for their catalytic activity in the selective catalytic reduction of nitric oxide[375, 376, 377]. The micro-tunnel structure of $Ag_2Cu_2O_3$ system is comparable to that of copper-zeolites and allows oxygen diffusion through the lattice. It can be imagined that this structure plus the combination of Ag and Cu ions may activate NO for oxidative ethane dehydrogenation.

However, NO conversion was not detected. The stoichiometric reduction of the oxide may be responsible for the low oxidation of ethene.

The material was characterised by SEM/EDX after the catalytic reaction. $Ag_2Cu_2O_3$ was completely destroyed as expected from the catalytic tests already discussed. Spherical copper particles were formed from the rod-like starting material (data not shown), which were coated by a highly facetted silver-rich silver-copper alloy (data not shown).

In conclusion, $Ag_2Cu_2O_3$ is not active for high temperature partial oxidation reactions, but the observed low conversion of methane at 200°C is remarkable, and may indicate a labile oxygen species in this material.

10.3.3 Low temperature methanol oxidation

The oxidation of methanol is less demanding than the above reactions and may be used to characterise a possible low temperature activity of $Ag_2Cu_2O_3$. Only minor conversion of methanol to carbon dioxide and formaldehyde could be detected between room temperature and 150°C for a methanol to oxygen ratio of 3.0:1.0. The conversion increased between 150°C and 170°C. A spontaneous temperature overshoot at 170°C up to ~300°C in a few seconds led to 100% methanol conversion to carbon dioxide. After reaching the steady state reaction temperature of 290°C, the methanol conversion to carbon dioxide was 45% after 3h time on stream and 20% after 1d operation. After lowering the temperature to 150°C, the reaction ceased within 3h time on stream (Graph.: 10-3). It is important to note that the onset of the reaction occurred at much lower temperatures compared to silver (450°C) or copper (320°C) metal catalysts being comparable to that of dispersed copper catalysts (290°C).

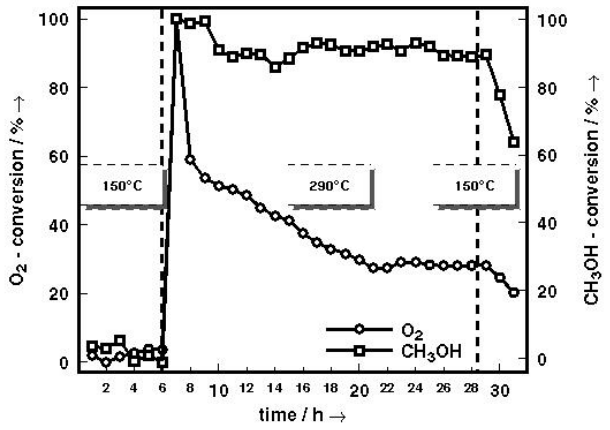

Graph.: 10-3 O_2 and CH_3OH conversion during methanol oxidation.

In order to obtain information about the relation between oxygen partial pressure and methanol conversion, the ratio of both reactants was varied. The material was heated up to 170°C in a 0.4:1.0 methanol to oxygen atmosphere. Then this ratio was changed stepwise to 2.6:1.0 (Graph.: 10-4). Each

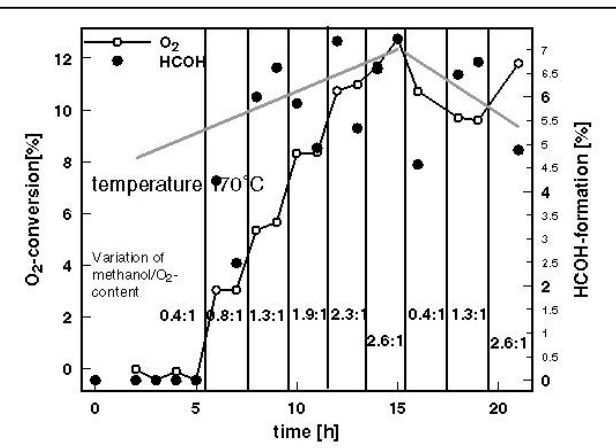

Graph.: 10-4 Formaldehyde and CH_3OH conversion during methanol oxidation. Stepwise variation of the methanol to oxygen ratio at 170°C reactor temperature.

new ratio was kept constant for 1h to reach equilibration. The oxygen conversion increased to 12% for the highest methanol to oxygen ratio. That means that the change of the catalytic activity of the material is indicated by the oxygen partial pressure. Due to that the conversion to formaldehyde is not remarkable influenced by the change of the oxygen partial pressure during the experiment.

SEM showed a less pronounced destruction of the material after the reaction at 170°C than after the high temperature reactions. Sintering of the rod-like particles was found despite the low temperature (Graph.: 10-5). EDX proved the homogeneity of the silver cuprate after the low temperature catalytic test. After the high temperature treatment at temperatures above 170°C the destruction of the material was again documented by a silver copper alloy formation.

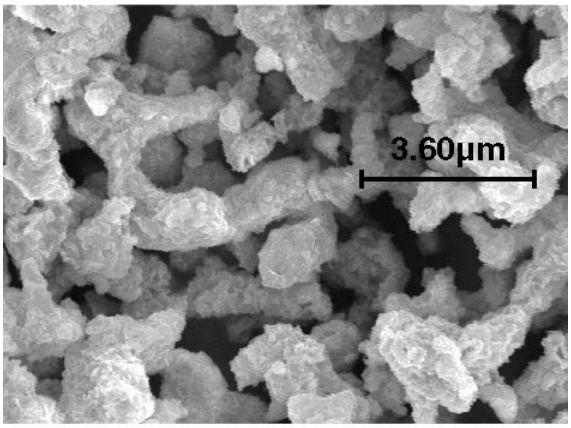

Graph.: 10-5 SEM of $Ag_2Cu_2O_3$ after methanol oxidation at 300°C. Sintered and highly facetted material.

Pure silver or copper catalysts do not show activity for methanol oxidation at such low temperatures of only 150°C. Hence, the silver cuprate is able to activate oxygen probably due to the special combination of the metal ions. Not very much is known so far about the behaviour of atomar dispersive copper clusters in partial oxidation reactions. Only some detailed structural aspects of the pure metal are documented in the literature[378,379]. Opposite to that the application of Cu-ZMS 5 zeolites in DeNOx reactions is well known but it is not possible to transfer this knowledge to partial oxidation reactions because of the different reaction conditions.

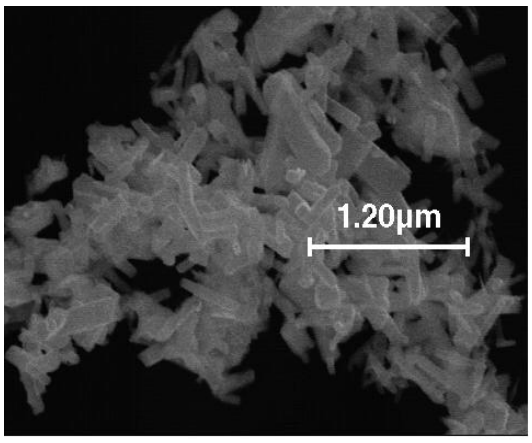

Graph.: 10-6 SEM of $Ag_2Cu_2O_3$. The untreated material consists of rod like particles with a mean length of 50nm.

The deactivation of the catalyst during the steady state experiment at 230°C was documented by the formation of an amorphous oxygen-containing silver copper alloy. The decrease of the methanol conversion is related to the proven phase separation, because pure Ag and Cu are not active for methanol oxidation at such low temperatures.

10.4 Morphology of the starting material

The morphology of the silver cuprate as determined by SEM and TEM comprises homogeneous rod-like particles with an average length of 50nm (Graph.: 10-6). EDX confirms the homogeneous appearance by the corresponding Ag:Cu ratio. The TEM results are highly interesting with respect to potential catalytic applications. The rod-like particles are covered by nano-crystals of about 5-6nm in diameter (Graph.: 10-7). At the moment information is not available whether this surface structures are formed in the electron beam of the microscope or whether it is inherent to the material. XPS experiments have proven that the particles are a silver rich material.

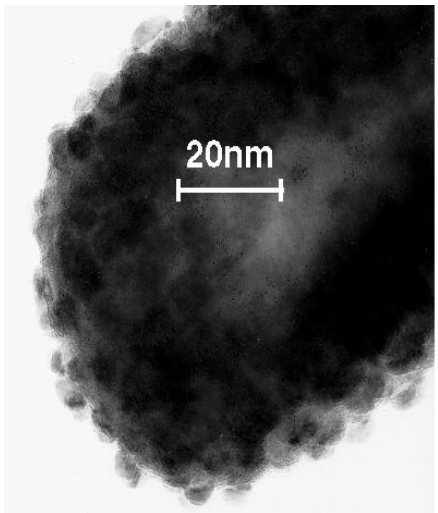

Graph.: 10-7 TEM of untreated $Ag_2Cu_2O_3$ material. Coverage of silver-rich clusters on rod like cuprate particles.

10.5 X-ray diffraction

The comparison of the diffraction patterns of $Ag_2Cu_2O_3$ with those of silver or copper oxides proved its purity. The lattice type of $Ag_2Cu_2O_3$ is tetragonal (a= 5.89, c= 10.7A) with the space group $I4_i/amd^{360}$. The crystal parameters of the silver and copper oxides are compared with those of $Ag_2Cu_2O_3$ in table 10-1.

	Cu_2O [30]	CuO[30]	Ag_2O[30]	AgO[51]	$Ag_2Cu_2O_3$[1]
Crystal parameters	cubic	monoclinic	cubic	monoclinic	tetragonal
	a=4.27Å	a=4.6837 Å	a=4.74 Å	a=5.892 Å	a=5.8857 Å
		b=3.4226 Å		b=3.4642 Å	
		c=5.1288 Å		c=5.4995 Å	c=10.6868 Å
		β=99.54°		β=107.509	
distances					
d_{Cu-O} /d_{Ag-O}	1.84 Å	1.95 Å	2.05 Å		1.858 Å (d_{Cu-O1})
d_{O-O}	3.68 Å	2.62 Å	4.10 Å		1.987 Å (d_{Cu-O2})
d_{Cu-Cu}/d_{Ag-Ag}	3.02 Å	2.90 Å	3.34 Å		2.130 Å (d_{Ag-O1})

Table 10-1 Crystal parameters of copper and silver oxides and $Ag_2Cu_2O_3$.

The $Cu^{[II]}$- and $Ag^{[I]}$-ions in $Ag_2Cu_2O_3$ have interesting co-ordination geometries[360]. The two different oxygen species in the lattice, as recognised by their distance to the co-ordinating metals, could be of relevance for catalysis. O1 is bound to two Cu and two Ag-ions, and O2 bounds to four Cu-ions. The resulting metal-oxygen distances are different as compared to those known for the pure copper- or silver oxides, with a longer Ag-O-bond and a rhomboedrically distorted Cu-O co-ordination. This special structure leads to a complex three-dimensional tunnel system. Each tunnel entry is as large as the Cu-O distance and renders possible oxygen diffusion through the lattice. The two different oxygen species in $Ag_2Cu_2O_3$ as indicated by XRD should may lead to two different O-species as detected by XPS.

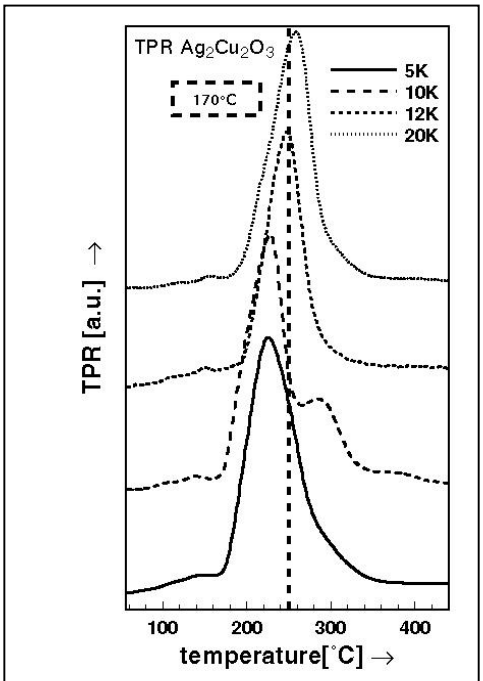

Graph.: 10-8 Rate dependence of TPR profiles of $Ag_2Cu_2O_3$.

10.6 Temperature-programmed reduction

Reaction conditions identical to the published TG/DTA reduction of $Ag_2Cu_2O_3$ were chosen for the TPR experiments[360]. TG/DTA showed that the reduction process occurs in one step[360]. TPR confirmed this result but

additionally revealed a small signal at about 170°C followed by the main signal at 220°C, whose position depended on the heating rate (Graph.: 10-8). It is remarkable that exactly at 170°C the start of the methanol oxidation reaction was observed. Catalytic reactions that require high temperature reaction conditions like OCM, or DeNOx would led automatically to the destruction of the material.

The reduction of large, spherical copper particles starts at temperatures above 320°C[380], while the reduction of nano-copper particles begins at 300°C[381]. Different to this, the reduction of $Ag_2Cu_2O_3$ starts at lower temperatures but irreversibly leads to copper silver alloys proven by SEM/EDX (data not shown) and phase separation (data not shown). Kinetic calculations based on the Avrami-Erofeev-model yielded an activation energy of 36kJ/mol for the reduction (correlation coeff. :96% for kinetic analysis). Other model dependent data analysis[382, 383, 384], like diffusion control did not give better results. This very low activation energy points to diffusion limitation of the reduction.

The Avrami-Erofeev-kinetics is based either on three-dimensional nucleation or core-shell formation of the reacted and the initial material. As proven by SEM, the redox process causes separation into silver and copper-rich phases which accordingly can be understood by the nucleation mechanism.

10.7 UPS/XPS of the redox behaviour combined with TEM and XRD

In order to reveal more details about the metal oxidation states during reduction, UPS/XPS experiments were conducted based on TPR and TG/DTA results[360].

The treatment of $Ag_2Cu_2O_3$ was already described in the experimental chapter. The possible ultra high vacuum effect on the redox state was explored but could not be detected[385]. Hence, this oxide is under the high

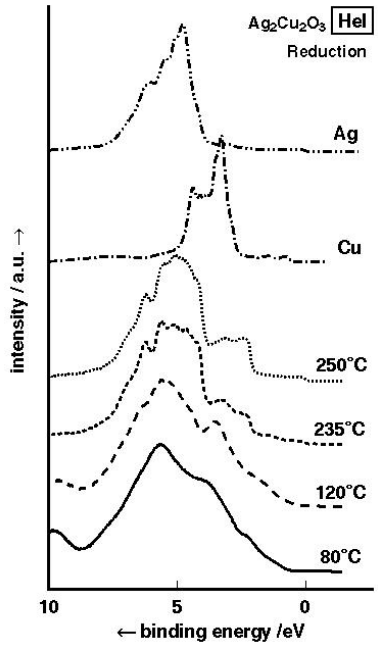

Graph.: 10-9 Comparison of the UPS-spectra for reduction at 80°C, 120°C, 235°C, and 250°C with reference spectra of Cu and Ad metal and the oxides.

vacuum conditions of ESCA. The carbon surface impurities of the oxide as prepared were lower than 5%. Table 2 compares the binding energies (B.E.) of Cu($2p_{3/2}$) as observed for $Ag_2Cu_2O_3$ and these reported for Cu-metal, Cu_2O and CuO (spectra not shown).

Compared to literature, the Cu($2p_{3/2}$) B.E. of 933.6eV is much higher than that of Cu metal at 932.3eV, Cu_2O at 932.4eV, and CuO at 933.2eV[386]. At best, the B.E. of the Cu($2p_{3/2}$) signal of $Ag_2Cu_2O_3$ can be compared to that of CuO. Hence, the Cu oxidation state in $Ag_2Cu_2O_3$ is close to $Cu^{[II]}$. In addition to the main peak, a shoulder was detected at still higher B.E. This satellite structure is well described in literature as characteristic for d^9 elements like metallic nickel or copper-dihalides and was explained by a cluster-configurations-interaction calculation[387]. The absence of this satellite structure in the case of Cu_2O allows easy differentiation between CuO, Cu_2O, and $Ag_2Cu_2O_3$.

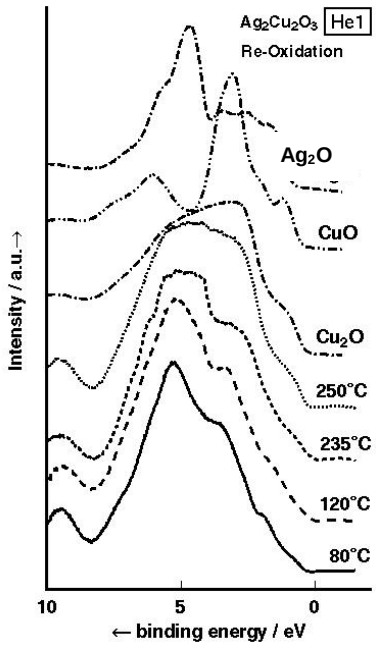

Graph.: 10-10 Comparison of the UPS-spectra for re-oxidation at 80°C, 120°C, 235°C, and 250°C with reference spectra of Cu and Ag metal and the oxides.

The B.E. of Ag($3d_{5/2}$) signal of $Ag_2Cu_2O_3$, on the other hand, is 368.1eV (Table 10-2) and compares well with the value for $Ag^{[0]}$ (spectra not shown)[388]. Satellite structures are not reported for Ag_2O and Ag_2CuO_3 as for CuO probably due to the instability of AgO under ultra high vacuum conditions[389].

Hence, the combined XPS results on the metal ions in $Ag_2Cu_2O_3$ suggest some alterations of the structural picture of this oxide as developed from XRD. Silver is present as zero valent atoms, while copper is present as $Cu^{[II]}$ and possible $Cu^{[III]}$ ions. Therefore, it seems unlikely that Ag is bound to oxygen in this unusual crystal lattice. The long Ag-O distances (see XRD[360]) support this.

An O(1s) B.E. was determined of 529.6eV for $Ag_2Cu_2O_3$. Opposite to the comparable Cu($2p_{3/2}$)B.E. of CuO and $Ag_2Cu_2O_3$, the O(1s) B.E.'s are different (Table 10-2). The observed value of 529.6eV is between that of 530.3eV for Cu_2O and that of 529.4eV for CuO and much higher than the 528.6eV for Ag_2O. (Table 10-2) compares the B.E.´s observed for $Ag_2Cu_2O_3$ with literature values.

Like the O(1*s*) spectra of CuO and AgO, the peak shape of the O(1*s*) signal of $Ag_2Cu_2O_3$ is asymmetric. This asymmetry was attributed to chemisorbed oxygen or adsorbed water[390]. However in case of Cu_2O, this peak is symmetric. Thus, the asymmetry cannot unambiguously be attributed chemisorbed oxygen or adsorbed water.

$Ag^{[I]}$ and $Ag^{[III]}$ ions form the AgO crystal lattice. The CuO structure may also be described by $Cu^{[I]}$ and $Cu^{[III]}$ ions. The presence of two different metal oxidation states should lead to two different oxygen sates and accordingly to two XPS O(1*s*) signals. In case of $Ag_2Cu_2O_3$, the two Cu(2*p*) signals support the existence of two different oxygen species as indicated by the asymmetric O(1*s*) signal. This asymmetry, however, does not arise from the combination of Ag and Cu ions as suggested by XRD, but by two different copper electronic states.

UPS measurements of the valence band show a combination of signals for O(2*p*), Cu(3*d*) and Ag(4*d*) niveaus (Graph.: 10-9, 10-10). For Cu_2O, the spectrum ends at ~8eV.[50] The Cu(3*d*) valence electrons are localised between 1eV and 4eV, and the O(2*p*) valence electrons are between 5eV and 8eV. For CuO, the high energy part reaches up to 15eV. The characteristic splitting of the Cu(3*d*) and O(2*p*) niveaus is not as clear in case of $Ag_2Cu_2O_3$ as for pure Cu_2O. It can be suggested that the spectral regime between 1eV and 5eV arises from Cu(3*d*) and Ag(4*d*) emissions and that the regime between 5eV and 12eV is due to O(2*p*) valence electrons.

Cu 2 $p_{3/2}$			
Cu	Cu_2O	CuO	$Ag_2Cu_2O_3$
932.3eV	932.4eV	933.2eV	933.6eV
Ag 3 $d_{5/2}$			
Ag	Ag_2O		$Ag_2Cu_2O_3$
368.0eV	367.6eV		368.1eV
Ag 3 $d_{3/2}$			
Ag	Ag_2O		$Ag_2Cu_2O_3$
374.0eV	373.6eV		374.2eV
O 1 *s*			
Ag_2O	Cu_2O	CuO	$Ag_2Cu_2O_3$
528.9eV	530.3eV	529.4eV	529.6eV

Table 10-2 Binding energies of copper oxides, silver oxides and $Ag_2Cu_2O_3$.

The integral intensities of the XPS peaks[391] are discussed in the following (Table 10-3 and Graph.: 10-11: 10-12). Spectral differences could not be detected as compared to the initial material after H_2 treatment at 80°C. The reduction started at 120°C and is described by a loss of oxygen and an increase of the Ag(3*d*) and Cu(2*p*) signal intensities. The reduction process reaches its maximum in the TG/TPR experiment at 235°C. At this temperature, the Ag(3*d*) signal has reached almost 50% of the total XPS intensity. The integral signal intensities of the other elements have decreased accordingly. This indicates the formation of a silver-rich surface. The integral oxygen signal intensity initially was 40% and decreased to 10% after this treatment. Oxygen could not be detected anymore after the final treatment at 250°C. The integral intensity of the Ag(3*d*) peaks was close to 95%, and that of the Cu(2*p*) signals close to 5%. This proved a phase separation forced by reduction.

treatment	Binding energies [eV]			
	Cu 2*p*	O 1*s*	Ag 3*d*	
untreated	933,68	529,47	368,19	374,15
Reduction 80°C	933,16	529,62	368,31	374,33
Re-Oxidation 80°C	933,06	529,32	368,12	374,11
untreated	933,57	529,43	368,11	374,10
Reduction 120°C	932,82	529,72	368,33	374,36
Re-oxidation 120°C	932,47	529,21	368,05	374,02
untreated	933,46	529,46	368,13	374,11
Reduction 235°C	932,58	530,35	368,15	374,16
Re-oxidation 235°C	933,42	529,34	368,24	374,20
untreated	933,68	530,84	368,15	374,19
Reduction 250°C	932,63	530,84	368,15	374,19
Re-oxidation 250°C	933,45	529,42	368,20	374,22

Table 10-3 Comparison of binding energies of $Ag_2Cu_2O_3$ with reference to the temperature programmed reduction or re-oxidation treatment before XOS/UPS measurement.

Reduction was found to be reversible after H_2 treatment at room temperature and 120°C. Re-oxidation at 120°C led to an oxygen content of 37% close to that of the starting material (40%).

Re-oxidation led to a complete change of the element distributions after the high temperature reductions as compared to those observed after H_2 treatments. At 235°C, the Cu(2*p*) signal reached 42%, while the Ag(3*d*) signal was reduced to 16%. The O(1*s*) peak intensity was 36% after the maximum re-oxidation temperature, whereas 2% of the integral Ag(3*d*) signal intensity was left.

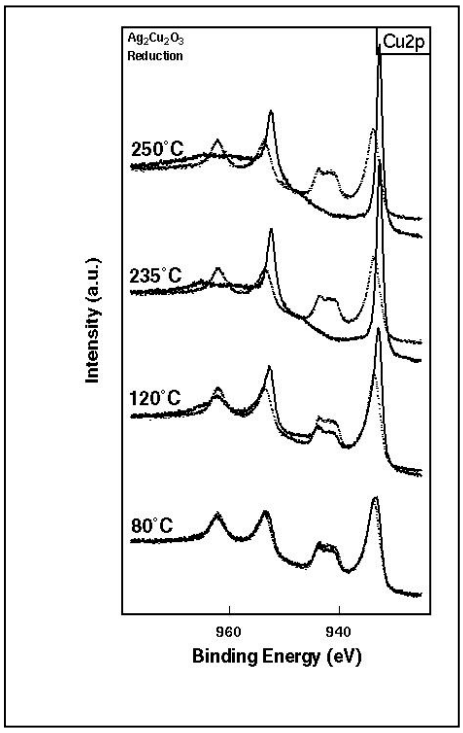

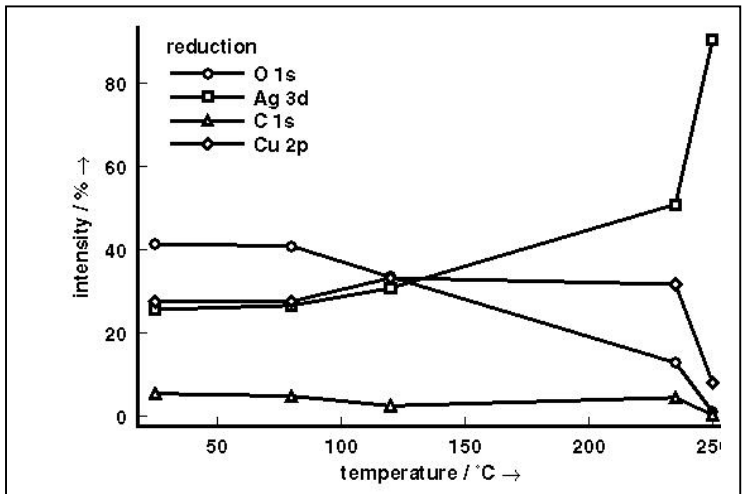

Graph.: 10-11 Comparison of the integral intensities for the XPS data of reduction. The formation of a silver-surface is forced during the reduction and the coating by a copper oxide rich phase was proven. XPS of the Cu2p signal.

This redox behaviour documents a high sensitivity of $Ag_2Cu_2O_3$ to temperature and atmosphere. Reduction of the material led to an irreversible phase separation at temperatures higher than 120°C. Ag covered the surface during reduction. The end of this process, the formation of a silver surface layer almost completely covered the copper. The high temperature reduction process is not reversible. Re-oxidation inverts this effect and a layer of copper oxide is formed on the surface.

TEM of the samples after ESCA reduction and re-oxidation revealed morphological changes of the particles as expected (images not shown). The clusters on the particle surfaces (data not shown) have grown after redox treatment at 120°C. Particle sintering was detected after redox treatment at 250°C and phase separation seemed to have occurred. This observation corresponds to the increase of the

Ag(3*d*) signal during the reduction, and the subsequent increase of the Cu 2*p* signal during re-oxidation.

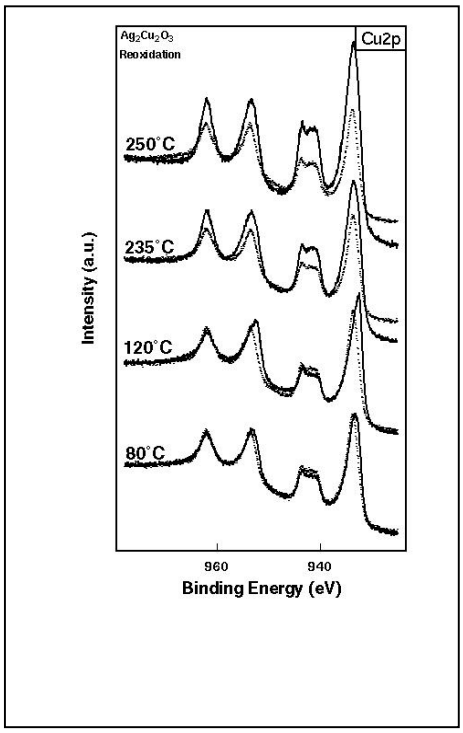

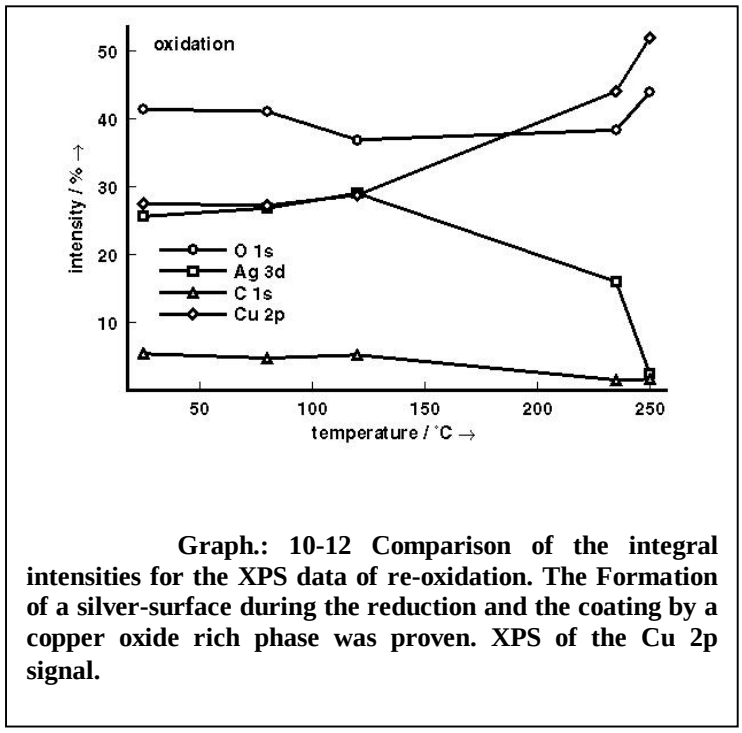

Graph.: 10-12 Comparison of the integral intensities for the XPS data of re-oxidation. The Formation of a silver-surface during the reduction and the coating by a copper oxide rich phase was proven. XPS of the Cu 2p signal.

Additional XRD analysis also confirmed the destruction after the redox treatments at temperatures above 120°C. The diffraction patterns of the samples treated at 235°C are composed of silver metal and copper oxides (data not shown)[391]. This confirmed the results of the catalytic test reactions. Activity for high temperature reactions arises after destruction of the material. The activity in the low temperature methanol oxidation may be due to easy surface redox processes.

10.8 Conclusions

The different oxygen–metal distances in $Ag_2Cu_2O_3$ suggested the possibility of active oxygen species for catalytic oxidation reactions[360]. The three dimensional channels of the crystal structure additionally suggested easy oxygen diffusion. The catalytic activity of silver and copper is well documented. Both elements are combined in $Ag_2Cu_2O_3$. Such a combination might increase the catalytic activity for such reactions.

The physicochemical characterisation of $Ag_2Cu_2O_3$ confirmed the reported structure.[23] The rod-like particles had homogeneous elemental distribution. Redox

treatments above 120°C led to phase separation of copper oxides and silver metal as proven by XPS/UPS. Reduction led to the formation of a silver-rich surface phase on a sintered matrix. Re-oxidation in opposite led to segregation of copper oxides to the surface.

The reduction process can be modelled by Avrami-Erofeev-kinetics of nucleation. Subsequent SEM and TEM proved sintering of the rod-like particles. Destruction was confirmed by XRD.

High temperature catalytic reactions, like oxidative dehydrogenation of ethane by NO and O_2, or OCM only revealed activity after the decomposition of $Ag_2Cu_2O_3$ to a copper-silver alloy above 450°C Partial oxidation products were not found. Most interesting, however, is the observed catalytic activity for methanol oxidation at about 170°C. Future investigations will be focussed on this low-temperature activity and explore the long time stability of this material and optimum reaction conditions.

11 The explanation: Copper particles

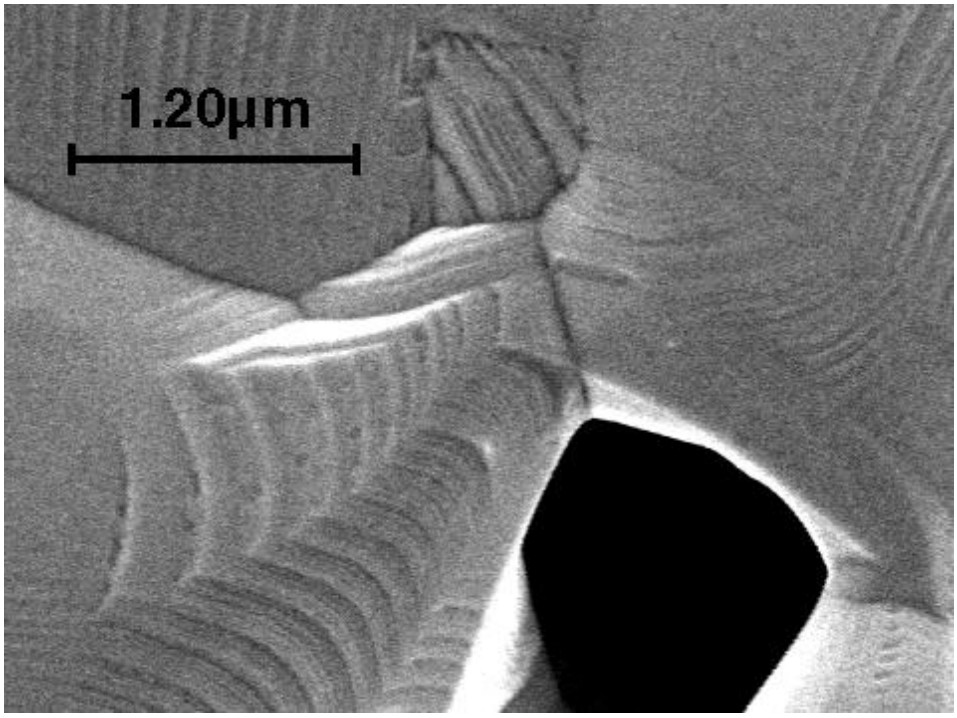

(SEM of a spherical copper particles surface after catalytic reaction treatment (MOX) at 500°C. Documented is the morphological change by the formation of pores, and facets.)

11.1 Reactor tests

Polycrystalline spherical copper particles with diameters of <20µm, 20-40µm, 40-60µm, 60-80µm, 80-100µm and 100-250µm (Heraeus AG.) and copper oxide powders, CuO and Cu_2O, (Aldrich Inc) were used. Methanol to oxygen molar ratios of 1:1 and 3:1 were applied. Helium was used to maintain typical total flow conditions of 150 ml/min. A tubular-flow reactor system was used with a quartz-tube of 4mm diameter. The undiluted material (5mg to 100mg) was placed in the tube using quartz wool plugs. The reactor system was coupled to a gas chromatograph (Varian Inc.) with an TCD (thermal conductivity detector) and a carboxen column (Varian Inc.). TG experiments under reaction conditions with online product monitoring were performed on a SEIKO system coupled to an evaporator for dosing methanol. An Atomica IMR-MS 1500 instrument with Kr/XE excitation of the mass spectra was used for evolved gas phase analysis. The samples were characterised subsequently by SEM using a Hitachi 4000 (see also experimental chapter No. 7).

11.2 Redox chemistry

The reduction of copper (I)-oxide, Cu_2O, as determined by TG/DTA, showed several exothermic and endothermic transitions in the temperature range between 220°C and 550°C (Graph. 11-1). The main TPR signal can be separated in three regimes: a broad exothermic signal at 300°C, a plateau between 380° and 420°C, and a main sharp reduction peak at

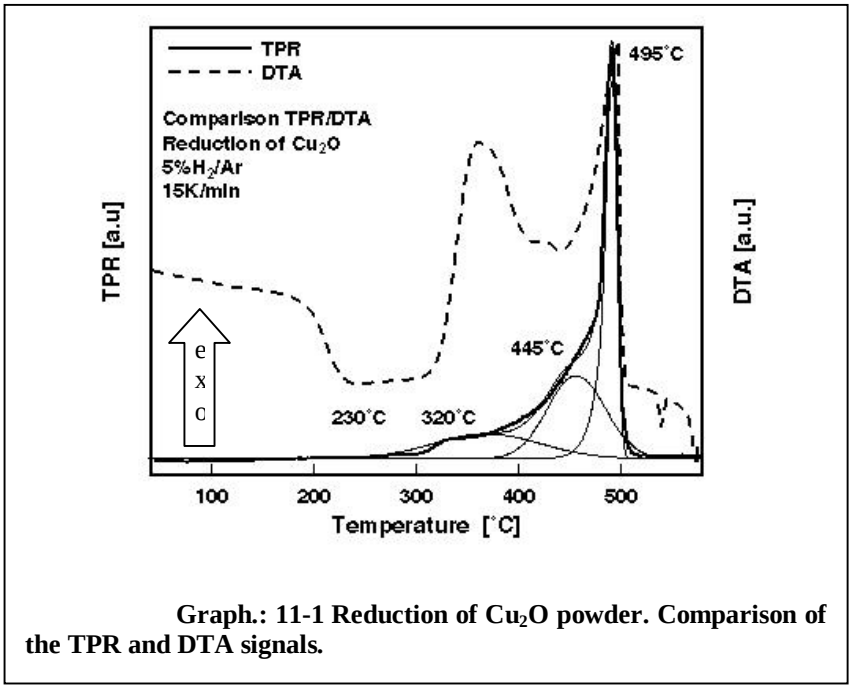

Graph.: 11-1 Reduction of Cu_2O powder. Comparison of the TPR and DTA signals.

500°C. Correspondingly, the TPR signal begins at 220°C and ends at 550°C (Graph.: 11-1). It comprises one sharp peak with an exponential tail at the low temperature side. Fitting by Gauss-Lorentzians[392] allows a detailed analysis (Graph.: 11-1). The reduction of the Cu_2O powder is governed by a continuous change of stoichiometry. It is not possible to isolate these intermediates. Hence, the reduction of Cu_2O seems to be a multi-step process.

The reduction of pre-oxidised spherical copper particles additionally showed that the peak separation of the TPR profiles is a function of the particle size. The exponential tail, seen for Cu_2O powder, is a sharp signal at 400°C for copper particles. The TPR profile comprises this sharp peak, a subsequent plateau between 380° and 420°C and the main reduction peak at 500°C. The positions of these signals depended on the heating rate too. A detailed kinetic analysis[393] is described in the following.

11.2.1 The kinetics of the reduction of copper(I) oxide, Cu_2O

The model-independent analysis of Cu_2O TPR reveals a strong influence of the morphology on the reduction. An activation energy of E_a = 69.59 ± 4.91 kJ/mol was determined for this process using the Kissinger method.

In the following, several different kinetic approaches for model-dependent and -independent analyses are discussed in detail to reveal the problems mentioned above (see chap. 6) by comparison of the obtained results.

Partial Area	Activation Energy [kJ/mol]	lg(A/s^{-1})
0.02	49.15+-2.62	0.39
0.05	66.65+-7.31	1.87
0.10	48.83+-0.31	0.52
0.20	55.96+-0.48	1.18
0.30	62.57+-17.04	1.80
0.40	72.48+-21.28	2.68
0.50	82.24+-26.25	3.54
0.60	88.46+-28.91	4.13
0.70	89.22+-30.00	4.35
0.80	86.08+-26.85	4.33
0.90	75.02+-12.50	3.83
0.95	65.22+-3.09	3.40
0.98	54.89+-28.96	2.98

Tab.: 11-1 Friedman analysis for Cu_2O reduction

Table 11-1 lists the parameters of the model-dependent analyses according to Friedman. The Tables 11-2 to 11-10 list the parameters for the other used models, i.e. the pre-exponential factors, the activation energies, the reaction orders, the used and calculated peak areas, and the correlation coefficients of the fits together with the standard deviations of each parameter.

Model	Parameter	Value	Stand. Dev.
n-th order	lgA1/s^{-1}	2.1353	1.03E-02
	E1 kJ/mol	67.3852	2.36E-02
	React.ord. 1	3.45E-02	2.31E-04
	Area1	4.00E+07	1.88E+06
	Area2	4.58E+07	2.73E+06
	Area3	1.23E+08	5.21E+06
	Correlation coeff.	0.9078	

Tab.: 11-2 Model dependent analysis for Cu_2O reduction, n-th order

Model	Parameter	Value	Stand. Dev.
3-dim. Diffusion Janders type	lgA1/s^{-1}	6.1754	0.9481
	E1 kJ/mol	130.6331	12.5152
	Area1	4.00E+07	4.73E+06
	Area2	4.58E+07	6.51E+06
	Area3	1.23E+08	1.30E+07
	Correlation coeff.	0.5941	

Tab.: 11-3 Model dependent analysis for Cu_2O reduction, n-dimensional diffusion Janders type

Model	Parameter	Value	Stand. Dev.
3-dim. Diffusion Ginstling-Brounstein type	lgA1/s^{-1}	5.1496	0.9481
	E1 kJ/mol	117.6039	0.4104
	Area1	4.00E+07	4.04E+06
	Area2	4.58E+07	5.82E+06
	Area3	1.23E+08	1.08E+07
	Correlation coeff.	0.6360	

Tab.: 11-4 Model dependent analysis for Cu_2O reduction, n-dimensional diffusion Ginstling-Brounstein type

Model	Parameter	Value	Stand. Dev.
n-th order Prout-Tompkins, autocat.	lgA1/s^{-1}	2.1179	1.24E-02
	E1 kJ/mol	61.7194	1.77E-02
	React.ord.1	0.2700	2.73E-02
	Exponent a1	0.5770	1.15E-02
	Area1	4.00E+07	1.00E+06
	Area2	4.58E+07	1.42E+06
	Area3	1.23E+08	2.80E+07
	Correlation coeff.	0.9617	

Tab.: 11-5 Model dependent analysis for Cu_2O reduction, n-th order Prout-Tompkins with auto-catalytic process.

Model	Parameter	Value	Stand. Dev.
n-th order with autocat. by B	lgA1/s^{-1}	1.6048	2.76E-03
	E1 kJ/mol	64.3358	1.54E-02
	React.ord.1	0.1953	1.90E-02
	lg Kcat 1	0.5208	1.61E-03
	Area1	4.00E+07	1.13E+06
	Area2	4.58E+07	1.62E+06
	Area3	1.23E+08	3.34E+06
	Correlation coeff.	0.9609	

Tab.: 11-6 Model dependent analysis for Cu_2O reduction, n-th order with auto-catalytic process by B.

Model	Parameter	Value	Stand. Dev.
3-dim. Avrami-Erofeev type	lgA1/s^{-1}	1.5401	0.1202
	E1 kJ/mol	58.6386	1.5186
	Area1	4.00E+07	1.57E+06
	Area2	4.58E+07	2.11E+06
	Area3	1.23E+08	4.07E+07
	Correlation coeff.	0.9200	

Tab.: 11-7 Model dependent analysis for Cu_2O reduction, 3-dimensional Avrami-Erofeev type.

Model	Parameter	Value	Stand. Dev.
n-dim. Avrami-Erofeev type	lgA1/s^{-1}	1.5921	6.91E-02
	E1 kJ/mol	59.7280	0.8910
	Dimension 1	4.0853	0.1455
	Area1	4.00E+07	1.24E+06
	Area2	4.58E+07	1.64E+06
	Area3	1.23E+08	3.30E+06
	Correlation coeff.	0.9427	

Tab.: 11-8 Model dependent analysis for Cu_2O reduction, n-dimensional Avrami-Erofeev type.

Model	Parameter	Value	Stand. Dev.
3-dim. Diffusion Janders type	lgA1/s^{-1}	3.1929	1.5810
	E1 kJ/mol	83.2722	19.4110
3-dim. Avrami-Erofeev type	lgA2/s^{-1}	1.4434	0.3681
	E2 kJ/mol	55.8767	4.9923
	FollReact.	0.1912	3.28E-02
	Area1	4.00E+07	1.80E+06
	Area2	4.58E+07	2.28E+06
	Area3	1.23E+08	5.41E+06
	Correlation coeff.	0.9411	

Tab.: 11-9 Model dependent analysis for Cu_2O reduction, Combination of n-dimensional diffusion of Janders type with 3-dimensional Avrami-Erofeev type.

Model	Parameter	Value	Stand. Dev.
3-dim. Avrami-Erofeev type	lgA1/s^{-1}	0.7090	0.1597
	E1 kJ/mol	45.8480	1.8420
3-dim. Avrami-Erofeev type	lgA2/s^{-1}	3.3076	0.2322
	E2 kJ/mol	78.6503	2.9267
	FollReact.	0.3780	1.89E-02
	Area1	4.00E+07	1.40E+06
	Area2	4.58E+07	1.36E+06
	Area3	1.23E+08	2.63E+06
	Correlation coeff.	0.9809	

Tab.: 11-10 Model dependent analysis for Cu_2O reduction, Combination of two 3-dimensional Avrami-Erofeev type reactions.

The comparison of the model-independent and the model-dependent analyses of the TPR of Cu_2O emphasises the major influence of the fit procedure used. Only the adaption of different models to the data can yield an estimate about the real reduction process.

In case of copper oxide, the “simple” kinetics of an n-th order process was tested as well as the enhanced Avrami-Erofeev model. The reaction was first treated as a one step reaction. Correlation coefficients as well as activation energies suggested in an n-dimensional diffusion process of the Prout-Tompkinks-type (Tab. 11-5). It is reasonable that diffusion is the parameter most affecting the reduction.

A better fit of the TPR was obtained after addition of a second reaction step to the model. The problems of the fit that arose for a diffusion-based model of the reaction kinetics led to the assumption that the reduction of the copper oxide powder is not only ruled by diffusion but also by nucleation.

The additional assumption of two, independent nucleation-controlled processes for the reduction of Cu_2O led to the best fit (Tab. 11-10). This result is supported by the values of the activation energies of the processes in comparison to literature data. However, nucleation is not independent of diffusion during a temperature-programmed experiment. Hence, it cannot be ruled out that, although nucleation led to the best fit, it does not describe the real process as well as a combination of nucleation and diffusion. The application of model depent kinetic analysis to the redox behaviour of spherical copper particles and copper powders as well as oxides is new. One main assumption as pointed out in the introduction is that the mechanism on which the reaction is based should be known to decide which of the kinetics is the right one. That is not possible so far. A relevant information for the correctness is the correlation coefficient. The mathematical evaluation of the

obtained data is not automatically in correspondence to chemical knowledge of the reaction condition and possible behaviour of the material. The seriousness of the relevant informations has to be assessed form case to case. The reduction of copper oxides or oxidic copper particles is possibly ruled by nucleation processes as supposed since years. The well correlation of the nucleation model by Avrami-Erofeev may valid this supposion.

Exaples for the fit of the different TPR data are shown in Graph.: 11-2. The fit was calculated by using Gauss-Lorentz equations. It is obvious that the mathematical interpretation allowed several different solutions expressed by the amount of functions used for one curve.

11.2.2 Kinetic analysis of TPR of oxidised copper particles

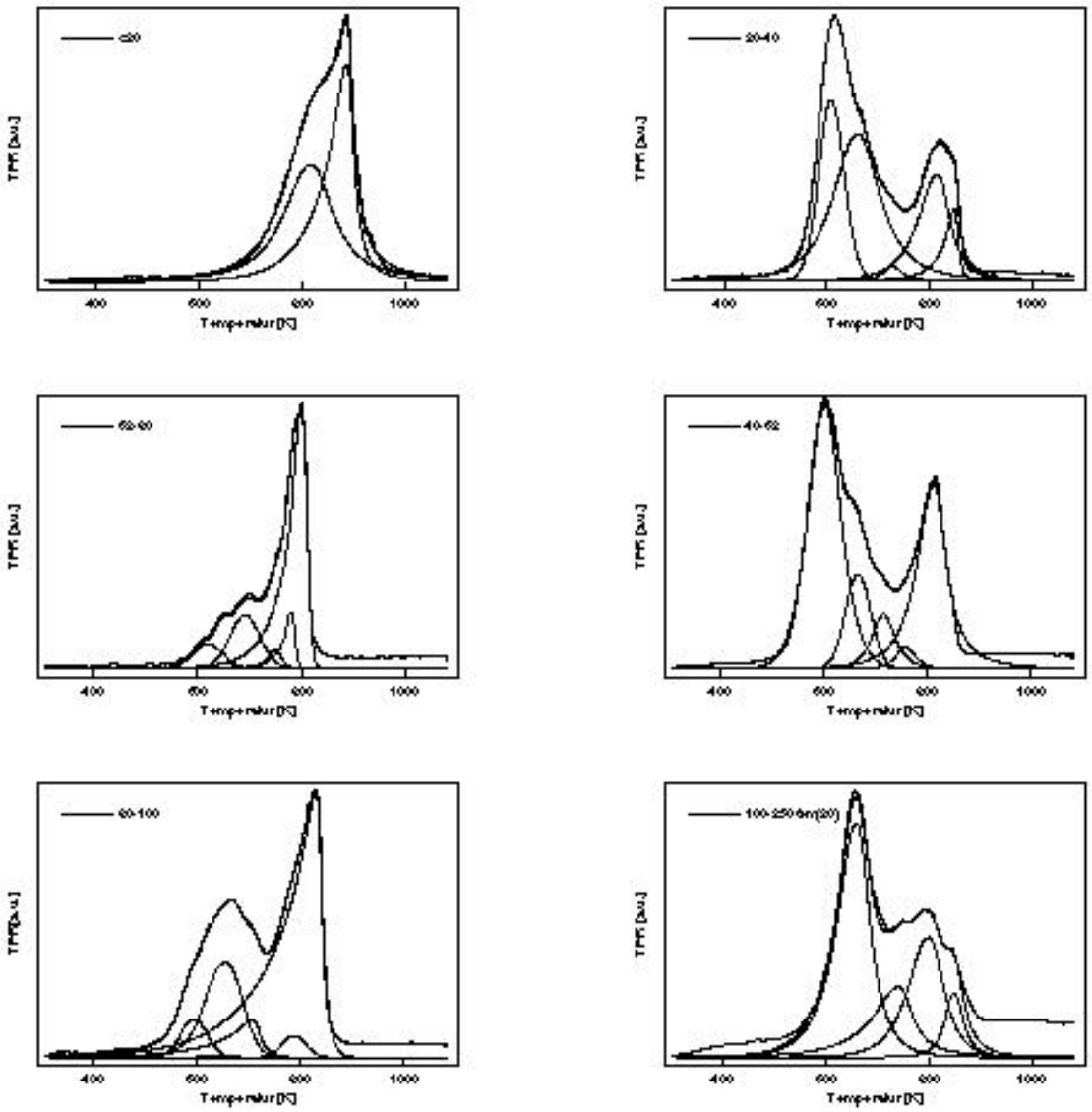

Graph.: 11-2 TPR profiles for different copper particle sizes.

The reduction of the pre-oxidised copper particles showed a particle size dependence of the reduction behaviour (Graph.: 11-2) The shape of the TPR-profile of the smallest particles (<20µm) was comparable to that of Cu_2O or CuO (CuO data not shown). It consisted of one broad peak in the temperature range between 600°C to 900°C with a maximum at 850°C (Graph.: 11-2). The bigger particle sizes led to an increasing separation of the TPR peaks. The low temperature regions of the TPR´s between 500°C and 700°C were combinations of several processes followed by the

main reduction peaks in the high temperature region. The relative intensities of these peak groups varied but the signal integrals were comparable for all particle sizes. For all tested particle sizes, the reduction profiles consisted of the described three peaks. In case of smaller particles, the main reduction peak was located in the low temperature region at about 600°C. Particle sizes bigger than 63-80µm in diameter showed the main reduction peak in the high temperature region around 800°C. The solution of hydrogen in the reduced material is responsible for the shape of the curves at higher temperatures.

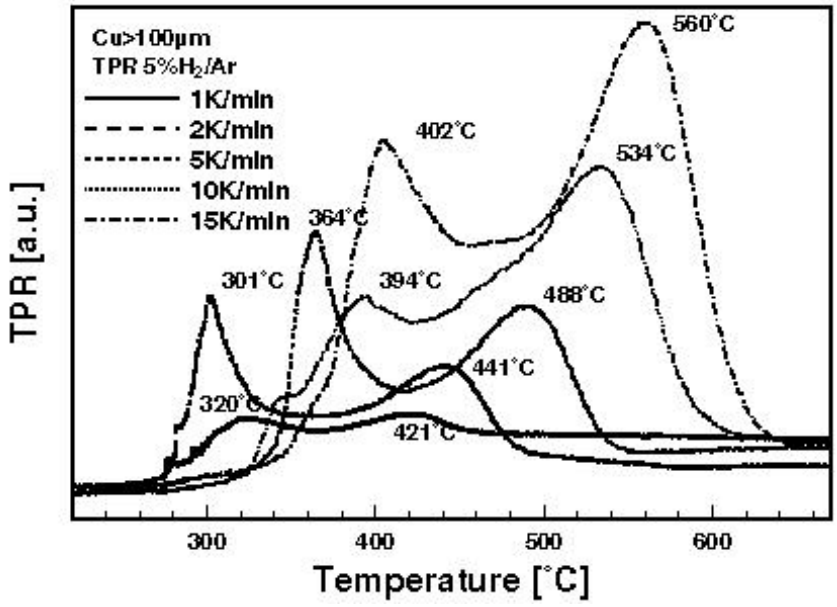

Graph.: 11-3 TPR profiles for the reduction of copper particles

A detailed kinetic analysis was conducted for the TPR of the 100µm particles (Graph.: 11-3), considering the heating rate dependence of the signal shapes and positions. The data evaluation procedure was made in the same way as described for the reduction of Cu_2O (s. above) and the fit parameters are listed in Tab. 5-11 to 5-13.

In the following, only the model with the best correlation coefficient is listed for the model-dependent analysis. Models which considered diffusion and auto-catalytic processes did not reasonably fit the experimental data.

Partial Area	Activation Energy [kJ/mol]	lg(A/s^{-1})
0.02	51.29+-4.93	0.50
0.05	40.51+-15.82	-0.11
0.10	28.33+-25.86	0.87
0.20	42.44+-15.31	0.32
0.30	36.74+-16.37	-0.26
0.40	41.47+-6.47	0.02
0.50	54.82+-2.32	0.95
0.60	70.91+-0.96	2.08
0.70	73.94+-1.16	2.38
0.80	73.24+-3.98	2.44
0.90	71.84+-9.05	2.45
0.95	70.50+-12.77	2.41
0.98	73.12+-22.71	2.56

Tab.: 11-11 Friedman- analysis for TPR of 100µm Cu particles

Partial Area	Activation Energy [kJ/mol]	Lg(A/s^{-1})
0.02	46.75+-0.14	0.10
0.05	51.74+-2.92	0.61
0.10	43.86+-1.63	0.04
0.20	42.00+-6.36	0.05
0.30	41.23+-8.76	0.03
0.40	40.44+-8.61	-0.03
0.50	43.83+-6.94	0.23
0.60	50.03+-5.36	0.69
0.70	55.97+-4.83	1.13
0.80	59.84+-3.96	1.43
0.90	63.30+-5.07	1.73
0.95	64.54+-5.84	1.85
0.98	65.47+-7.09	1.95

Tab.: 11-12 Ozawa-Flynn-Wall- analysis for TPR of 100µm Cu particles

Model	Parameter	Value	Stand. Dev.
n-dim. Avrami-Erofeev	lgA1/s^{-1}	0.9343	9.89E-02
	E1 kJ/mol	43.9462	1.1346
	Dimension 1	3.3286	0.1371
n-th order	lgA2/s^{-1}	0.7829	0.1729
	E2 kJ/mol	47.2096	2.3028
	React.ord. 2	0.9496	4.27E-02
n-dim. Avrami-Erofeev	lgA3/s^{-1}	2.6157	0.1896
	E3 kJ/mol	78.0045	2.7508
	Dimension 3	1.7887	4.78E-02
	FollReact.1	0.1847	9.41E-03
	FollReact. 2	0.4572	2.03E-02
	Area1	4386.7309	31.8643
	Area2	4208.4698	44.4800
	Area3	4847.4223	78.0339
	Correlation coeff.	0.9801	

Tab.: 11-13 Model-dependent Analysis for TPR of 100µm Cu particles

Important differences can be recognised when the different models of the TPR of copper particles are compared. The use of diffusion based models led to much higher activation energies for the reduction process. For the three steps, values between 43kJ/mol to 78kJ/mol were found using the Avrami-Erofeev model for nucleation. These values are comparable to those of the reduction of Cu_2O and seem to be an indirect proof for its correctness. The plateau was identified as an n-th order reaction type flanked by two processes of nucleation-type kinetics. The particle size variations enhanced the geometric effect excerted on the kinetics. Diffusion through as well as nucleation on increasingly bigger particles in this series led to different morphology-induced reduction mechanisms. The formation of already reduced parts on/in the particle next to oxygen-rich phases seems plausible. The TPR traces could be described by the core-shell model (Graph.: 11-4). Due to the complexity of the size-depending Cu-TPR, a fit with only three independent processes was insufficient.

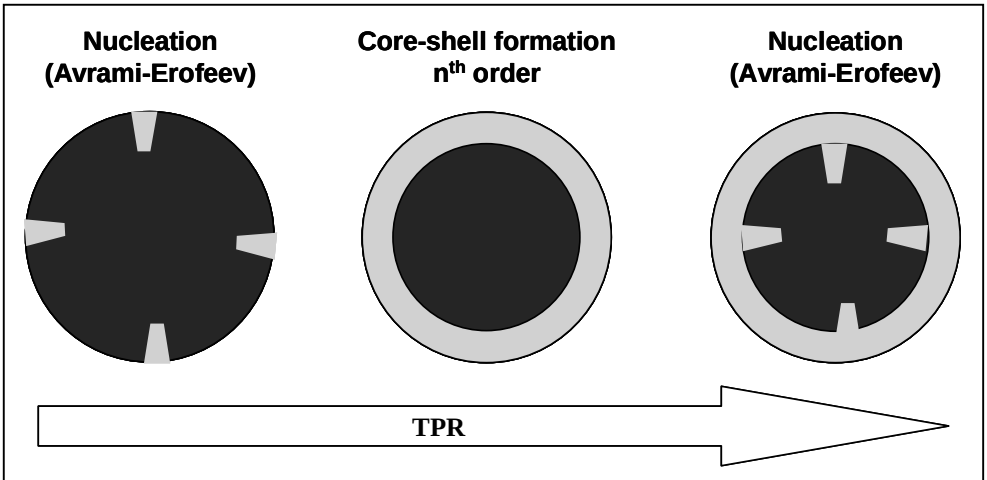

Graph.: 11-4 Model for nucleation process during TPR experiment.

Subsequent SEM only showed smooth particle surfaces without any signs for nucleation or grain boundary separations (data not shown). EDX proved reduction. The easy re-oxidation of copper was also indicated by low oxygen contents. It is important to note that the core-shell separation as suggested by the kinetic modelling was not experimentally observed by SEM, which proved the completion of the reduction process (data not shown). That proved the relation between core-shell formation and the influence of oxygen. The nucleation kinetics are valid for reduction as well for oxidation processes. It seemed to be that only the oxidation indicated the visible morphological changes.

11.3 The copper oxygen interaction

11.3.1 Materials

Oxygen (5.0) (Linde AG.) and helium (5.0) (Linde AG) were used for the pre-treatments. Spherical Cu-particles, 99.999% pure copper (Hereaus AG.) were used for SEM and TDS experiments. TDS measurements were made in an UHV chamber with an average background pressure of $3 \cdot 10^{-8}$ mbar. The vacuum was generated by oil-free Balzer's turbo pumps with pump rates of 240l/s. Analysis of the background gas shows water to be the primary impurity present. The desorption products were monitored a HIDEN-Hal2 quadrupole mass spectrometer (Hiden Inc.) coupled to a Next workstation[392]. A sampling rate of 0.65 scan/s was used. A water cooled, infrared oven (Stroehlein Inc.) was used for sample heating. The thermocouple was placed directly below the sample and was in direct contact with the quartz reactor tube. Linear heating was possible with this set up from room temperature to 900°C with a maximum heating rate of 130 K/min. The sample was transferred into the vacuum and pumped several hours (1d) to minimise water and carbon dioxide impurities. The dosage pressure for the TDS experiments was 1bar of oxygen. This dosage pressure is much higher than that usually taken for surface science experiments to render comparison to reactor conditions possible. Several dosage temperatures were used. All exposures were made for 2 minutes. 10 - 100mg of copper were used for all experiments. The sample were evacuated for five minutes prior to TDS.

11.3.2 TDS results: Interaction of oxygen with untreated copper particles

The main interest of this investigation, if possible, was to extend the silver model, as discussed above, to the interaction of copper particles with oxygen. The formation of two different high temperature oxygen species in Ag is related to morphological changes of the surface and bulk. Because of the different physicochemical properties of copper in comparison to silver, the oxygen-metal-interaction is certainly stronger and should happen in a different temperature range. The higher stability of the copper oxides relative to silver oxides also influences the result.

As described in the introduction, three different types of oxygen were found in silver catalysts. The low temperature species O_α, chemisorbed oxygen, O_β, dissolved in the bulk and the third species O_γ, interstitially dissolved in Ag (111) surfaces. The high temperature species O_γ is suggested to be formed by segregation of bulk oxygen to the Ag surface. A comparable oxygen diffusion in case of Cu should also be temperature dependent as indirectly proven by the catalytic activity of copper catalysts. TDS is a well suited method to detect an interrelation between the Cu-O-interaction and metal restructuring. To my knowledge an investigation of polycrystalline copper powders of different diameters is not reported yet. Most of the studies were made with metal foils or well defined single crystals. The experiments presented in the following should also help to bridge the material gap between catalysis and surface science[394].

Graph.: 11-5 shows oxygen TDS spectra of spherical Cu-particles with a diameter of 100µm. The spectra were obtained after having exposed the reduced Cu-particles to 1bar oxygen at temperatures between 300 and 800°C for 2min. The interval between the oxidation temperatures was 10°C. The desorption signals can be separated in three parts. Corresponding to the results for silver catalysts, the desorbed oxygen species were named O_α, O_β, and O_γ with increasing desorption temperatures. After oxidation at 720°C, the TDS signal is accompanied by a broad desorption signal at 780°C. The shape of the peaks reveals that not only “simple” surface desorption of oxygen was characterized. Diffusion of bulk dissolved oxygen to the surface has to be taken into account prior to O-recombination and O_2-desorption.

The occurrence of three TDS signals in different temperature regions indicates a similarity to the silver model and the TPR experiments. The diffusion of bulk oxygen combined with reconstruction hence may result in the TDS peak separation at at high temperatures. It is important to also note the obvious similarity to the separation of the TPR profiles in

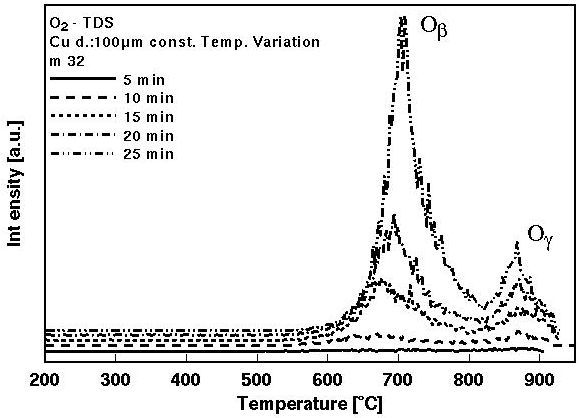

Graph.: 11-5 O_2-TDS from copper particles, amu 32. Three different signals were found in the temperature interval between 400 and 900°C.

three signals. It is remarkable that also the reduction of the material led to a complex reaction. The activation energies that were calculated for the desorption processes did not correlate to the calculated values using the TPR data. Taking the Redhead method into account for O_β, 234 kJ/mol, and O_γ, 252 kJ/mol.

The model independent method by Kissinger (see. above) led to an estimated activation energy of 42kJ/mol for the desorption processes following an 2^{nd}-order law following the stimation route by Niemantsverdriet as expected for O-recombination and O_2-desorption.. It should be emphasised, that this estimation can only describe a trend.

11.3.3 SEM analysis of the samples

In contrast to the TPR of the Cu particles, TDS after pre-oxidation led to the expected core shell separation. The oxidation-metal interaction led to the formation of the shell. The influence of pre-oxidation is documented by the thickness of the formed shell and/or its separation from the core. The high temperature treatment during TDS, however, led to sintered particles which does not allow further comparison with the isolated particles after TPR. The shells and cores showed faceted surfaces (Graph.: 11-6). This similarity to SEM observations after catalytic reactor tests indicates that the metal-oxygen-interaction in the catalytically relevant (methanol oxidation) temperature range around 500°C forces morphological changes of the Cu surface. These morphological alterations are again similar to those observed for Ag. The analysis by EBSD, however, did not lead to clear results. The surface orientations were determined to be Cu(111) and Cu(112).

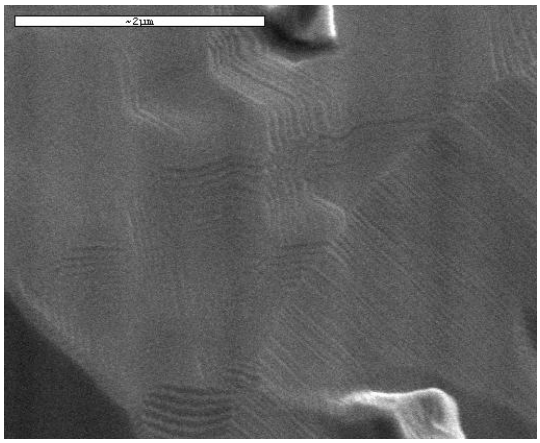

Graph.: 11-6 SEM of copper particles after TDS experiment. O_2 treatment at 520°C

11.3.4 TDS results: Interaction of oxygen with copper particles after methanol oxidation reaction

Copper particles were treated under methanol oxidation reaction conditions (see chap. 11.3.3) and subsequently investigated by TDS[394]. The oxidation prior to TDS was done at the same temperature and oxygen pressure conditions as those for the untreated particles. The O_2 TDS signal is also separated in two peaks. The first signal is formed after a treatment of adsorption temperatures between 400ºC to 700ºC and desorption temperatures of 400ºC to 600ºC with a maximum at 420ºC. The position of the maximum is about 100°C lower than the observed maximum (550ºC) for the particles investigated without methanol oxidation treatment. At lower temperatures no interaction was observed. This signal was interpreted to the low temperature species O_α. The signals that occurred at higher desorption temperatures were correlated to the O_β and the O_γ high temperature species.

The detection showed the desorption of a high temperature species at temperatures around 800ºC. The low temperature species characterised by a signal at 650ºC occurred after adsorption treatments of temperatures between 700ºC to 800ºC. The low temperature O_α signal at 400ºC was not detected.

It is interesting, that in the temperature range in which the methanol oxidation reaction was detected for copper particles in the reactor tests also a low temperature oxygen species was found. A direct correlation to the effects that were observed for silver catalysts is not possible in this context because of the different redox properties of both materials. But the TDS profiles may be compared to the TPR profiles that were discussed above. The separation into three different signals in the same temperature range proved that a comparable mechanism ruled the copper oxygen interaction. The kinetic analysis of the TDS data after methanol oxidation treatment led to activation energies of 247 kJ/mol for the O_γ species, 197kJ/mol for O_β, and 151 kJ/mol for the low temperature species O_α using the model independent method by Redhead.

11.3.5 SEM analyses of the samples

After the O_2-TDS experiments, the particles showed thicker shells as compared to the material after the methanol oxidation alone. Surface areas were

observed which made a molten impression (Graph 11-9). In addition, faceted areas were detected at the Cu surfaces (Graph 11-9). EBSD of the cores showed (001) as well as (110) oriented surfaces (data not shown). The shells always had a very disordered structure. EBSD characterisation did not lead to clear results. It is remarkable that in some cases faceting led to concentrically stepped surfaces (Graph.: 11-9). The surfaces of the shells, however, are not consequently structured by such facets and also show areas with no clear geometric forms. Difference surface orientations of cores and shells could not be determined in such cases. Silver catalysts showed also surface structures after the methanol oxidation reaction that could be correlated to the high exothermicity of the reaction. A kind of melting was also observed in this case. The high exothermicity of the methanol oxidation thus supported the melting of the copper metal surface at much lower temperatures. As shown in the introduction the copper melting point was found to be at 1089°C. The methanol oxidation at 500°C led to the same effect. The exothermicity render possible the restructuring of the thermodynamically stable surface orientations.

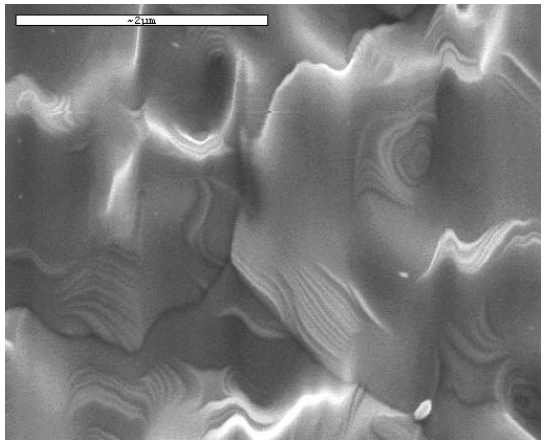

Graph.: 11-9 SEM of copper particles after TDS experiment. Treatment at 520°C after MOX at 520°C

11.4 Test reaction (TPRS) : methanol oxidation on poly-crystalline copper particles

The oxidation of methanol was chosen as low temperature test reaction to investigate the catalytic activity of Cu. The oxidative coupling of methane was used as the high temperature test reaction (chap. 11-7). Copper catalysts are known to be active for methanol oxidation but nearly inactive for the oxidative coupling of methane.

The methanol oxidation reaction started at 290°C. At 550°C, 100% conversion of methanol was reached. Upon controlled cooling to room temperature, methanol conversion was not detectable for temperatures below 220°C. The activity curves for subsequent heating-cooling cycles were comparable to this first cooling cycle. Hence, the Cu catalyst was in a different state during the first heating. (Graph.: 11-10).

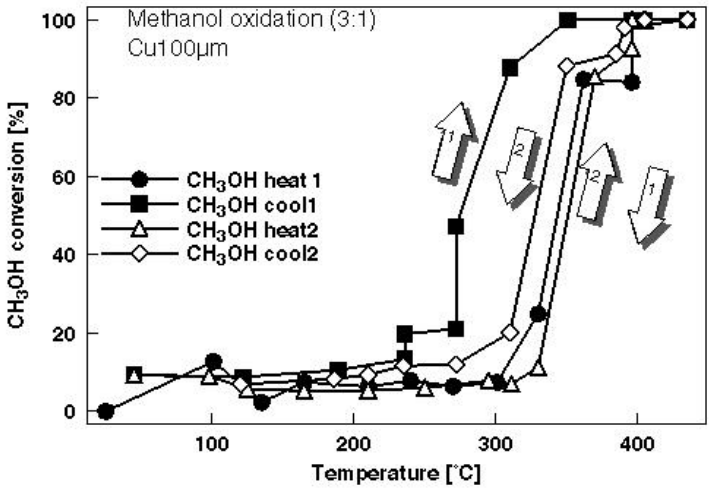

Graph.: 11-10 Methanol oxidation reaction (MOX). Hysteriseis of the heating and coooling curves in the temperature range bewteen 25°C – 450°C

Material	Cycle1	Selectivity / % // T/°C		Cycle 2	Selectivity / %	
		CO_2	CH_2O		CO_2	CH_2O
Cu_2O-powder	heat	87.2	12.1	heat	100.0	0.0
	cool	0.0	0.0	cool	100.0	0.0
CuO-powder	heat	78.3	19.8	heat	100.0	0.0
	cool	49.5	50.1	cool	100.0	0.0
Cu100µm	heat	61.7	38.7	heat	100.0	0.0
	cool	58.4	42.2	cool	100.0	0.0
Cu80µm	heat	60.2	39.0	heat	100.0	0.0
	cool	58.1	42.3	cool	100.0	0.0
Cu60-80µm	heat	64.3	33.9	heat	100.0	0.0
	cool	52.3	46.8	cool	100.0	0.0

Tab.: 11-14 Selectivity. Methanol oxidation reaction at 50% conversion.

In case of the methanol oxidation reaction, hystereses of the methanol and oxygen conversion were found in the temperature range between 220°C and 550°C comparing the heating and cooling cycles. The conversions of oxygen and of methanol showed a hysteresis in the first temperature-programmed heating and cooling cycle. Thus, the catalyst first remained at high levels of conversion upon cooling before the reaction ceased with decreasing temperature. The subsequent following heating-cooling cycles indicated catalyst deactivation and exhibited reduced hystereses with cycle number 2. The selectivity of the formaldehyde and carbon dioxide formation is shown in Tab.11-14 as a function of the particle sizes of the

tested material. The selectivity was determined of the ignition temperatures. Total oxidation is preferred in the first heating. The selectivity to formaldehyde was generally increased in the first cooling cycle. The second heating-cooling cycle with a reduced hystereses, however, revealed the preferred total oxidation. Both the reduced hysteresis and the catalytically altered selectivity indicate changes in the catalyst. The ignition temperatures for the methanol oxidation reaction shows the expected particles size dependence. Graph. 11-11 and 11-12 compare the oxygen conversions over differently sized Cu-particles. The largest Cu particles of 100µm diameter showed the reaction start at the highest temperatures of 450°C. The smallest Cu particles, showed a on set temperature of 290°C-300°C. For all particles the maximum conversion of 100% oxygen was reached ignition like in a very short temperature interval of ~2°C.

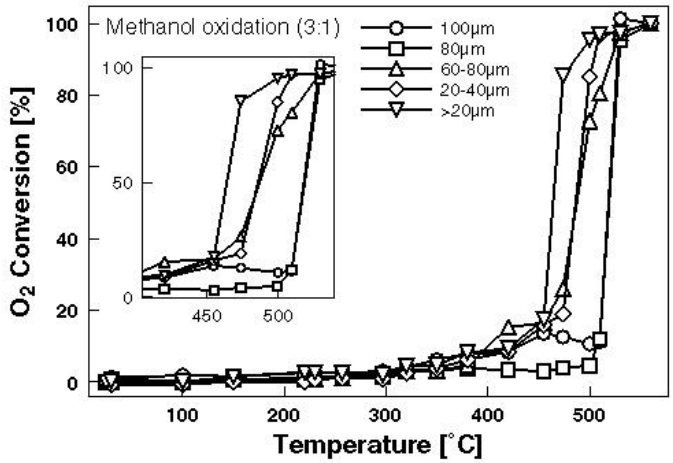

Graph.: 11-11 Particle size effects. Methanol oxidation reaction.

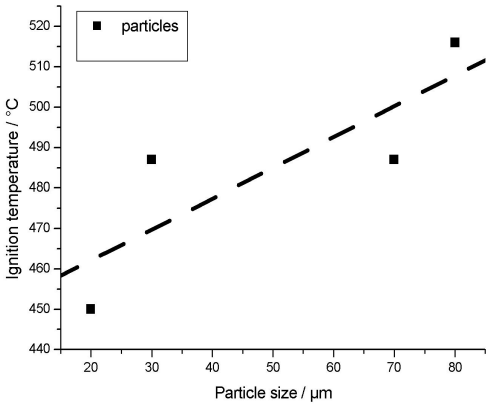

Graph.: 11-12 Comparison of particles size and ignition temperature.

This reaction hysteresis reflected the morphological change of the catalyst as proven by subsequent SEM. The former spherical copper particles were sintered. In addition, the spheres were separated into an oxygen-rich Cu-shell around an oxygen-free Cu-core as proven by EDX. Distances of 300 to 600nm were measured between cores and shells. Both, cores and shells showed highly facetted surfaces.

This phenomenon of core-shell formation can be understood by the three models that were described in the introduction of the thesis. The application of these models to the alterations of spherical Cu particles is discussed in the following.

11.4.1 Application of the Levenspiel model to the behaviour of spherical copper particles during methanol oxidation reaction

The Levenspiel model for spherical particles can easily be applied to the behaviour of Cu particles in the methanol oxidation reaction. The primary assumption of this model is the isolated non-porous spherical particle. Sintering and pore formation are neglected. The mathematical description of the temperature dependence of the chemically and diffusion-controlled model for the oxidation of the particles are given in Equ.: 11-1 and Equ.: 11-2.

$$1/T = 1 - 3(80/100)^2 + 2(80/100)^3 = 0.104$$

Equ.: 11-1 Reaction on copper particles controlled by diffusion through the oxide layer

$$1/T = 1 - 80/100 = 0.2$$

Equ.: 11-2 Reaction on copper particles controlled by chemical reaction

The graphic interpretation[395] of the model (Graph.: 11-13) compared to the experimental data showed that both reaction limitations together can explain the behaviour of the copper particles during methanol oxidation. Unfortunately, only a few data points could be obtained for this comparison, because the oxygen-containing shell was not found at the beginning of the catalytic activity. Still it can be concluded that a chemical reaction of Cu to copper oxide

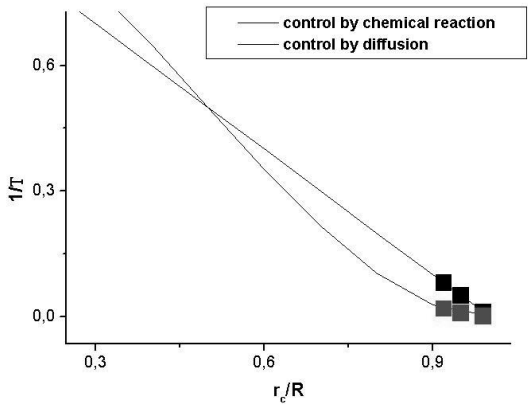

Graph.: 11-13 Graphic interpretation of the Levenspiel model. The curves document the chemical reaction and diffusion reaction control

occurs on one hand, the diffusion of oxygen controls the (oxidation of copper which happens during the methanol oxidation

After quenching to room temperature, only very small differences of the oxide shell thicknesses were determined for all tested Cu catalysts irrespective of the catalytic reaction, i. e. methanol oxidation and oxidative coupling of methane (see chap. 11.7.). One assumption of the Levenspiel model is the complete consumption of the catalytic material during the oxygen interaction. That is of course not the case for the catalytic methanol oxidation. Steady state operation would not be possible and a catalytic reaction would not be observed. However according to this model, the observed shell formation can explain the catalyst deactivation

11.4.2 Application of the Nabarro-Herring/Coble sinter-model to the behaviour of spherical copper particles during methanol oxidation reaction

The Nabarro-Herring or Coble model for pressure-less sintering can also be applied to yield an explanation for the Cu behaviour during methanol oxidation when some assumptions are made. The interpretation was derived from the obtained SEM pictures.

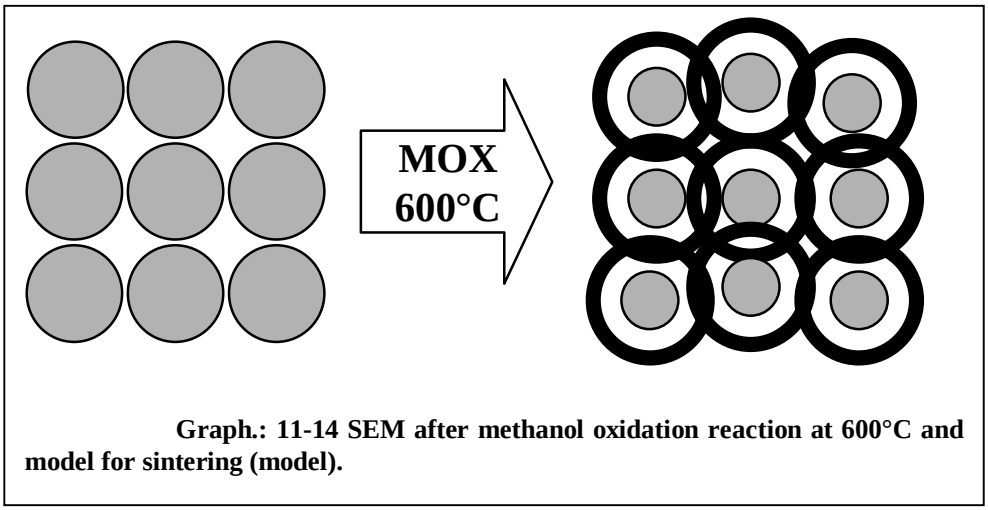

Graph.: 11-14 SEM after methanol oxidation reaction at 600°C and model for sintering (model).

A reactor of 4mm diameter was used for these test reactions. The reactor was ideally filled with a layer of spherical particles. It was taken care that all particles were placed in one plane layer (Graph.: 11-14, 11-15). From the diameter of the particles of 100µm, a pore maximum of $(n-1)^2$ can be calculated, with n being the number of particles. About 800 spherical Cu particles or a total volume V of $4{,}2*10^7$ μm^3 of Cu was used for this test. Accordingly, the total pore volume was estimated to be $4{,}8*10^5$ μm^3. After methanol reaction at 600°C, the pore sizes between the copper particles was reduced due to the sintering of the shells. Now, the mean pore volume

of the was calculated to be $3,0*10^5$ μm^3, assuming a rotational hyper-boloid model ($V= \pi h/3(2a^2+r_2)$[396]. Using the two particle model of sintering, the neck region was estimated to have a length of 2.9µm height with a mean radius of 3.8µm. Based on these assumptions, the contact region was calculated to 110μm^2. This resulted in a shrinkage of the pore volume of around 38% which explained the reduction of the contact area of the catalysts during the reaction. The catalytic activity as shown by the hysteresis decreased by about 30%. Thus, Cu sintering fully explains the decrease in activity.

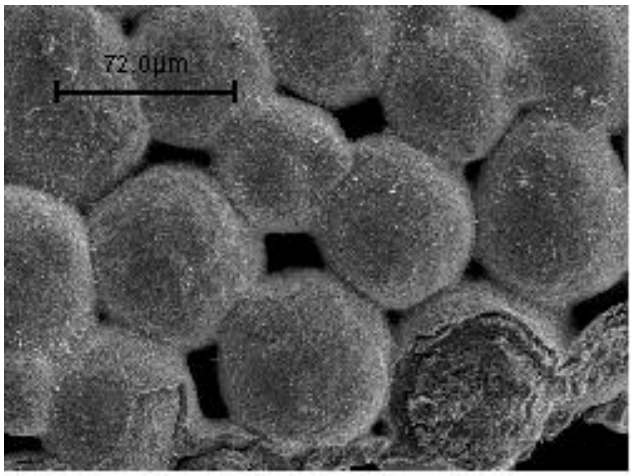

Graph.: 11-15 SEM. Particles after MOX treatment.

11.4.3 Application of the Pilling-Bedworth model to the behaviour of spherical copper particles during the methanol oxidation reaction.

The Pilling-Bedworth-ratio (PBR) can be used to model the Cu oxidation in the case that only oxygen and copper are the reaction partners. The Pilling-Bedworth model clearly simplifies real catalytic process which comprises many more reaction partners like methanol, carbon dioxide, formaldehyde, hydrogen and water. Additionally, the chemical influence of volume stress or strain during copper oxidation is not taken into account by the model. Information about the chemical composition of the shell or the core could not be obtained during catalytic action. The real density of copper, however, is most important for this stress/stain release.

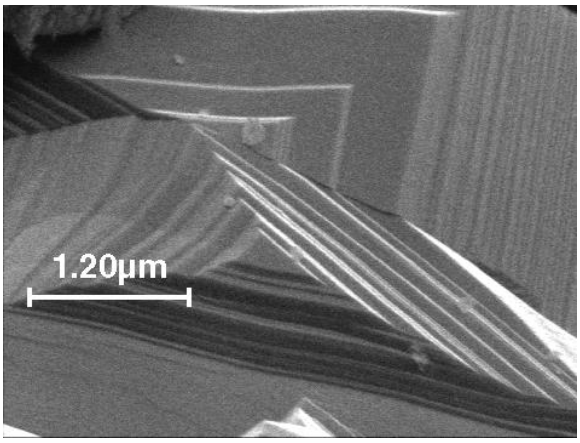

Graph.: 11-16 Pyramidal growth of facets on the copper surface

The PBR can be calculated for the case that only the copper oxides, CuO and Cu_2O, were formed during the oxidation reactions. The resulting PBR´s of 1.252 (CuO) and 1.503 (Cu_2O) correlate with the values documented in the literature[86].

SEM/EDX has proven that not only oxides were formed during the reaction. A core of copper metal still remained unreacted. So, the removal of the shell has to be interpreted by a kinetic model.

11.4.4 Interpretation of the surface science and kinetic models to the behaviour of spherical copper particles during methanol oxidation reaction.

As pointed out the surface of the copper catalyst was restructured after the catalytic action. Three different types of surface restructuring were observed simultaneously irrespective of the reaction atmosphere: Pyramidal growth, fractal growth and, concentric growth (Graph.: 11-16, 11-17, 11-18).

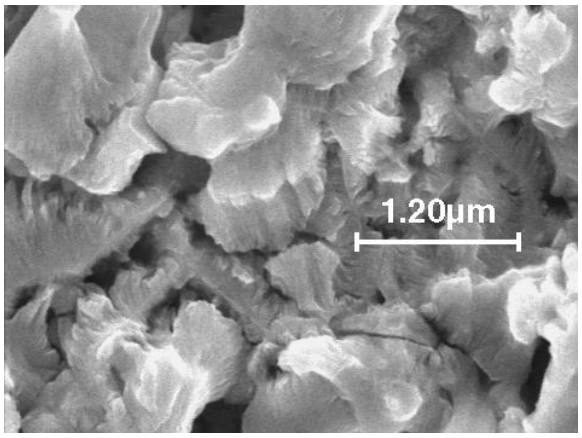

Graph.: 11-17 Fractal growth of facets on the copper surface

Cu catalysts, which were quenched to RT at maximum activity, mainly exhibited the concentric and pyramidal growth modes of facet formation.

A very simple relation for the facet growth was developed by Mullins[397, 398]. Irrespective of the transport process, the facet size L increases with time according to a power law,

$$L \sim t^n$$

Equ.: 11-3 Kinetic of facet growth by Mullins.

with n depending on the transport

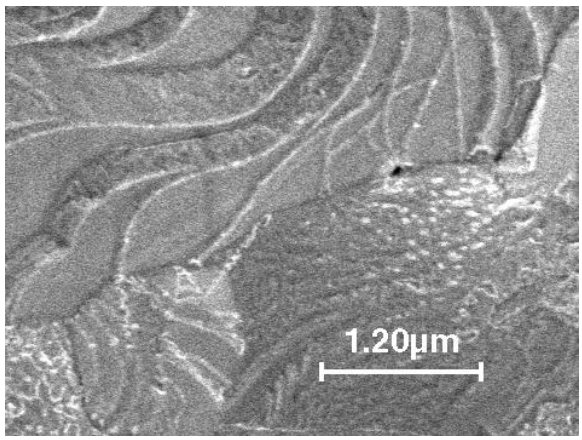

Graph.: 11-18 Concentric growth of facets on the copper surface

mechanism; n=1/4 for surface diffusion, n=1/3 for bulk diffusion and n=1/2 for evaporation-condensation. This model unfortunately cannot be applied due to the more complicated behaviour of polycrystalline copper particles. The size of the facets differed between the core and shell region. In most of the cases, the facets on the shells were smaller than the facets of the cores. This would suggest different facet growth processes for cores and shells, which is reasonable due to the different oxygen contents of the shells and the metallic cores.

A detailed characterisation of these facets is possible by EBSD[399, 400]. The orientation of the facets was determined to be mainly Cu(110) for the untreated copper particles before catalytic action. The interaction with oxygen at 600°C led to the re-crystallisation to Cu(111) facets or surface areas. After methanol oxidation at this temperature, Cu(111) facets were formed too. In this context it is important to note that exactly the same recrystallization to Ag(111) surfaces was found for Ag catalysts and related to the development of catalytic activity, because the dehydrogenating oxygen species, O_γ, is only stabilized in the Ag(111) surface[40].

The formation of the Cu(111) facets may accordingly be assumed to be related to catalytic activity of copper in partial oxidation reactions. For a clear statement, the nucleation of copper during redox processes has to be analysed by model-dependent kinetics.

11.4.5 Kinetic interpretation of the behaviour of spherical copper particles during methanol oxidation reaction

The kinetics of the methanol oxidation reaction was interpreted by using the model dependent analyses which were also used for the explanation of the redox behaviour of Cu-particles and oxides. Only a few models fit to the catalytic data (Table 11-15 to 11-16).

Model	Parameter	Value	Stand. Dev.
n-th. order	lgA1/s^{-1}	1.7172	2.3592
	E1 kJ/mol	23.0510	20.6170
	React.ord. 1	1.2102	2.7976
	Area1	12864.4458	7372.9414
	Correlation coeff.	0.9415	

Tab.: 11-15 Model dependent analysis for methanol oxidation, n-th order reaction

One problem of a kinetic investigation of a real catalytic process could be the increase of participants of the reaction and the induced morphological changes of the catalysts during the reaction Sintering and possible surface processes are neglected by several kinetic models

It is important to note that only three models could be adapted to the experimental data. All other diffusion-based, auto-catalytic kinetic models did not lead to acceptable results. Similar to the model TPR reaction, the catalytic methanol oxidation is not governed by a nucleation process following the Avrami-Erofeev kinetics as proven by SEM. The obtained reaction data seems to follow an nth-order kinetics for the oxygen conversion rate.

The exact definition of the reaction order is difficult. The kinetic interpretation allowed a second order kinetic as well as a first order kinetics because of the model dependent analysis. A second order kinetics would directly correlate to the results obtained form the TDS experiments. With that, the second order kinetics for the methanol oxidation may be suggested. The comparable core-shell formation after reactor tests as well after the TDS treatment allowed the assumption of comparable mechanisms for the oxygen activation in both processes. A simple assumption is that if the result is the same in different treatments the induction for this results could also be the same. The core shell formation and the faceting of the materials surface is due to the oxygen interaction. After reactor test and after TDS oxygen treatment mainly the copper (111) surfaces were found. The desorption signals for oxygen O_α species occurred in the temperature range around 400C in which the methanol oxidation reaction showed the maximum conversion rates. At the higher temperatures between 700C to 900C the total oxidation for methane was proven (see below). This behaviour would support a strong relation between the catalytic behaviour of copper to that of silver catalysts. As pointed out before, the restructuring of the surface is related to the diffusion properties of oxygen during the reaction. Copper showed restructuring as well, and the formation of different oxygen species.

11.5 In situ TG/DTA experiment

The methanol oxidation oscillated in the temperature range between 250°C and 550°C [401], characterised here in this work by the DTA signal (Graph.: 11-20). Oscillations of the corresponding the TG or DTG data were not detected probably due to the too low sensitivity of the apparatus. Alternatively, mass changes of the catalyst did indeed not occur and the oscillating DTA signal arises from the reaction exothermicity and heat transfer limitations.

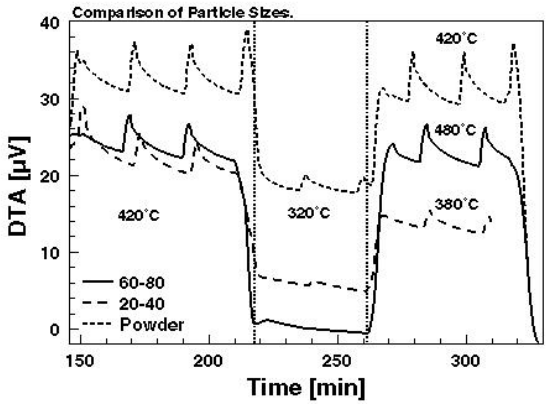

Graph.: 11-20 Temperature dependence of the oscillative behaviour durig the methanol oxidation reaction

Depending on the reaction temperature and the Cu-particle sizes, exothermic DTA signals were detected with a frequency of 20min. The oscillating signals are described by a fast vertical increase indicating an exothermic reaction followed by an exponential decay to the baseline. The smallest Cu-particles, or Cu-powder respectively, showed the highest amplitude of the DTA nearly 10µV. It was estimated that the smallest particle size e.g. the oxide powder as starting material led to the highest conversion rates. That supported the suggestion of a heat transport limitation problem using the TG/DTA equipment as reactor system. A TG-reactor temperature below 300°C led to a reduction of the oscillating amplitude. Re-heating to the initial temperature re-started the oscillations with the same frequency. A variation of the oxygen to methanol ratios from 3:1 to 1:1 in the gas phase, (data not shown) did not affect the oscillations, neither the frequency nor the amplitude.

The gas phase also showed an oscillating behaviour corresponding to that of the DTA signal (Graph.: 11-21 , 11-22). During the fast increase of the DTA-signal, the methanol peak intensity as measured by amu 31 reached its minimum. Parallel to the DTA peak maximum, the oxygen conversion is also at its maximum. Accordingly, the exothermic DTA signal corresponds to maximum methanol oxidation. The signal

for methanol, is nearly the mirror image of the formaldehyde signal as measured by amu 29. The led to the supposition that the formaldehyde was formed via the oxidative dehydrogenation route. The direct dehydrogenation would follow a endothermic reaction path.

The second product carbon dioxide reached its maximum production rate shifted to the decreasing branch of the DTA signals.

Long time experiments showed that the oscillations did not change, neither their shape, frequency, nor amplitude during several hours. The whole oscillating reaction is additionally governed by a second process after 12 hours on stream. The base line of the DTA signal additionally oscillated with a frequency of three hours. The origin of this phenomenon is not understood yet.

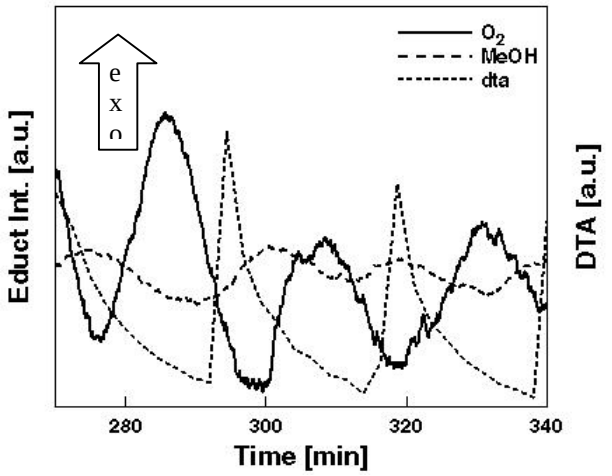

Graph.: 11-21 Oscillating behaviour of the evolved gas phase during the methanol oxidation reaction. The spheres above the reaction data symbolize the states of reduction/oxidation during the reaction

It should be emphasised that the maximum oxygen conversion was reached when the methanol conversion was on its minimum. This clearly implies that a second process has to be operative besides the catalytic oxidation reaction which consumes oxygen. Because of the partial oxidised character of the Cu particles proven by SEM (see below), the cyclic re-oxidation of the reduced Cu particle surface is this second oxygen

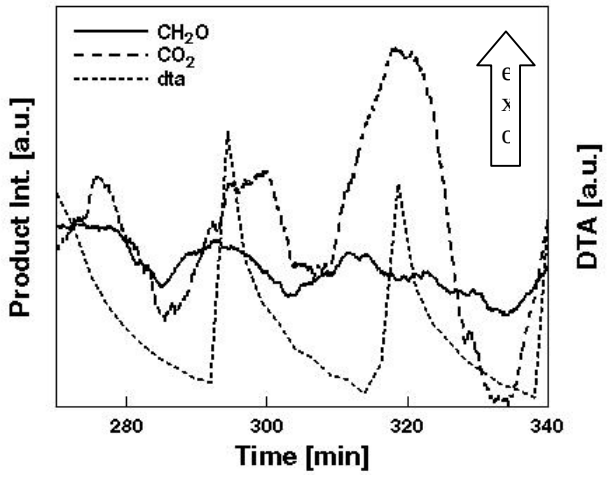

Graph.: 11-22 Oscillative behaviour of the products gas phase during the methanol oxidation reaction. The spheres in top of the graphic suggests a state of reduction/oxidation during the reaction

consuming process[80]. In light of these observations, the oscillating reaction could be understood as a cyclic oxidation-reduction of the Cu surface. High methanol and low oxygen conversions are reached for high oxidation degrees of Cu. This high methanol conversion leads to high exothermicity and to the reduction of the Cu surface. The methanol conversion decreases while Cu becomes increasingly re-oxidized, hence the oxygen conversion increases until the cycle starts again. As pointed out in the beginning oscillations during the methanol oxidation reaction on copper catalysts is not a new phenomenon. The investigation of copper foils by microscopy and also UPS/XPS measurements have proven the complex interaction of gas phase and metal or oxidic surface. The main difference to this oscillations is in the frequencies. In contrast to the TG/DTA reactor experiments frequencies of minutes or seconds were generated by changes of the methanol feed[34].

The Cu particles prior to catalytic action are characterised by an inhomogeneously oxidised surface. The inhomogeneous distribution of oxygen in core and shell after the catalytic test was found to be characteristic for all samples. SEM subsequent to the TG-catalysis experiment revealed a change of the Cu-morphology. The surface of the particles was completely restructured. The observed surface restructuring was similar to the observations that were made for the copper particles after the test reactions in the tubular flow reactor. An oxygen-reduced core was surrounded by an oxygen-rich shell. The shells of the particles were sintered together. Shells and cores showed highly facetted and porous surfaces. The facets were formed by small crystallites with mean sizes between 300nm to 600nm. The observed pore formation in the shells underlines the assumption that the catalytic reaction, occurring at the outer surface, also affects the bulk. The formation of oxygen-rich shells around metallic cores confirms the model of cyclic redox processes proposed above for the oscillating DTA signal and evolved gas phase.

11.6 Short-contact-time reactor for methanol oxidation reaction

A short-contact-time reactor system was also tested for the methanol oxidation reaction, in an attempt to reduce the contact times to such levels that the O_2 conversion would be below 10%, necessary for the precise determination of the reaction kinetics and reaction orders. Oxygen to methanol ratios, 1:1 or 1:3, were

chosen similar to those tested in the tubular flow reactor. The copper tube reactor was used without any pre-treatment. The total flow was 120ml/min identical to that in the TG and the flow reactor system The reactor length was 10mm with an inner diameter of 2mm. This led to a contact time shorter as compared to the copper particles in the “usual” tubular flow reactor. The maximum temperature that could be reached was 450°C. The methanol oxidation reaction started at temperatures above 200°C as proven by a mass spectrometer signal for formaldehyde (data not shown).

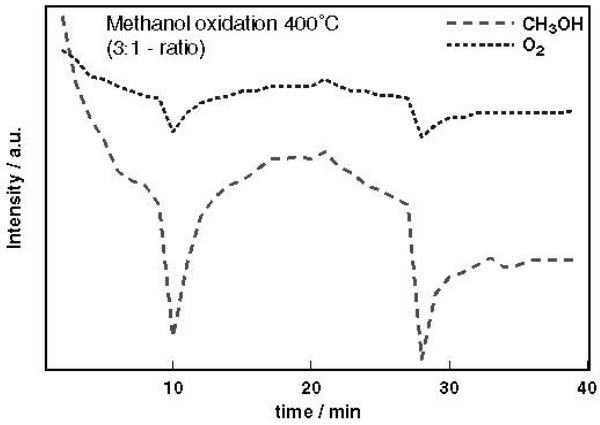

Graph.: 11-23 Oscillations during methanol oxidation reaction at 300°C, methanol and oxygen signal at 400°C.

The reaction showed oscillations with almost the same frequency than that of the oscillation which was detected on the TG/DTA equipment (Graph 11-23). The oscillation of both the oxygen as well of the methanol conversion signals was detected between 300°C and 500°C with an interval of 18min. Despite the shorter contact time, the oxygen conversion was still below 100% (for the chosen reaction conditions. However, the signals for methanol and oxygen showed an in phase oscillating behaviour. The maximum conversion was reached for both compounds at the same time opposite to the results obtained for the experiment on the TG/DTA apparatus. The difference between the oscillations determined for particles opposite to the Cu tube may be induced by the different heat transport of both materials. Comparable measurements of the methanol oxidation using different amounts of copper rings showed a comparable behaviour to that of the copper tube. There the oscillations appeared in the temperature range between 320°C to 400°C. The oxygen and methanol conversions were determined to decrease or increase parallel. Channeling effects that caused this behaviour may supported the oscillative behaviour of the copper tube.

Unfortunately, the contact times could not be reduced to such an extent that differential reactor conditions were reached. Hence, a detailed kinetic analysis

was not possible. But it should be mentioned that similar reaction oscillations were observed independent of the reactors used.

11.7 Oxidative coupling of methane, OCM

In case of the OCM reaction, oxygen conversion started at 650°C and reached a first maximum at 750°C (Graph 11-24). 100% oxygen conversion was detected at this temperature. The oxygen conversion dropped with further increasing temperature. A second maximum at 850°C with an oxygen conversion of 80% characterised the beginning gas-phase reaction. The controlled cooling cycle did not reproduce the first maximum of O_2 conversion at 750°C. Thus, again a hysteresis was detected between the heating and cooling cycles. The activity curve for all following cycles was parallel to that of the first cooling ramp.

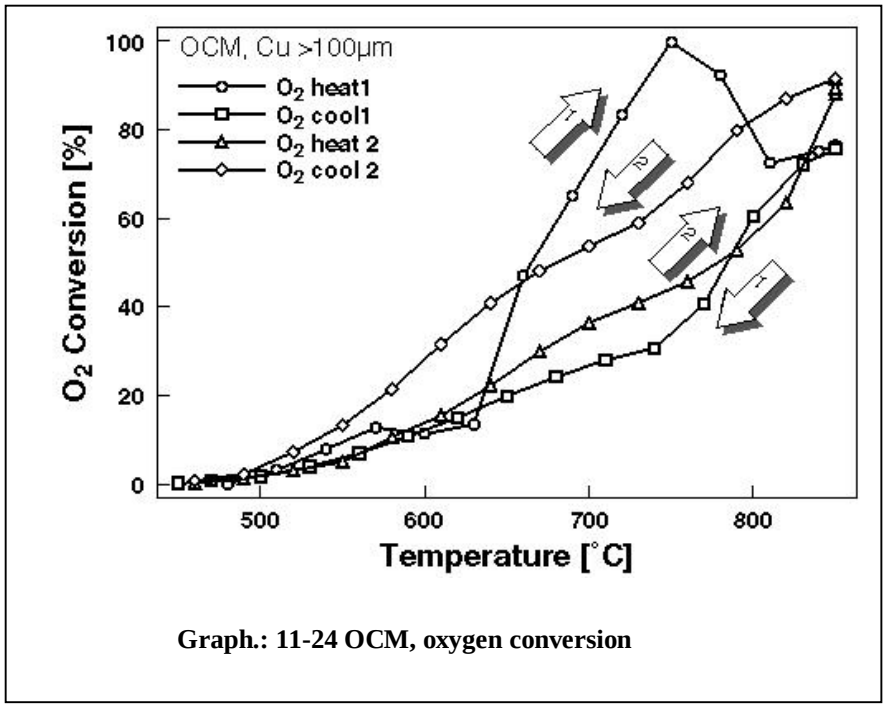

Graph.: 11-24 OCM, oxygen conversion

In comparison to the low temperature methanol oxidation reaction the high temperature reaction led to a deactivation of the catalyst. This behaviour was found for all tested particle sizes.

The selectivity for ethene is near 2% for an oxygen methane ratio of 5:1. The variation of this ratio to higher methane concentrations in the feed led to the formation of carbonaceous deposits at the copper surface. The same result was obtained after steady state operation at 800°C for more than two days. The already low activity of Cu for OCM continuously decreased during this time period to 50% oxygen conversion.

Copper thus behaved completely different in the OCM reaction than Ag for which reasonable activity and selectivity in OCM was found and correlated to the recrystallization of (111) facets containing the dehydrogenating $O_{\square}$

In the case of silver catalysts the OCM facility is directly correlated to the occurrence of O_γ as proven by TDS measurements[65]. In the case of copper catalysts, ethene or ethane formation was not observed. Hence, catalytic properties of the high temperature species that was formed (see TDS) cannot be compared to the silver O_γ species.

The reaction hysteresis occurred in the same temperature range in which the reduction of the copper oxide and the copper particle fractions was complete.

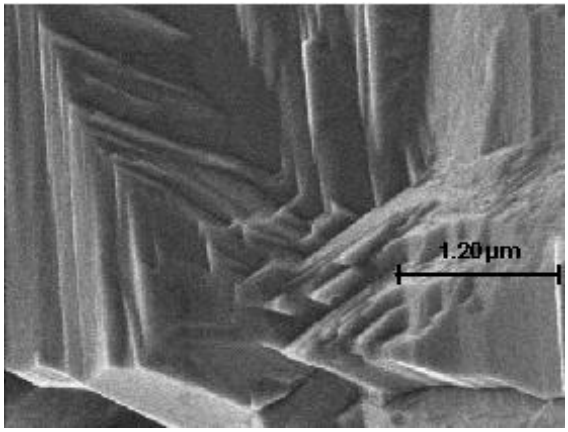

Graph.: 11-26 SEM of copper particles after OCM reaction. Faceted surface

Subsequent SEM/EDX analysis also proved the separation of the Cu-particles into cores and shells. The material showed highly facetted surfaces for the cores and shells for all tested particle sizes. The surface orientations were again determined to form Cu(111) planes in comparison to the obtained data after TDS and methanol oxidation reactions (Graph. 11-26).

The formation of carbonaceous material was found to take place in the voids between core and shell. After the steady state operation for 24h, the material was completely sintered to a copper block (Graph.11-27). The surface of the block showed a sponge-like appearance. The characterisation by SEM has proven that the morphological change, i.e. the pronounced sintering of the material,

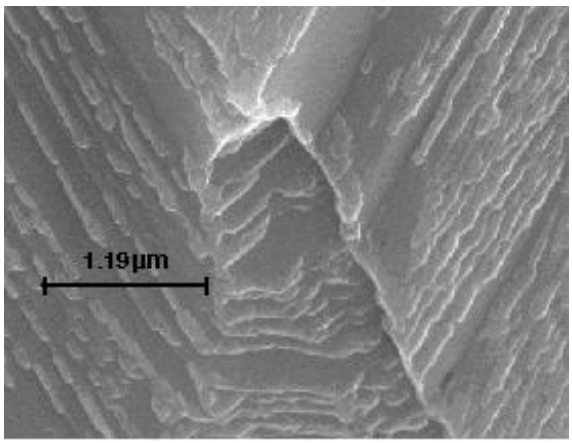

Graph.: 11-27 SEM of Copper particle after OCM long time experiment.

influenced mostly the catalytic activity. The sintering and the reduction of the active catalyst surface were responsible for the deactivation.

12 Summary

The general aspect of this work on copper catalysts is the identification of formation mechanisms of copper particles which can undergo various transformations under cyclic redox treatments.

The segregation of copper metal forced by redox processes at higher temperatures was used for the production of ceramic surfaces for several hundred years. Temperature and concentration of copper governed the morphological changes of the material. The formation of the spinel $CuAl_2O_4$ stabilised copper as Cu^{2+}. An increase of the reduction temperature led to the formation of highly dispersed copper particles on an inhomogeneous aluminate copper oxide matrix. The change of the copper oxidation state was responsible for the change of colour what is controlled by the change of the composition.

In addition, to the redox system of the spinel, some perovskite-type oxides were investigated. These materials prepared at high temperature are suggested to be catalysts for total oxidation as well as partial oxidation reactions. The controlled oxygen interaction by bulk diffusion caused by the “porosity” on the atomic level should be the reason for the catalytic properties. Copper is stabilised in these oxides in different oxidation states by structural properties. Several copper containing materials were tested for their catalytic activity in oxidation of alkenes and methanol. In contrast to to the published results the materials were all found to be unstable under catalytic reaction conditions. Partial oxidation products were not found. After catalytic action, the destruction of the perovskites to amorphous matrices containing copper metal particles was reveald.

The combination of copper and silver oxides together in one perovskite-type related compound was also tested for catalytic activity. $Ag_2Cu_2O_3$ was found to be not stable under catalytic reaction conditions but the formation of highly dispersed

copper and silver metal particles causes its activity for the methanol oxidation at temperature below 170°C. Spherical copper particles were found to be formed during the redox reaction or catalytic test reaction. If the structured copper oxide causes total oxidation and if the material was responsible for the nucleation of copper during the behaviour of copper metal particles should be able to explain the catalytic activity.

The redox behaviour of spherical copper particles of different diameters in comparison to oxide catalysts during selective partial oxidation reactions was investigated in this work. The results can be summarised in several aspects.

The morphological changes that the copper particles and the cuprates undergo during the methanol oxidation reaction or during other oxidation reaction are documented in Graph.: 12-1.

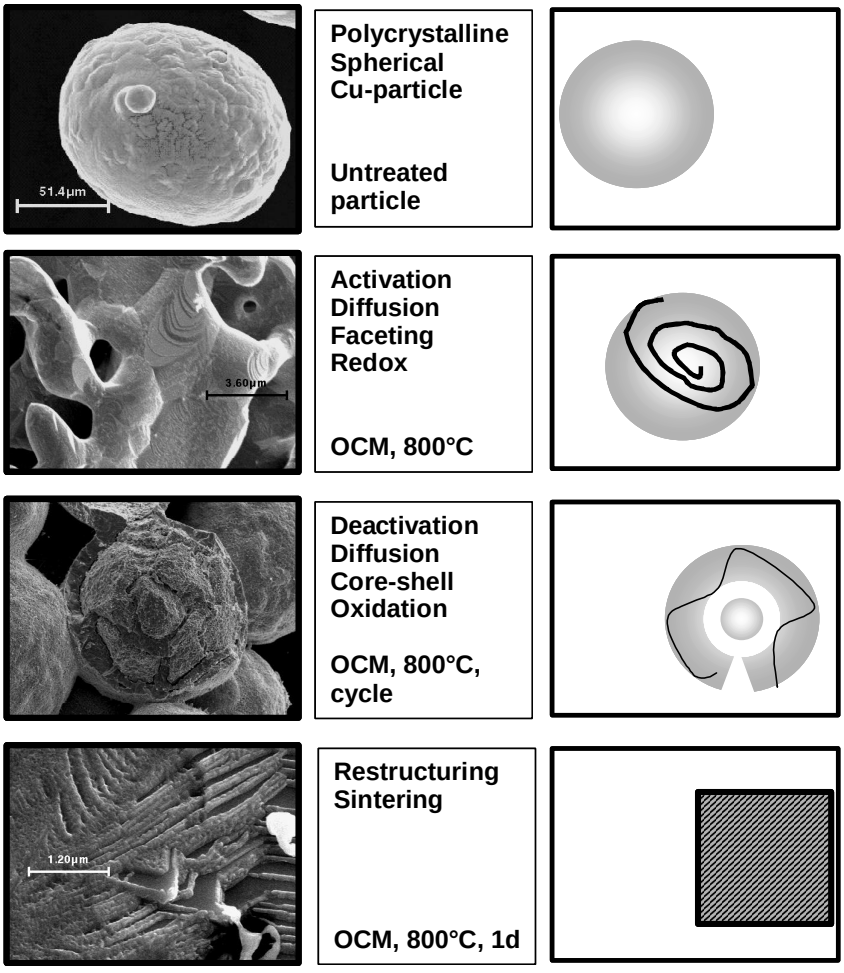

Graph.: 12-1 Change of morphology during partial oxidation reaction (OCM).

The untreated poly-crystalline spherical particle showed a macroscopic smooth, oxidised surface. During the activation in different reaction atmospheres the material is changed to a highly porous, highly facetted catalyst. This activation is forced by the diffusion of oxygen through the material and its interaction

with the surface. The influence of oxygen causes the faceting and the influence of the reactants causes the redox processes of material and gas phase. At this point the catalyst shows its highest activity The beginning of the deactivation of the catalyst is forced by the increase of sintering and partial oxidation of the metal. The extensive dissolution of oxygen in the particle surface leads to the formation of an oxide layer. This oxygen-rich shell coats an oxygen-poor core. The shell supports further sintering and a reduction of the macroscopic catalyst surface. The decrease of activity is forced by a further sintering what leads to a complete lost of the spherical particle shape but form a compact particle. The facets are covered by an oxygen-rich sponge like overlayer.

The interpretation of these morphological changes requires the application of several kinetic models. Each model is able to describe only one part of the complete transformation.

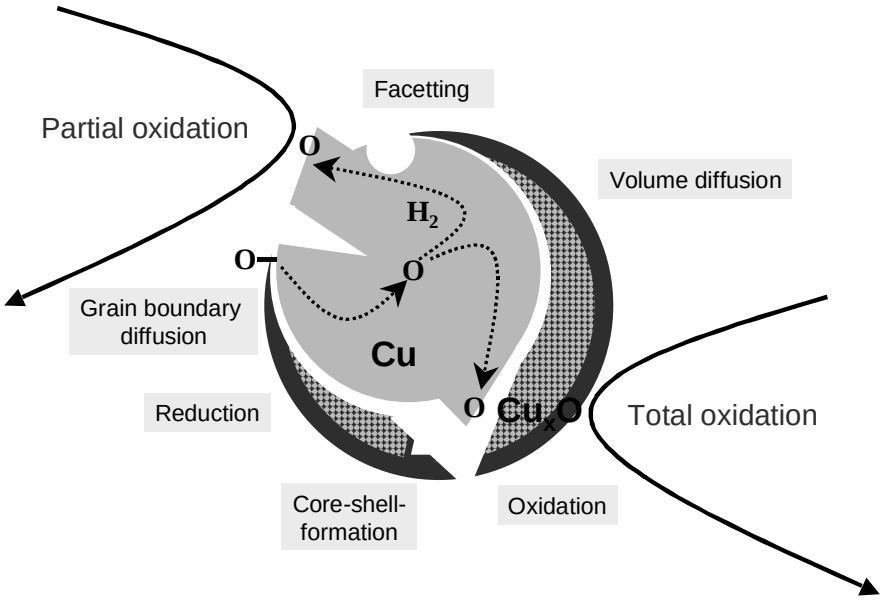

Graph.: 12-2 Copper model for selective partial oxidation reactions

The most "macroscopic" view that might be used is the interpretation by the Levenspiel model. The separation between a chemical reaction and a diffusion controlled reaction is achieved with this formalism. Sintering, core-shell formation, are the next steps, but thus are neglected by this model. The removal of the shell from the core can be describe by the Pilling Bedworth model. The influence of the stress to the particle surface region that is inflicted by the oxidation explaning the separation. The sintering of the material especially the shell with other particles shells documents indirectly that in this case not only an oxide, but an oxygen rich metallic species must have

been formed. The pressure-less sintering is described by the models of Naborro-Herring and Coble. If there are copper metal particles in an oxidic amorphous matrix, a nucleation controlled kinetic process might be the reason for that. Such kinetic is not taken into account by the Pilling-Bedworth model. The nucleation kinetics is described by the Avrami-Erofeev model. Oxidation reactions of metals are known as a surface controlled reactions. The formation of nuclei is as important for the catalytic activity as the their growth during the reaction. The formation of defined surface structures like Cu(111) planes is described by the re-crystallisation kinetics of Johnson-Mehl-Avrami-Kolmogorov very close to the more macroscopic Avrami-Erofeev nucleation. The description of this growth model at an atomic level might be the explanation of the whole life cycle of the catalyst. Unfortunately, the last step allows no more exception. With the JMAK-kinetics the atomic level was reached and the in situ detection of faceting is not possible, so far.

The main problem of all these models are the complications that arises if a real catalytic process is investigated. The complex interaction of a organic molecule together with oxygen on a amorphous catalyst inhibits a detailed kinetic analysis by macroscopic methods.

It is a fascinating aspect, that for copper particles in catalysis a correlation to surface science models is possible. The temperature-programmed experiment of the reduction of copper oxides showed that non-stoichiometric oxidic intermediates occur during the reaction. In the same temperature range copper showed its highest activity during the methanol oxidation. The oscillating behaviour during the methanol oxidation reaction emphasised the influence of the surface structure to activity. The SEM/EDX and EBSD investigations of this material proved the formation of nuclei and facets in the same way tat was found for copper foils under completely different reaction conditions. The faceting to Cu(111) planes and the occurrence of different oxygen species proved by temperature-programmed desorption built a strong relation to the results that were obtained for silver catalysts in partial oxidation reactions. It is now very likely that the diffusion of oxygen ad atoms to the subsurface region causes the beginning bulk oxidation and forms the catalytically active non-stoichiometric copper oxide. The completation of the oxidation built the oxidic shell around the metallic core gives rise to de-activation or under catalytic redox conditions leads to disintegration of the initial macroscopic particle.

The consequences of the work are:

1. Spherical copper particles undergo catalytically induced morphological changes during partial oxidation reactions.

2. These changes are faceting, core-shell formation, and sintering due to the redox reaction atmospheres far below the melting point of copper metal.

3. The occurrence of these phenomena can be correlated to the activation and desactivation of copper catalysts.

4. Cuprates like perowskite-type oxides, spinels, and $Ag_2Cu_2O_3$ are not stable under catalytic reaction conditions. The materials can be understood as a source for nanocrystalline copper particles.

5. Formation, Nucleation, sintering, and reconstruction of theses particles can be described by several kinetic models (Avrami-Erofeev, Pilling-Bedworth, Levenspiel).

6. The results obtained by catalytic test reactions can be confirmed by several reference experiments (TG/DTA, TDS, TPR)

7. The catalytic activity of cuprates is ruled by the same mechanisms that were found for copper metal .

13 Acknowledgements

Mein besonderer Dank gilt meinen Eltern und meiner Schwester, die mich während meines Studiums und der Promotion in allen Phasen bedingungslos unterstützt haben.

Ich möchte mich ausdrücklich bei Herrn Prof. Dr. R. Schlögl und Dr. G. Mestl für die stetige Unterstützung und ihre konstruktive Kritik an meiner Arbeit bedanken. Beides wurde umfangreich gewährt und hat zum Gelingen beigetragen. Besonders hervorheben möchte ich dabei nicht nur die fachliche Betreuung, sondern auch die Möglichkeit meine archäometrischen Forschungen fortführen zu dürfen. Neben sehr vielen interessanten Konferenzen hat ein Aufenthalt in Indien bei mir den größten Eindruck hinterlassen. Für die Möglichkeit dieser Reise möchte ich mich ebenfalls ausdrücklich bedanken.

Ohne den Einsatz und die Geduld von Frau Gisela Weinberg bezüglich der SEM Untersuchungen wäre diese Arbeit nicht möglich gewesen. Ihr und den Mitgliedern der Arbeitsgruppe „Heterogene Katalyse“, Martin Fait, Olga Ovsitser, Andreas Blume, Nadja Maximova, Raimund Horn, Manfred Thiede, Horst Brust, Olaf Timpe, Stefan Knobl, Pablo Beato, Steffen Fuhrmann, und allen anderen Mitgliedern der Abteilung Anorganische Chemie des FHI gilt mein Dank für die Unterstützung.

Zahlreiche Praktikanten haben mit mir zusammengearbeitet. Celine Elsäßer, Almut Rapp, Alexandra Scheffler, Esra Sule Azbanoglu, und Jennah Kriebel gehören dazu. Bei ihnen, wie auch bei Bernd Steinhauer, für seinen Einsatz im Rahmen seiner Diplomarbeit, möchte ich mich besonders bedanken.

Ich möchte mich ausdrücklich bei Frau Ute Röper für ihre Hilfe den Blick auf das Wesentliche zu richten bedanken.

Ich danke Ute Wild für die XPS/UPS-Messungen,

Norbert Pfänder für die TEM-Messungen,

Edith Kitzelmann für die XRD-Messungen,

Gisela Lorenz für die labortechnische Beratung

Franziska Krause für die Unterstützung bei den TPD/R/O- und TG/DTA-Messungen und

Karin Hofmann für die BET-Messungen.

Kooperationen müssen sich nicht nur auf fachliche Gebiete beschränken. Aus dem Alltag heraus haben sich viele Möglichkeiten ergeben, beim Badminton, Tennis, Kino, usw. die nicht-katalytische Seite des Anderen kennenzulernen. Das hat mir sehr geholfen.

Allen Mitarbeitern des Fritz-Haber-Institutes der Max-Planck-Gesellschaft, die keine namentliche Erwähnung gefunden haben sei an dieser Stelle ebenfalls gedankt.

14 Publications

H.-J. Wölk in: Catalysis from A to Z; B. Cornils, W.A. Herrmann, R. Schlögl, C.-H. Wang; Ed.- Weinheim, Wiley-VCH, 2000.

H.-J. Wölk, A.Scheffler, G. Mestl: Investigations on the selective partial oxidation of methanol and the oxidative coupling of methane on copper catalysts, Stud. Surf. Sci. Catal., 130 (2000) 3537.

M. Hartl, B. Spandl, H.-J. Wölk, P. Behrens, H. Hartl, R. Schlögl: XAFS-Investigations of CuO-based engobes – the system CuO-Al_2O_3-SiO_2 at temperatures from 850°C – 1150°C, HASYLAB Ann. Rep., 1 (2000).

H.-J. Wölk, G. Weinberg, G. Mestl, R. Schlögl: Investigations on the selective partial oxidation of methanol and the oxidative coupling of methane on copper catalysts, Stud. Surf. Sci. Catal., 133 (2001) 181.

H.-J. Wölk, B. Steinhauer, G. Weinberg, G. Mestl, R. Schlögl: Copper – Morphology and Selective Partial Oxidation, Chemie Ingenieur Technik 73 (2001) 666.

H.-J. Wölk, U. Wild, G. Weinberg, N. Pfänder, P. Gomez-Romero, G. Mestl, Inverstigations on the Catalytic Activity of the First Silver Copper Oxide: $Ag_2Cu_2O_3$, Chemie Ingenieur Technik 73 (2001) 667.

H.-J. Wölk, B. Hoffmann, G. Mestl, R. Schlögl: Experimental Archaeology: Investigations on the System Cu-Al-Si-O. J. Am. Ceram. Soc. accepted (2001).

H.-J. Wölk, G. Mestl, R. Schlögl: Catalytically induced nucleation of perovskite-type oxides. Catal. Lett. submitted (2001).

H.-J. Wölk, G. Weinberg, P. Gomez-Romero, G. Mestl, R. Schlögl: On the Catalytic Activity of the First Silver Copper Oxide: $Ag_2Cu_2O_3$. Chem. Eur. J. submitted (2001).

H.-J. Wölk, B. Steinhauer, J. Kriebel, G. Weinberg, G. Mestl, R. Schlögl: Morphological changes of copper catalysts in selective partial oxidations, J. Catal. subm. (2001).

H.-J. Wölk, J. Kriebel, G. Mestl, R. Schlögl: On the Properties of Copper in Selective Partial Oxidation Reactions. Talk. XXXIII. Jahrestagung deutscher Katalytiker, 22.-24.03.2000, Weimar.

H.-J. Wölk, G. Mestl: Investigations on Copper Catalysts. Talk. X. Workshop über die Charakterisierung von feinteiligen und porösen Feststoffen,15.-16.11.2000, Bad Soden.

H.-J. Wölk, U. Wild, G. Weinberg, N. Pfänder, P. Gomez-Romero, G. Mestl: Investigations of the Catalytic Activity of the first Silver Copper Oxide: $Ag_2Cu_2O_3$. Talk. 15th Indian National Symposium on Catalysis and 2nd Conference of the Indo-Pacific Catalysis Association, 23. - 25.01.2001, Pune, India.

H.-J. Wölk, G. Weinberg, R. Schlögl: Investigation of the selective partial oxidation of methanol and the oxidative coupling of methane over copper catalysts. Talk. 3rd International Symposium on Reaction kinetics and the development and operation of catalytic processes, 22.04. – 25.04.2001, Oostende, Belgium.

H.-J. Wölk, G. Mestl: Properties of copper as catalyst in selective oxidation reactions. Talk. 4th World Congress on Oxidation Catalysis, 16. –21.09.2001, Potsdam.

Curriculum Vitae

Name:	Hans.Jörg Wölk
Birthdate and Place:	January 19th 1970, Hamburg, Germany
School:	1980-1986, Luisen Gymnasium, Hamburg-Bergedorf 1986-1989, Gymnasium am Bornbrook, Hamburg-Lohbrügge
Military Service:	1989-1990, Hamburg, Germany
University:	1990- 1997, Freie Universität Berlin, Department of Chemistry, Department of the History of Arts
	Diploma Thesis: On the formation and characterization of pentafluoro-sulfanyl-isocyanide, F_5SNC; group of Dr. D. Lentz, Department of Inorganic and Analytic Chemistry,
	1997-2001, Fritz-Haber-Institute of the Max-Planck-Society, Berlin, Germany Thesis work. PhD to be received at the Technical University Berlin, Germany

15 References

[1] R. Schlögl, A. Knop-Gericke, M. Hävecker, T. Ressler, R.E. Jentoft, J. Wienold, G. Mestl, A. Blume, Y. Uchida, Topics Catal., 15 (2001) 219.

[2] J. Haber, E. Lalik, Catal. Today, 33 (1997) 119.

[3] G. Ertl, Phys. Bl., 46 (1990) 339.

[4] M.S. Spencer, Catal. Lett., 60 (1999) 45.

[5] M. Bowker, R.A. Hadden, H. Houghton, J.N.K. Hyland, K.C. Waugh, J. Catal., 109 (1988) 263.

[6] N. Takezawa, N. Iwasa, Catal. Today, 36 (1997) 45.

[7] O.V. Vodyankina, L.N. Kurina, G.A. Izatulina, L.A. Arkatova, Russ. J. Appl. Chem., 70 (1997) 1921.

[8] G. Reuss, W. Disteldorf, O. Grundler: Formaldehyde.-Ullmann's Encyclopedia of Industrial Chemistry, A11, p.619; Springer Ver. Berlin 1988.

[9] G. Sexto: Polyoxomethylenes.-Ullmann's Encyclopedia of Industrial Chemistry, A21, p.591; Springer. Berlin 1992.

[10] J.F. Walker: Formaldehyde. -Reinhold Publ. Cooperation; New York 1964.

[11] A.F. Hollemann, Lehrbuch der Anorganischen Chemie/ Hollemann-Wiberg, N. Wiberg, 101. Ed.- de Gruyter, Berlin 1995.

[12] S. Ashbrink, L. Norrby, Acta Crystallogr. B, 26 (1970) 8.

[13] J. Ghijsen, L.H. Tjeng, J. van Elp, H. Eskes, J. Westerink, G.A. Sawatzky, Phys. Rev. B, 38 (1988) 11322.

[14] P. Marksteiner, P. Blaha, K. Schwarz, Z. Phys. B: Condens. Matter, 64 (1986) 119.

[15] P.W. Baumeister, Phys. Rev., 121 (1961) 359.

[16] F.P Koffyberg, F.A. Benko, J. Appl. Phys., 53 (1982) 1173.

[17] G. Tammann, Z. Anorg. Allg. Chem., 111 (1928) 78.

[18] G. Tammann, F. Sartorius, Z. Anorg. Allg. Chem., 175 (1928) 97.

[19] R.F. Mehl, E.L. McCandless, F.N. Rhines, Nature, 182 (1934) 1009.

[20] P.A. Thiessen, H. Schütza, Z. Anorg. Allg. Chem., 233 (1937) 35.

[21] E. Menzel, Z. Anorg. Chem., 256 (1948) 49.

[22] E. Menzel, Ann. Phys., 5 (1949) 163.

[23] W.J. Tomlinson, J. Yates, J. Phys. Chem. Solids, 38 (1977) 1205.

[24] E. Menzel, Z. Phys., 132 (1952) 508.

[25] E. Menzel, W. Stössel, Chr. Menzel-Knopp, Z. Naturforsch., 12a (1957) 404.

[26] F.W. Young, J.V. Cathcart, A.T. Gwathmey, Acta Metall., 4 (1956) 145.

[27] J.C. Yang, B. Kolassa, J.M. Gibson, Appl. Phys. Letters, 73 (1998) 2841.

[28] J. Heller, W. Jaenicke, Ber. Bunsenges., 72 (1968) 1061.

[29] H. Neumeister, W. Jaenicke, Z. Phys. Chem., 108 (1977) 217.

[30] J. Xue, R. Diekmann, J. Phys. Chem. Solids, 51 (1990) 1263.

[31] M.J. Murray, J. Phys. Chem., 35 (1931) 1011.

[32] C. Carel, M. Mouallem-Bahout, J. Gaude, Solid State Ionics, 117 (1999) 47.

[33] M. Hävecker, A. Knop-Gericke, Th. Schedel-Niedrig, R. Schlögl, Angew. Chem., 110 (1998) 2049.

[34] Th. Schedel-Niedrig, Th. Neisius, I. Böttger, E. Kitzelmann, G. Weinberg, D. Demuth, R. Schlögl, Phys. Chem. Chem. Phys., 2 (2000) 2407.

[35] R. Vogel, W. Pocher, Z. Metallkunde, 21 (1929) 333.

[36] Gmelin-Institut, Handbuch der Anorganischen Chemie, Cu [B] 60, 23.

[37] W. Feldmann, Phys. Rev., 64 (1943) 113.

[38] A. Philips, E.N. Skinner, Am. Inst. Min. Met. Eng. Techn. Publ., 1280 (1941) 1.

[39] F.R. Rhines, C.H. Mathewson, Trans. A. Inst. Min. Met. Eng. Inst. Metals Div., 111 (1934) 337.

[40] X. Bao, M.Muhler, Th. Schedel-Niedrig, R. Schlögl, Phys. Rev. B, 54 (1996) 2249.

[41] G. Ertl, Surf. Sci., 173 (1967) 208.

[42] G.A. Somorjai, “Introduction to surface chemistry and catalysis.”John Wiley & Sons, U.S.A. 1993.

[43] A.F. Carley, P.R. Davies, G.U. Kulkarni, M.W. Roberts, Chem. Comm. 185, (2000) 186.

[44] F. Jensen, F. Besenbacher, E. Laengsgaard, I. Stensgaard, Phys. Rev. B-Cond. Mat. 41 (1990) 10233.

[45] A.F.Carley, P.R.Davies, R.V. Jones, K.R. Harikumar, G.U. Kulkarni, M.W. Roberts, Surf. Sci. 447 (2000) 39;50.

[46] N. Hartmann, R.J. Madix, Surf. Sci. 488 (2001) 107.

[47] S.M. Francis, R. Davies, N. Xiang, S. Haq, M. Bowker, F.M. Leibsle, Phys. Rev. Lett., 72 (1994) 2569.

[48] F.M. Leibsle, S. Haq, N. Xiang, M. Bowker, S.M. Francis, Surf. Sci., 315 (1994) 284.

[49] A.F. Carley, A.W. Owens, M.K. Rajumon, M.W. Roberts, Catal. Lett., 37 (1996).

[50] T. Fujitani, Y. Choi, M. Sano, Y. Kushida, J. Nakamura, J. Phys. Chem. B, 104 (2000) 1235.

[51] S.V. Gorshov, G.I. Lin, A.Ya. Rozovskii, Kin. Catal., 40 (1999) 334.

[52] F.M. Leibsle, Surf. Sci., 401 (1998) 153.

[53] P.R. Davies, G.G. Mariotti, Catal. Lett., 43 (1997) 261.

[54] M. Bowker, S. Poulston, R.A. Bennet, A.H. Jones, Catal. Lett., 43 (1997) 267.

[55] J.N. Russell, Jr., S.M. Gates, J.T. Yates, Jr., Surf. Sci., 163 (1985) 516.

[56] I. Wachs, R.J. Madix, J. Catal., 53 (1978) 208.

[57] J.N. Russel Jr., S.M. Gates, J.T. Yates Jr., Surf. Sci., 163 (1985) 516.

[58] M.A. Barteau, R.J. Madix, in The Chemical of Solid Surfaces and Heterogeneous Catalysts, ed. D.A. King and D.P. Woodruff.-Elsevier, Amsterdam 1982.

[59] M. Bowker, R,J. Madix, Surf. Sci., 102 (1981) 542.

[60] D.F. Cox, K.-H. Schulz, J. Vac. Sci. Technol., A8 (1990) 2599.

[61] P. Pitchai, K. Klier, Catal. Rev.-Sci. Eng., 28 (1986) 13.

[62] J. C. Mackie, Catal. Rev.-Sci. Eng., 33 (1991) 169.

[63] Z. Zhang, X. E. Verykios, M. Baerns, Catal. Rev.-Sci. Eng., 36 (1994) 507.

[64] D. Herein, A. Nagy, H. Schubert, G. Weinberg, E. Kitzelmann, R. Schlögl, Z. Phys. Chem., 197 (1996) 67.

[65] A. Nagy, Diss. TU Einhoven NL, 1999.

[66] J. C. Mackie, Catal. Rev.-Sci. Eng., 33 (1991) 169.

[67] Z. Zhang, X. E. Verykios, M. Baerns, Catal. Rev.-Sci. Eng., 36 (1994) 507.

[68] V.I. Vedeneev, O.V. Krylov, V.S. Arutynov, V.Ya. Basevich, M.Ya. Goldenberg, M.A. Teitel boim, Appl. Catal. A: General, 127 (1995) 51.

[69] L. Mleczko, M. Baerns, Fuel Proc. Tech., 42 (1995) 217.

[70] F.P. Fehlner, Phil. Mag. B, 52 (1985) 729.

[71] M.-S. Liao, Q.-E. Zhang, J. Mol. Catal., J. Mol. Catal. A: General, 136 (1998) 185.

[72] A. Palermo, J.P. Hodalgo Vasquez, R. M. Lambert, Catal. Lett., 68 (2000) 191.

[73] Y.K. Park, D.G. Vlachos, AIChE J., 43 (1997) 2083.

[74] G.A. Martin, C. Mirodatos, Fuel Proc. Tech., 42 (1995) 179.

[75] A. Nagy, Diss. TU Einhoven NL, 1999.

[76] H. Schubert, U. Tegtmeier, D. Herein, X. Bao, M. Muhler, R. Schlögl, Catal. Lett., 33 (1995) 305.

[77] R.J. Beuhler, R.M. Rao, J. Hrbeck, M.G. White, J. Phys. Chem. B, 105 (2001) 5950.

[78] A. Nagy, G. Mestl, Appl. Catal., 188 (1999) 337.

[79] M. Hävecker, PhD Thesis, Tecchnical University Berlin, 1999.

[80] I. Böttger, PhD Thesis, Freie Universität Berlin 1999.

[81] J.Y. Park, O. Levenspiel, Chem. Eng. Sci., 30 (1975) 1207.

[82] O. Levenspiel; Chemical Reaction Engeneering,2nd Ed.-Wiley, New York 1972.

[83] M. Ishida, C.Y. Wen, AIChE Journal, 14 (1968) 311.

[84] H. Rode, D. Orlicki, V. Hlavacek, AIChE Journal, 41 (1995) 1235.

[85] H. Rode, D. Orlicki, V. Hlavacek, AIChE Journal, 41 (1995) 2614.

[86] N.B. Pilling, R.E. Bedworth, J. Inst. Metals, 29 (1923) 529.

[87] H.L. Bernstein, Metall. Trans., 18A (1987) 975.

[88] D.M. Owen, T.G. Langdon, Mat. Sci. Eng., A216 (1996) 20.

[89] C. Herring, J. Appl. Phys., 21 (1959) 437.

[90] R.L. Coble, J. Appl. Phys., 34 (1963) 1679.

[91] T.E.M. Staab, R. Krause-Rehberg, B. Vetter, B. Kieback, J. Phys.: Condens. Matter, 11 (1999) 1757.

[92] W. Schatt: Sintervorgänge. 1st Ed.- VDI, Düsseldorf 1992.

[93] P. Wellner, G.H. Gessinger, H.-E. Exner, Z. Metallk., 65 (1974) 602.

[94] T.E.M. Staab, Diss. Universität Halle-Wittenberg, 1996.

[95] T.C. Wei, J.Phillips, Adv. Catal., 41 (1995) 359.

[96] M.R. Lyubovski, V.V. Barelko, J. Catal., 149 (1994) 23

[97] W.L. Winterbottom, J. Appl. Phys., 40 (1969) 3810.

[98] X. Bao, G. Lempfuhl, G. Weinberg, R. Schlögl, G. Ertl, J. Chem. Soc. Faraday Trans., 88 (1992) 865.

[99] M. Flytzani-Stephanopoulos, L.D. Schmidt, Prog. Surf. Sci., 9 (1979) 83.

[100] A.F. Bento, A.T. Gwathmey, J. Phys. Chem., 46 (1942) 969.

[101] H. Leidheiser, A.T. Gwathmey, J. Am. Chem. Soc., 70 (1948) 1200, 1206.

[102] T. Hwa, M. Kardar, M. Paczuski, Phys. Rev. Lett., 66 (1991) 441.

[103] C. Herring, Phys. Rev., 82 (1951) 87.

[104] N. Cabrera, Surf. Sci., 2 (1964) 320.

[105] W. Ostwald, Z. Phys. Chem., 22 (1897) 289.

[106] D. Kaschiev, K. Sato, J. Chem. Phys., 109 (1998) 8530.

[107] J.W. Christian, Physical Metallurgy, 2nd Ed..- R.W. Hahn, Amsterdam 1970.

[108] R.C. Lacmann, A. Herden, Chr. Mayer, Chem. Eng. Technol., 22 (1999) 4.

[109] A.N. Kolmogorov, Izv. Akad. Nauk SSSR, Ser. Mat., 1 (1937) 355.

[110] W.A. Johnson, R.F. Mehl, Trans. Am. Inst. Min. Metall. Eng., 135 (1939) 416.

[111] **M. Avrami, J. Chem. Phys., 9 (1941) 177.**

[112] **M. Fanfoni, M. Tomellini, Nuovo Ciem., 20D (1998) 1171.**

[113] **M.C. Weinberg, D.P.BirnieIII, V.A. Shneidman, J. Non-Cryst. Solids, 219 (1997) 89.**

[114] **C. DeW. Van Siclen, Phys. Rev. B: Condens. Matter, 54 (1996) 11845.**

[115] **D. Kashchiev, J. Chem. Phys., 104 (1996) 104.**

[116] **J.W. Cahn, Acta Metall., 4 (1956) 449.**

[117] **F. Baitalow, H.-G. Schmidt, G. Wolf, Thermochim. Acta, 337 (1999) 111.**

[118] **A.K. Galwey, M.E. Brown, Thermochim. Acta, 269/270 (1995) 1.**

[119] **A.K. Galwey, M.E. Brown, Thermochim. Acta, 300 (1997) 107.**

[120] **H. Schmalzried, Chemical Kinetics of Solids, VCh, Weinheim, 1995.**

[121] **M. Criado, M. Gonzales, A. Ortega, C. Real, J. Therm. Anal., 29 (1984) 243.**

[122] **J.P. Elder, J. Thermal Anal., 30 (1985) 657.**

[123] **H.E. Kissinger, Analyt. Chem., 29 (1957) 1703.**

[124] **H. Friedman, J. Polym. Sci. Part C, 6 (1964) 183.**

[125] **J.H. Flynn, L.A. Wall, J. Polym. Sci. PartB, 4 (1966) 323.**

[126] **T. Ozawa, Bull. Chem. Soc. Japn., 38 (1965) 1881.**

[127] **C.D. Doyle, J. Appl. Polymer Sci., 6 (1962) 639.**

[128] **J.H. Flynn, Thermochim. Acta, 300 (1997) 83.**

[129] **M. Avrami, J. Phys. Chem. 9 (1941) 177.**

[130] **J. Opfermann, E. Kaisersberger, Thermochim. Acta, 203 (1992) 167.**

[131] **J.R. Frade, M.Cable, J. Mat. Sci., 32 (1997) 2727.**

[132] **W. Jander, Z. Anorg. Allg. Chem., 163 (1927) 1.**

[133] **G. Valensi, C.R. Acad. Sci. Paris, 201 (1935) 602.**

[134] **A.M. Ginstling, V.I. Brounshtein, J. Appl. Chem. USSR, 23 (1950) 1327.**

[135] **M. Avrami, J. Chem. Phys., 7 (1939) 1103; 8 (1940) 212.**

[136] **B.V. Erofeev, in J.H. De Boer (Ed.), Reactivity of Solids., Proc. 4th Int. Symp. On Reactivity of Solids, pp. 273. Elsevier, Amsterdam, 1960.**

[137] **M.J. Starink, A.-M. Zahara, Thermochim. Acta, 292 (1997) 159.**

[138] **J. Malek, T. Mitsuhashi, J. Am. Ceram. Soc., 83 (2000) 2103.**

[139] **D. Rasch, G. Herrendörfer, J. Block, K. Busch: Verfahrensbibliothek-Versuchsplanung und –auswertung, VEB Deutscher Verlag Landwirtschaftsverlag Berlin, 1981.**

[140] K. Christman, Introduction to Surface Physical Chemistry, in Topics in Physical Chemistry Vol. 1, Ed.: H. Baumgärtel, E.U. Franck, W. Grünbein, Steinkopff-Verlag Darmstadt 1991.

[141] G. Ertl, Phys. Bl. 46 (1990) 339.

[142] J.W. Niemanntsverdriet, Spectroscopy in Catalysis, an introduction. 2nd Ed., Wiley-VCH 1993.

[143] P.J. Kisliuk, J. Phys. Chem. Solids, 3 (1957) 95.

[144] D.A. King, Surf. Sci., 47 (1975) 384.

[145] L. Reimer, G. Pfefferkorn: Raster-Elektronenmikroskopie. -2.Aufl. Springer Verlag, Berlin, 1977.

[146] D.P. Burke, R.L. Higginson, Scripta mater., 42 (2000) 277.

[147] N.C. Krieger Lassen, J. Microscopy, 181 (1996) 72.

[148] S. Amelinckx, D. van Dyck, J. van Landuyt, G. van Tendeloo: Handbook of Microscopy – Applications in Materials Science.- Part I. VCh, Weinheim, 1997.

[149] P.W. Atkins, Physikalische Chemie.- VCH, Weinheim, 1990.

[150] M.M. Günter, PhD Thesis, TU Berlin 2001.

[151] N.W. Hurst, S.J. Gentry, A. Jones, B. McNicol, Catal. Rev.-Sci. Eng., 24 (1982) 233.

[152] D.A. Monti, A. Baiker, J. Catal., 83 (1983) 323.

[153] P. Malet, A. Caballero, J. Chem. Soc.: Faraday Trans., 84 (1988) 2369.

[154] J.M. Criado, A. Ortega, F. Gotor, Thermocim. Acta, 157 (1990) 171.

[155] P. Malet, A. Caballero, J. Chem. Soc.: Faraday Trans., 84 (1988) 2369.

[156] A. Ortega, Thermochim. Acta, 298 (1997) 205.

[157] G. Fierro, M. LoJacono, M. Inversi, P. Porta, R. Lavechia, F. Cioci, J. Catal., 148 (1994) 709.

[158] M.J. Tiernan, P.A. Barnes, G.M.B. Parkes, J. Phys. Chem. B, 103 (1999) 338.

[159] K. Godlewski, A. Stoklosa, Thermal Anal., 1 (1974) 739.

[160] S. Walter, G. Frischmann, R. Broucek, M. Bergfeld, M. Liauw, Chem. Ing. Tech., 71 (2000) 447.

[161] O. Deutschmann, L.D. Schmidt, AIChE J., 44 (1998) 2465.

[162] D.J. Quiram, I.M. Sing, A. Franz, K.F. Jensen, M.A. Schmidt, Chem. Eng. Sci., 55 (2000) 3065.

[163] I. M. Sing, R. Srinivasan, M.P. Harold, K.F. Jensen, M.A. Schmidt, Chem. Eng. Sci., 55 (2000) 3.

[164] M. Baerns, H. Hofmann, A. Renken: Chemische Reaktionstechnik, Bd. 1.- 3.,drchges. Aufl..- Stuttgart: Thieme 1999.

[165] G.Centi, S. Perathoner, Appl. Catal. A,: General, 132 (1995) 179.

[166] F. Hamer, J. Hamer: Lexikon der Keramik und Toepferei: Material, Technik, Geschichte.- Augsburg; Augustus Verlag, 1990.

[167] W. Lehnhaeuser: Glasuren und ihre Farben. Duesseldorf 1966.

[168] A. Moropoulou, A. Bakolas, K. Bisbikou, Thermochim. Acta, 269/270 (1995) 743.

[169] H. Mommsen: Archaeometrie: neue naturwiss. Methoden u. Erfolge in d. Archaeologie.- Stuttgart; Teubner, 1986.-Teubner Studienbuecher.

[170] M.S. Tite, Proceed. Brit. Academy, 77 (1992) 111.

[171] P. Mirti, A. Casoli, L. Apollonia, Archaeometry, 35 (1993) 225.

[172] J. Riederer, Kunstwerke chemisch betrachtet: Materialien, Analysen, Altersbestimmung.- Berlin; Springer, 1981.

[173] T. Hausmann: Majolika: Spanische und italienische Keramik vom 14. Bis zum 18. Jh..- Katalog des Kunstgewerbemuseums Berlin.- Bd. 5, Gebr. Mann Verlag, Berlin 1986.

[174] R.A. Eppler, Ceramic Bull., 56 (1977) 213.

[175] F. Berti, G. Migliori, E. Dani, Tecnologica della ceramica antica: strumenti ditattici 1.- Museo archaeologico e della ceramica di Montelupo, 1989.

[176] H.H. Bachmann, H.P. Mielke, Ber. Dt. Keram. Ges., 55 (1978) 5.

[177] W. Noll, Alte Keramiken und ihre Pigmente: Studien zu Material und Technologie.- Stuttgart; E. Schweizerbart'sche Verlagsbuchhandlung (Nägele u. Obermiller), 1991.

[178] R.H.J. Clark, M.L.Curri, J. Mol. Struc., 440 (1998) 105.

[179] T.Y.A. Chan, M. Odlyha, Thermochim. Acta, 268/270 (1995) 755.

[180] L. Appolonia, Thermochim. Acta, 269/270 (1995) 769.

[181] F. Hund, Angew. Chem., 95 (1981) 763.

[182] A.I. Andrews, C.H. Zwermann, J. Am. Ceram. Soc., 22 (1939) 65.

[183] Martin Heinrich Klapproth, 1743-1817, first Prof. for chemistry of the university of Berlin, founded the archaeometric section.

[184] C. Picolpasso: Li tre libri dell'arte del vasaio, ed. a. transl. By B. Rackham, 1934.

[185] A.F. Hollemann: Lehrbuch der Anorganischen Chemie / Hollemann-Wiberg.- 101. Auflg.- Berlin: de Gruyter, 1995.

[186] S. Singer, Ceram Ind., 63 (1951) 72.

[187] R.J. Gettens, E.W. Fitzhugh, Conservation, 19 (1974) 2.

[188] **W. Noll, R. Holm, L. Born, Angew. Chem., 18 (1975) 639.**

[189] **W. Noll, K. Hangst, N. Jb. Miner. Mh., (1975) 209.**

[190] **E.M. Jope, C. Huse, Nature, 144 (1940) 26.**

[191] **R.J. Forbes, Studies in ancient technology. Chap. 7, vol. 3, p. 210, 1965.**

[192] **H.G. Wiedemann, G. Bayer, Analytical Chem., 54 (1982) 619.**

[193] **W. Noll, R. Holm, L. Born, N. Jb. Miner. Abh., 122 (1974) 119.**

[194] **I. Bauer, W.Endres, B. Kerkhoff-Hader, R. Koch, H.-G. Stephan: Leitfaden zur Keramikbeschreibung; Mittelalter – Neuzeit.- Praehistorische Staatssammlung Muenchen.- Kallmuenz/Opf.;V. M. Lassleben, 1993.**

[195] **Autorenkollektiv: Technologie der Feinkeramik.-Leipzig, VEB Verlag fuer Grundstoffindustrie, 1979.**

[196] **W. Gebauer: Kunsthandwerkliche Keramik.- Friesen, J. Buechel, 1981.**

[197] **T. Haase: Keramik.- Leipzig, VEB Verlag fuer Grundstofftechnik, 1970.**

[198] **B. Hoffmann, A. Vernhet, RCRF, XXXI-XXXII (1992) 177.**

[199] **B. Hoffmann, M Picon, Ann. Pegasus, 1 (1993) 3.**

[200] **U. Hofmann, Angew. Chem., 80 (1968) 736.**

[201] **C. Nicolescu-Otin, Met., 9 (1912) 92.**

[202] **N.W. Taylor, Z. Phys. Chem., B9 (1930) 241.**

[203] **W. Noll, Angew. Chem., 75 (1963) 123.**

[204] **J.A. Hedvall, J. Heuberger, Z. Anorg. Chem., 116 (1921) 137.**

[205] **ASTM card 2-1414.**

[206] **O. Krause, Ber. Dt. Keram. Ges., 15 (1934) 101.**

[207] **T. Tsuchida, R. Furuichi, T. Sukegawa, M. Furudate, T. Ishii, Thermochim. Acta, 78, (1984) 71.**

[208] **ASTM card 9-185.**

[209] **A.M.M. Gadalla, J. White, Trans. Brit. Ceram. Soc., 63 (1964) 39.**

[210] **S. Misra, A.C.D. Chaklader, J. Am. Ceram. Soc., 46 (1963) 509.**

[211] **E. Thompson, J.G. Thompson, R.L. Whiters, M. Sterns, Y. Xiao, R.J. Kirkpatrick, J. Am. Ceram. Soc., 77 (1994) 49.**

[212] **K.T. Jacob, C.B. Alcock, J. Am. Ceram. Soc., 58 (1975) 192.**

[213] **R. Vogel, W. Pocher, Z. Metallkunde, 21 (1929) 333.**

[214] **Gmelin Institut: Handbuch der Anorganischen Chemie. Cu [B] 60, 23.**

[215] **A.M.M. Gadalla, W.F. Ford, J. White, Trans. Brit. Ceram. Soc., 62 (1963) 45.**

[216] **H.S. Roberts, F.H. Smyth, J. Am. Soc. 43 (1921) 1061.**

[217] **C.Y. Chen, G.S. Lan, W.H. Tuan, J. European Ceram. Soc., 20 (2000) 2519.**

[218] **A. K. Chakraborty, D.K. Ghosh, J. Am. Ceram. Soc., 61 (1978) 170.**

[219] **M Slaughter, W.D. Keller, Am. Ceram. Soc. Bull., 38 (1959) 703.**

[220] **In Ullmanns Encyclopaedia of techn. Chemistry, 4. Aufl., 1977.**

[221] **Collection of the Kunstgewerbemuseum Berlin, Saatliche Museen Preussischer Kulturbesitz (SMPK), Kulturforum, Matthaeikirchplatz.**

[222] **Naturwissenschaftliche Kriterien und Verfahren zur Beschreibung von Keramik, Diskussionsergebnisse der Projektgruppe Keramik im AK Archäometrie (G. Schneider Ed.), Acta Praehistorica et Archaeologica 21 (1989).**

[223] **F. Berti: The Montelupo Ceramics, from thw 16th to 18th centuries. –Electa, Milano 1986.**

[224] **K.J.D. MacKenzie, J. appl. Chem., 19 (1969) 65.**

[225] **Ph. Colomban, J. Mat. Sci., 24 (1989) 3002.**

[226] **Ph. Colomban, J. Mat. Sci., 24 (1989) 3011.**

[227] **B.D. Saksena, Trans. Farad. Soc., 57 (1961) 242.**

[228] **H.J. Percival, J.F. Duncan, P.K. Forster, J. Am Ceram. Soc., 57 (1974) 57.**

[229] **R.D. Walderon, Phys. Rev., 99 (1955) 1727.**

[230] **S. Hafner, Z. Krist., 115 (1961) 331.**

[231] **W.B. White, B.A. DeAngelis, Spectrochim. Acta, 23A (1967) 985.**

[232] **L.M. Plyasova, T.M. Yur'eva, I. Yu. Molina, T.A. Krieger, A.M. Balagurov, L.P. Davydova, V.I. Zaikovskii, G.N. Kustova, V.V. Malakhov, L.S. Dovlitova, Kin. Catal., 41 (2000) 429.**

[233] **B. Jalala Kumari, P. Krishna Pillari, K.G.K. Warrier, K.G. Satyanarayna, J. Mat. Sci. Lett., 5 (1986) 865.**

[234] **F. Bergaya, P. Dion, J.-F. Alcover, C. Clinard, D. Tchoubar, J. Mat. Sci., 31 (1996) 5069.**

[235] **M. Lo Jacono, M. Schiavello, A. Chimino, J. Phys. Chem., 75 (1971) 1045.**

[236] **G. Ertl, R. Hierl, H. Knözinger, N. Thiele, H.P. Urbach, App. Surf. Sci., 5 (1980) 49.**

[237] **R.M. Friedman, J.L. Freeman, J. Catal., 55 (1978) 10.**

[238] **J.P. Malins, K.H. Tonge, Thermochim. Acta, 340-341, (2001) 395.**

[239] **R.J.H.Voorhoeve, J.J. Burton, R.L. Garten (Eds.) Adv. Mater. in Catalysis, Academic Press, NY, 1997, p. 129.**

[240] **T. Seiyama, Catal. Rev.-Sci. Eng. ,** ***34*** **(1994) 281.**

[241] **L.G.Tejuca, J.L.G.Fierro, J.M.D.Tascon, in D.D.Eley, H.Pines and P.B.Weisz (Eds.) Adv. Catal. *36*, (1989) 237.**

[242] **G. Saracco, G. Scibilia, A. Iannibello, G. Baldi, Appl. Catal. B, *8*, (1996) 229.**

[243] **R.J. Cava, Science, 247 (1990) 656.**

[244] **F. Liebau, Angew. Chem., 111 (1999) 1845.**

[245] **G. Demazeau, C. Parent, M. Prouchard, P. Hagenmüller, Mat. Res. Bull., 7 (1972) 913.**

[246] **Y. Miyazaki, N. Hyatt, M. Slaski, I. Gameson, P.P. Edwards, Chem. Eur. J., 5 (1999) 2265.**

[247] **S. Maekawa, Sience, 273 (1996) 1515.**

[248] **S.N. Ruddlesden, P. Popper, Acta. Cryst., 11 (1958) 54.**

[249] **B. Grande, H. Müller-Buschbaum, M. Schweizer, Z. Anorg. Allg. Chem., 428 (1977) 120.**

[250] **K. Otzschi, Y. Ueda, Tech. Report ISSP, 3254 (1997) 1.**

[251] **F. Ribot, S. Kratovhil, E. Matijevic, J. Mater. Res., 4 (1989) 1123.**

[252] **C. Rial, E. Moran, M.A. Alario-Franco, U. Amador, N.H. Andersen, Physica C, 254 (1995) 233.**

[253] **W. Günter, W. Paulus, R. Schöllhorn, Physica C, 132 (1999) 61.**

[254] **R.J. Cava, B. Batlogg, C.H. Chen, E.A. Rietman, S.M. Zahurak, D. Werder, Phys. Rev. B, 36 (1987) 5719.**

[255] **S. Yu. Glazkov, L.V. Glazkova, Z.I. Semenova, N.F. Zakharchuk, Thermochim. Acta, 342 (1999) 147.**

[256] **E. Goldberg, A. Nemudry, V. Boldyrev, R. Schöllhorn, Solid State Ionics, 110 (1998) 223-233.**

[257] **S. Adler, S. Russek, J. Reimer, M. Fendorf, A. Stacy, Q. Huang, A. Santoro, J. Lynn, J. Baltisberger, U. Werner, Solid State Ionics, 68, (1994), 193-211.**

[258] **S. Wei, F. Liu, S. Cao, J. Zhang, Mat. Lett., 35, (1998), 270.**

[259] **R. Gottschall, R. Schöllhorn, M. Muhler, N. Jansen, D. Walcher, P. Gütlich, Inorg. Chem., 37, (1998), 1513-1518.**

[260] **J.F. Howlett, W.R. Flavell, A.G. Thomas, J. Hollingworth, S. Warren, Z. Hashim, M. Mian, S. Squire, H.R. Aghabozorg, Md. Moinuddin Sarker, P. Wincott, D. Techan, S. Downes, D. S.-L. Law, F.E. Hancock, Faraday Discuss., 105, (1996), 337-354.**

[261] **Z. Yu, L. Ghao, S. Xuan, Y. Wu, J. Chem. Soc. Faraday Trans., 88, (1992), 3245.**

[262] **Th. Koslowski, Phys. Chem. Chem. Phys., 1, (1999), 3017-3023.**

[263] **M. T. Anderson, J.T. Vaughey, K.R. Poeppelmeier, Chem. Mater., 5, (1993), 151-165.**

[264] **J.-C. Grennier, N. Ea, M Prouchard, P. Hagenmüller, Solid State Chem., 58, (1985), 243.**

[265] **A. Nemudry, P. Rudolf, R. Schöllhorn, Chem. Mater., 8, (1996), 2232-2238.**

[266] **A. Nemudry, P. Rudolf, R. Schöllhorn, Solid State Ionics, 109, (1998), 213-222.**

[267] **J.B. Goodenough, A. Manthiram, P.Paranthaman, Y.S. Zhen, Solid State Ionics, 5, (1992), 105.**

[268] **A. Manthiram, J.S. Swinnea, Z.T. Sui, H. Steinfink,, J.B. Goodenough, J. Am. Chem. Soc., 109, (1987), 6667.**

[269] **A. Nemudry, M. Weiss, I. Gainutdinov, V. Boldyrev, R. Schöllhorn, Chem. Mater., 10, (1998), 2403.**

[270] **S.-J. Huang, A.B. Walters, M.A. Vannice, Appl. Catal. B, 17, (1998), 183.**

[271] **V.V. Kharton, L. Shuangbao, A.V. Kovalevsky, A.P. Viskup, E.N. Naumovich, A.A. Tonoyan, Mat. Chem. Phys., 53, (1998), 6-12.**

[272] **K.D. Kreuer, W. Münch, U. Traub, J. Maier, Ber. Bunsenges. Phys. Chem., 102, (1998), 552-559.**

[273] **D. Klissurski, V. Rives, Appl. Catal. A, 109, (1994), 1-44.**

[274] **M. Caldararu, A. Oventson, J.R. Walls, Appl. Catal. A, 167, (1998), 225-235.**

[275] **T. Yosikawa, M. Bowker, Phys. Chem. Chem. Phys., 1, (1999), 913-920.**

[276] **K. Klier, A. Beretta, Q. Sun, O.F. Feeley, R. G. Herman, Catal. Today, 36, (1997), 3-14.**

[277] **G.K. Boreskov, in D.D. Eley, H. Pines, and P.B. Weisz (Ed.), Advances in Catalysis, Academic Press, Vol. 1, p. 477.**

[278] **G.K Boreskov, in J.R. Anderson and M. Boudart (Ed.), Catalysis, Science and Technology, Springer-Verlag, Berlin, Vol. 3, 1982, p. 39.**

[279] **R. Jeyalakshmi, B. Jagannadhaswamy, K. Rengaraj, B. Sivasankar,, Bull. Chem. Soc. Jpn., 63, (1990), 2970-2974.**

[280] **P.N. Trikalitis, P.J. Pomonis, Appl. Catal. A, 131, (1995), 309.**

[281] **A. Jiang, Y. Peng, Q. Zhou, Gao, P., H.Yuan, J. Deng, Catal. Lett., 3, (1989), 235-246.**

[282] **I. J. Pickering, J.M. Thomas, J. Chem. Soc. Faraday Trans., 87, (1991), 3067-3075.**

[283] **J. Shu, S. Kaliaguine, Appl. Catal. B, 16, (1998), L303.**

[284] **V.S. Arutyunov, V.Ya. Basevich, V.I. Vedeneev, O.V. Krylov, Kin. Catal., 40, (1999), 382-387.**

[285] **C.T. Au, K.D. Chen, C.F. Ng, Appl. Catal. A, 171, (1998), 283.**

[286] **A. Kaddouri, R. Kieffer, A. Kiennemann, Catal. Lett., (1989), .**

[287] **U. Balachandaran, J.T. Dusek, P.S. Maiya, B. Ma, R.L. Mielville, M.S. Kleefisch, C.A. Udovich, Catal. Today, 36, (1997), 265.**

[288] **A.A. Davydoy, M.L. Shepotko, A.A. Budneva, Catal. Today, 24, (1995), 225.**

[289] **D. Ferri, L. Forni, Appl. Catal. B, 16, (1998), 119.**

[290] **Y.S. Lin, Y. Zeng, J. Catal., 164, (1996), 220.**

[291] **L. Marchetti, L. Forni, Appl. Catal. B, 15, (1998), 179.**

[292] **P. Tsiakaras, C. Anthanasiou, G. Mornellos, M. Stoukides, J.E. ten Elshof, H.J.M. Bouwemeester, Appl. Catal A, 169, (1998), 249.**

[293] **M. Teymouri, E. Bagherzadeh, J. Mat. Sci., 30, (1995), 3005.**

[294] **P. Gaffuri, T. Faravelli, E. Ranzi, N. Chernansky, D. Miller, A. d'Anna, A. Ciajolo, AIChE Journal, 43, (1997), 1278-1286.**

[295] **L. Guzci, R. van Santen, K.V. Sarma, Catal. Rev.-Sci. Eng., 38, (1996), 249-296.**

[296] **V.C. Belessi, C.N. Costa, T.V. Bakas, T. Anastasiadou, P.J. Pomonis, A.M. Efstathiou, Catal. Today, 59, (2000), 347-363.**

[297] **J. Christopher, C.S. Swamy, J. Mol. Catal., 62, (1990), 69-78.**

[298] **Y. Yokoi, H. Ushida, Catal. Today, 42, (1998), 167-174.**

[299] **D. Ferri, L. Forni, M.A.P. Dekkers, B.E. Niewenhuys, Appl. Catal. B, 16, (1998), 339.**

[300] **L. Forni, C. Olivera, F. P. Vatti, N. A. Sinitsina, S.V. Sorochkin, A.V. Moev, A.V. Vishniakov, J. Chem. Soc. Faraday Trans., 88 (1992) 1041.**

[301] **N. Gunasekaran, S. Rajadurai, J.J. Carberry, Catal. Lett., 35, (1995),373.**

[302] **N. Guilhaume, S.D. Peter, M. Primet, Appl. Catal B, 10 (1996) 325.**

[303] **H. Hamada, Catal. Today, 22 (1994) 21.**

[304] **D. Klvana, J. Chadouki, C. Guy, J. Kirchnerova, Combust. Sci. And Tech., 121 (1996) 51.**

[305] **K.V. Ramanujachary, N. Kameswari, C.S. Swamy, J. Catal., 86, (1984), 121.**

[306] **C.S. Swamy, J. Christopher, Catal. Rev.-Sci. Eng., 34 (1992) 409.**

[307] **S. Subramanian, C.S. Swamy, Catal. Lett., 35 (1995) 361.**

[308] **L.A. Pedersen, W.F. Libby, Science, 176 (1972) 1355.**

[309] **E.A. Lombardo, M.A. Ulla, Res. Chem. Intermed., 24 (1998) 581.**

[310] **H. Arai, T. Yamada, K. Eguchi, T. Seiyama, Appl. Catal., 26 (1986) 265.**

[311] **T. Nitadori, T. Ichiki, M. Misono, Bull. Chem. Soc. Japan, 61 (1988) 621.**

[312] **G.E. Keller, M.M. Bhasin, J. Catal., 73 (1982) 9.**

[313] V.D. Sokolovskii, N.J. Coville, A. Parmaliana, I. Eskendirov, M. Makoa, Catal. Today, 42 (1998) 191.

[314] T. Ito, J.-X. Wang, C.-H. Lin, J.H. Lunsford, J. Am. Chem. Soc., 107 (1985) 5062.

[315] C.-H. Lin, K.D. Campell, J.-X. Wang, J.H. Lunsford, J. Phys. Chem., 90 (1986) 534.

[316] K.D. Campell, H. Zhang, J.H. Lunsford, J. Phys. Chem., 92 (1988) 750.

[317] M. O'Connell, A.K. Norman, C.F. Hüttermann, M.A. Morris, Catal. Today, 47 (1999) 123.

[318] C. T. Au, Y.H. Hu, H.L. Wen, Catal. Lett., 36 (1996) 159.

[319] I. Lee, K.Y.S. Ng, Catal Lett., 2 (1989) 403.

[320] O.V. Krylov, Catal. Today, 18 (1993) 209.

[321] A. Ekstrom, J.A. Lapszewicz, J. Chem. Soc., Chem. Comm., 797-799, (1998).

[322] Z. Zhang, X.E. Verykios, M Baerns, Catal. Rev.-Sci. Eng., 36 (1994) 507.

[323] E.A. Gregoryan, Kin. Catal., 40 (1999), 389.

[324] R.J.H.Voorhoeve, J.J. Burton, R.L. Garten (Eds.) Adv. Mater.-in Catalysis, Academic Press, NY, 1997, p. 129.

[325] MM. Bettahar, G. Costentin, L Savary, J.C. Lavalley, Appl. Catal. A, 145 (1996) 1.

[326] C.R. Adams, T.J. Jennings, J. Catal., 25, (1964), 549.

[327] V.G. Michalchenko, V.D. Sokolowskii, A.A. Filippova, A.A. Davydov, Kinet. Katal., 14, (1973), 1253.

[328] B.J. Wood, H. Wise, R.S. Yolles, J. Catal., 15 (1969) 355.

[329] I. Rodriguez-Ramos, A. Guerrero-Ruiz, M.L. Rojas, J.L.G. Fierro, Appl. Catal., 68 (1991) 217.

[330] I. Halasz, Appl. Catal., 47, (1989), L17-22.

[331] J.R. Johnson, M. Suenage, P. Thompson, J.J. Reilly, Z. Phys. Chem., 163, (1989), 721.

[333] W. Günter, R. Schöllhorn, Solid State Ionics, 101-103, (1997), 1335.

[334] J. Hauck, B. Bischof, K. Mika, E. Janning, H. Libutzki, J. Plewa, Physica C, 212 (1993) 435.

[335] H. Lütgemeier, S. Schmenn, Yu. Baikov, Solid State Comm., 94, (1995), 283.

[336] M.F. Yan, R.L. Barns, H.M. O'Bryan, Jr., P.K. Gallgher, R.C. Sherwood, S.Jin, Appl. Phys. Lett., 51 (1987) 532.

[337] W. Günter, R. Schöllhorn, H. Siegle, C. Thomsen, Solid State Ionics, 84, (1996), 23.

[338] W. Günter, R. Schöllhorn, Physica C, 271, (1996), 241.

[339] P. Fortunato, A. Reller, H.R. Oswald, Solid State Ionics, 101-103 (1997) 85.

[340] **E. Traversa, P. Nunziante, M Sakamoto, Y. Sadaoka, R. Montanari, Mat. Res. Bull., 33 (1998) 673.**

[341] **L.G. Tejuca, J.L.G. Fierro, Adv. Catal., 36 (1989) 237.**

[342] **W. Günther, Dissertation, TU Berlin, (1994).**

[343] **G.M.B. Parkes, P.A. Barnes, E.L. Charsley; M Reading; I. Abrahams, Thermochim. Acta 354 (2000) 39.**

[344] **S.Vyazovkin, C.A. Wight, Ann. Rev. Phys. Chem. 48 (1997) 125.**

[345] **F. Jensen, F. Besenbacher, E. Laengsgaard, I. Stensgaard, Surf. Sci. Lett., 259 (1991) L774.**

[346] **L.H. Dubois, Surf. Sci., 119 (1982) 399.**

[347] **A. Spitzer, H. Lüth, Surf. Sci., 118 (1983) 136.**

[348] **D.L. Gocke, G.K. Chua, N. Kruse, J.H. Block, Appl. Surf. Sci., 84 (1995) 153.**

[349] **F. Groenlund, P.E. Hoelund Nielsen, Surf. Sci., 30 (1970) 388.**

[350] **L.A. Aratova, L.N. Kurina, O.V. Vodyankina, A.G. Kozhomin, Russ. J. Appl. Chem., 72 (1999) 639.**

[351] **R.A. Hadden, B. Sakakini, J. Tabatabai, K.C. Waugh, Catal. Letters, 44 (1997) 145.**

[352] **C. Barnes, P. Pudney, Q. Guo, M. Bowker, J. Chem. Soc. Faraday Trans., 86 (1990) 2693.**

[353] **M. Bowker, R.J. Madix, Surf. Sci., 95 (1980) 190.**

[354] **M Casarin, G. Granozzi, M. Sambi, E. Tondello, A. Vittadini, Surf. Sci., 307, (1994) 95.**

[355] **P. W. Jacobs, G. A. Somorjai, J. Mol. Catal. A, 131, (1998), 5-18.**

[356] **F. Illas, M. Bachs, J. Rubio, J.M. Ricart, J. Chem. Phys., 91 (1989) 5466.**

[357] **Th. Schedel-Niedrig, Th. Neisius, E. Kitzelmann, G. Weinberg, D. Demuth, R. Schlögl, Phys. Chem. Chem. Phys., 2, (2000), 2407.**

[358] **T.-C. Wei, J. Phillips, Adv. Catal., 41 (1998) 332.**

[359] **M.M. Bhasin, Catal. Letters, 59 (1999) 1.**

[360] **P. Gomez-Romero, E. M. Tejada-Rosales, M.R. Palacin, Angew. Chem., 111, (1999), 544.**

[361] **K. Adelsberger, J. Curda, S. Vensky, M. Jansen, J. Solid State Chem., 158 (2001) 82.**

[362] **A.J. Nagy, G. Mestl, Th. Rühle, G. Weinberg, R. Schlögl, J. Catal., 179 (1998) 548.**

[363] **D. Zemlyanov, A.J. Nagy, R. Schlögl, Appl. Surf. Sci., 133 (1998) 171.**

[364] **H.-J. Wölk, G. Weinberg, G. Mestl, R. Schloegl to be published.**

[365] **S. Ashbrink, L. Norrby, Acta Crystallogr. B, 26, (1970), 8.**

[366] P. Marksteiner, P. Blaha, K. Schwarz, Z. Phys. B: Condens. Matter, 64 (1986) 119.

[367] A. Deb, A.K. Chatterjee, J. Phys.: Condens. Matter, 10 (1998)11719.

[368] D. Klissurski, V. Rives, Appl. Catal. A, 109 (1994) 1.

[369] J.-H. Park, P.M. Woodward, J.B. Parise, Chem. Mater., 10 (1998), 3092.

[370] L.G. Tejuca, J.L.G. Fierro, Adv. Catal., 36 (1989) 237.

[371] W. Günther, R. Schöllhorn, Solid State Ionics, 101-103 (1997) 1335.

[372] S.J. Xu, W.J. Thomson, AIChE Journal, , 43, (1997) 2731.

[373] S. Cimino, L. Lisi, R. Pirone, G. Russo, M. Turco, Catal Today, 59 (2000) 19.

[374] D. Majumdar, H.D. Glicksman, T.T Kodas, Powder Technology, 110 (2000) 76.

[375] Z. Chajar, M. Primet, H. Praliaud, M. Chevrier, C. Gauthier, F. Mathis, Catal. Letters, 28 (1994) 33.

[376] G. Centi, S. Perathoner, Appl. Catal. A, 132 (1995) 179.

[377] T. Izuka, H. Ikeda, S. Okazaki, J. Chem. Soc. Faraday Trans., 61 (1986) 82.

[378] F.W. Telgheder, J. Urban, J. Eletron Spec. Rel. Phen., 95 (1998) 267.

[379] I. Lisecki, A. Filankembo, H. Sack-Kongehl, K. Weiss, M.P. Pileni, J. Urban, Phys. Rev. B, 61 (2000) 4968.

[380] H.-J. Wölk, G. Weinberg, G. Mestl, R. Schlögl, Stud. Surf. Sci. Catal., 130 (2000) 3537.

[381] J. Find, Diss. TU Berlin 1998.

[382] S. Vyazovkin, C.A. Wight, Annu. Rev. Phys. Chem., 48 (1997) 125.

[383] J. Opfermann: Thermokinetics.- Netzsch-Gerätebau GmbH, D-95100 Selb.

[384] H.-J. Wölk, U. Wild, G. Weinberg, G. Mestl, R. Schlögl, Stud. Surf. Sci. Catal., 133 (2001) 181.

[385] Y. Iijima, N. Niimura, K.Hiraoka, Surf. Interface. Anal., 24 (1996) 193.

[386] J. Ghijsen, L.H. Tjeng, J. van Elp, H. Eskes, J. Westerink, G.A. Sawatzky, Phys. Rev. B, 38 (1988) 11322.

[387] S. Hüfner, G.K. Wertheim, J.H. Wernick, Solid State Commun., 17, (1975), 417.

[388] L.H. Tjeng, M.B.J. Meinders, J. van Elp, J. Ghijsen, G.A. Sawatzky, Phys. Rev. B, 41 (1990) 3190.

[389] P.G. Dickens, R. Heckingbottom, J.W. Linnett, Trans. Faraday Soc., 65 (1969) 2235.

[390] T. Robert, M. Bartel, G. Offergeld, Surf. Sci., 33 (1972) 123.

[391] H.-J. Wölk, G. Mestl, U. Wild, R. Schlögl, subm. Adv. Mat. (2002).

[392] Sciplot, software for data manipulation, M. Wesemann, FHI-MPG Berlin

[393] Program for kinetic analysis, J. Opfermann, Netzsch Inc., Selb

[394] **based in parts on the Diplomathesis of B. Steinhauer, TU Berlin (2000).**

[395] **A.N. Gokarn, L.K. Doraswamy, Chem. Eng. Sci., 26 (1971) 1521.**

[396] **H.J. Bartsch, Taschenbuch mathem. Formeln.- 12. Aufl., Verlag Harri Deutsch, Frankfurt/M., 1990.**

[397] **W.W. Mullins, J. Appl. Phys., 28 (1957) 313.**

[398] **W.W. Mullins, J. Appl. Phys., 30 (1959) 77.**

[399] **V. Randle, J. Microscopy, 195 (1999) 226.**

[400] **D.J. Prior, J. Microscopy, 195 (1999) 217.**

[401] **M.M. Slin'ko, N.I. Jaeger, Physicochemical Basis for the Apperearance of Self-Sustained Oscillations in Heterogeneous Catalytic Systems, Stud. Surf. Sci. Catal., 86.- Elsevier, Amsterdam 1994.**